Politecnico di Milano

School of Civil, Environmental and Land Management Engineering

M.Sc. in Civil Engineering for Risk Mitigation

3D Surface Reconstruction & Change Detection of Glaciers from Multi-Date Archival Aerial Images

Master of Science Thesis

Supervisor

Prof. Marco Scaioni

Co-Supervisor

Dr. Davide Fugazza

Student

Arsalan Malekian

ID nr. 943350

Academic Year 2021-2022

Contents

LIST OF FIGURES

List of Tables

ABSTRACT

As glaciers are affected severely by climate changes, it is crucial to monitor their morphological evolution by detection of mass variation and ice volume changes. Historical aerial images provide valuable information for monitoring and change detection in different areas such as glaciers, because the area of interest can be covered at a well-defined epoch, and help to obtain a better visual and metric analysis. Using aerial images, 3D models can be created and the geometry of the glaciers can be digitized manually to analyse surface extent of the glaciers, whereas data quality and properties make it more difficult to obtain information concerning the height.

The features of each dataset photos are inspected, and they are pre-processed to be used in the 3D reconstruction phase. This pre-processing is conducted to not only minimize the dataset's problems, including shadows covering the glaciers and insufficient image overlapping over crucial places, but also to generate the best achievable dense 3D point clouds from each group of photographs. Point clouds of reconstructed 3D models may be used to detect variations in the Val Veny region and determine the rate of retreating and height differences for each glacier in the area over time. This could be done by computation of distances between points in cloud pairs in consecutive years. In this phase, no manual shifting and translating of point clouds are required as they were georeferenced in 3D reconstruction phase and they are automatically co-registered with Iterative Closest Point (ICP) algorithm in CloudCompare. Four main glaciers in the Val Veny area were chosen to be assessed considering the quality of generated point cloud during the 3D reconstruction phase. The results of the comparisons indicate how glacier heights have varied throughout time and by merging them with local meteorological data, it's feasible to examine how they're connected to climate change in the region. Meteorological data from the area, collected at the same time as the photographs, could also help to better understand glacier activity and dynamics, as well as their link to climate change. Interpretation of these links could illustrate the climate change and significant variations in glaciers which can result in a wide range of hazards that endanger lives and properties nearby.

Despite the fact that retreat rate of volume in all four evaluated glaciers was almost negligible until the mid-1990s, investigations demonstrate a significant rise in volume retreat in all four glaciers in the beginning of 21st century, which is verified by overall rise in mean temperature in warmer months. As a consequence, interpreting glacier behaviour and reviewing the background of glacier-related incidents in the area can lead to the discovery of potential hazards for each glacier in the area, the establishment of monitoring systems in areas where potential hazards exist, and the management of risk mitigation strategies. Furthermore, the approaches described here are applicable to a wide range of glaciers and regions and are not limited to a specific example. Consequently, using modern photogrammetric techniques, it is conceivable to conclude that photographic archives can provide valuable information for morphological evolution studies.

RIASSUNTO

I ghiacciai sono fortemente colpiti dai cambiamenti climatici. E' dunque fondamentale monitorarne l'evoluzione morfologica rilevandone le variazione di volume e massa nel tempo. Le immagini aeree storiche forniscono preziose informazioni per il monitoraggio dei cambiamenti dei ghiacciai, dal momento che ne descrivono visivamente la superficie in epoche ben definite. Utilizzando le tecniche aerofotogrammetriche è possibile creare modelli digitali 3D che descrivono la geometria dei ghiacciai e consentono di analizzarne l'estensione areale. La qualità delle immagini rende più difficile ottenere informazioni sulle variazioni altimetriche.

Le caratteristiche di ciascun blocco di immagini aerofotogrammetriche devono essere ispezionate e pre-elaborate per essere utilizzate nella successiva fase di ricostruzione 3D. Questa pre-elaborazione è condotta non solo per ridurre al minimo i problemi imputabili alla qualità dei dati, come la presenza di ombre e l'insufficiente sovrapposizione delle immagini in alcune aree da ricostruire, ma anche per ottimizzare la creazione di nuvole di punti 3D ottenibili da ciascun blocco aerofotogrammetrico.

Le nuvole di punti dei modelli 3D ricostruiti possono essere utilizzate per rilevare le variazioni nella regione della Val Veny e determinare l'entità volumetrica del ritiro dei ghiacci e le differenze altimetriche nel tempo di ciascun ghiacciaio della zona. Questo potrebbe essere fatto calcolando le distanze tra punti in coppie di nuvole in anni consecutivi. In questa fase non è richiesto alcuno spostamento e traslazione manuale delle nuvole di punti in quanto sono state georeferenziate nella fase di ricostruzione 3D e sono automaticamente co-registrate con l'algoritmo Iterative Closest Point (ICP) in CloudCompare. Quattro ghiacciai principali dell'area della Val Veny sono stati scelti per essere valutati considerando la qualità della nuvola di punti generata durante la fase di ricostruzione 3D. I risultati dei confronti indicano come le altezze dei ghiacciai siano variate nel tempo e, fondendole con i dati meteorologici locali, è possibile esaminare come sono collegate ai cambiamenti climatici nella regione. I dati meteorologici dell'area, raccolti contemporaneamente alle fotografie, potrebbero anche aiutare a comprendere meglio l'attività e la dinamica dei ghiacciai, nonché il loro legame con il cambiamento climatico. L'interpretazione di questi collegamenti potrebbe illustrare il cambiamento climatico e le variazioni significative nei ghiacciai che possono comportare un'ampia gamma di rischi che mettono in pericolo vite e proprietà nelle vicinanze.

Nonostante il tasso di ritiro volumetrico dei quattro ghiacciai esaminati fosse quasi trascurabile fino alla metà degli anni '90, le indagini dimostrano un aumento significativo del ritiro del volume all'inizio del 21° secolo, che è contemporaneo all'aumento complessivo della temperatura media nei mesi più caldi. Di conseguenza, l'interpretazione del comportamento dei ghiacciai e l'analisi del contesto possono portare all'individuazione di potenziali rischi per ciascun ghiacciaio nell'area, che richiedono l'applicazione di sistemi di monitoraggio e di strategie di mitigazione del rischio. Inoltre, gli approcci qui descritti sono estendibili ad altri ghiacciai e regioni e non si limitano a un esempio specifico.

Di conseguenza, utilizzando le moderne tecniche fotogrammetriche, è possibile concludere che gli archivi fotografici possono fornire preziose informazioni per gli studi sull'evoluzione morfologica dei ghiacciai.

Chapter One

1. Introduction

1.1 Background

People and economic infrastructure in mountain areas are at risk as a result of natural processes related to the melting of glacier ice. Glacier avalanches, landslides, and slope instability produced by debuttressing, as well as catastrophic outburst floods from moraine-dammed lakes and outburst floods from glacier-dammed lakes, are examples of these phenomena. Geometric models based on multi-temporal repeated surveys can be used to study glacier retreat under global warming circumstances. Debris flows induced by the activation of deposited loose sediment on steep slopes (Kaab et al., 2005a) and avalanches from suspended glaciers (Vincent et al., 2015) can also have major repercussions for downstream inhabitants. Glacier and cryosphere retreat, which has been documented throughout the Alps (Smiraglia et al., 2015; Fischer et al., 2014; Gardent et al., 2014; Harris et al., 2009), is a significant cause of slope instabilities, which could lead to debris flows by debuttressing rock and debris flanks and promoting the exposure of poorly consolidated and ice-cored sediments (Keiler et al., 2010; Chiarle et al., 2007). Finally, glacier retreat and increased glacier dangers have a detrimental impact on high mountain tourism and economic development (Palomo, 2017). Glaciers cover 369.90 km^2 in Italy (2005-2011 data), nearly the same area as Lake Garda. Since the 1950s, glacial retreat has been particularly severe, with a 30 percent area reduction (Smiraglia et al., 2015) and rising rates of glacier retreat over the past twenty years (D'Agata et al., 2018). Glaciers are a crucial component of the topography in numerous sections of the Alps, such as the Ortles-Cevedale range, and they constitute a tourism asset (Diolaiuti and Smiraglia, 2010; Garavaglia et al., 2012).

The threat of cryospheric hazards as a consequence of climate change necessitates the implementation of preventive technique. Remote sensing is regarded as a valuable method for generating supporting data, such as digital elevation models (DEMs) and multispectral photographs, for this purpose. DEMs are especially effective for detecting glacier thickness and volume changes (Fischer et al., 2015; Berthier et al., 2016), as well as identifying steep places that are more susceptible to geomorphodynamic changes, such as mass movements (Fischer et al., 2015; Berthier et al., 2016). We now have a wide number of commercial, open source, and freely released photogrammetric software tools that allow us to rebuild 2D and 3D models from photos (Pierrot-Deseilligny & Paparoditis, 2006). However, not all of them can be utilized to generate results that are both precise and high-quality (Barto et al, 2014). Going back in time to track the history of a glacier is a difficult task for surveying and monitoring glaciers (with various spatial and temporal resolutions). Historical aerial photos, such as those collected for local cartographic reasons, are particularly significant tools for studying a glacier history and motion in the past. Historical aerial photographs may be used to create geometrically precise photogrammetric models of large-scale glaciers using cutting-edge digital methods. Historical photos, on the other hand, are obviously analogue. In order to use digital algorithms to orient the images through aerial triangulation, films should first be digitalized with a photogrammetric scanner. This study used approaches to examine the evolution of the Glaciers in Val Veny region using digitalized historical aerial photographs mixed with more contemporary digital surveys, either from aerial platforms or UAVs. This provided for the long-term monitoring of an Alpine glacier with great resolution and geometrical precision, which is critical for the application. Despite few disturbances such as scanning

errors and dark shadows in historical images, especially old ones, quality of results from aligning and dense cloud building were acceptable in most of the datasets.

Historical aerial photos, in particular, are one of the most ancient data sources for glaciers. As a result, they are extremely useful for glacier observation and frequently serve as the foundation for analysing area, length, volume, and mass change. As a result, aerial photos were employed in various research throughout the world for probability analysis. By comparing the frontal locations of marine- and land-terminating glaciers depicted in historic aerial images from the 1930s with early and present satellite imagery, the retreat of 132 Greenlandic glaciers could be satisfactorily illustrated through an 80-year period (Bjrk et al., 2012). (Bolch et al., 2019) created a time series of glacier-mass variations in the Himalaya derived from satellite stereo data and areal images, using aerial photographs from 1984 to construct a DTM of the glaciers. In addition, historic aerial images from the 1950s were utilized to calculate comprehensive elevation and volume analyses of sixteen unique Antarctic glaciers (Fox and Cziferszky, 2008, Fieber et al., 2018). Another experiment in Antarctica was based on a massive collection of 30.000 old aerial photographs from the 1940s (Koblet et al., 2010). Between 1959 and 1990, DTMs and orthophotos were created for a glacier in Sweden based on consistent photogrammetric processing of aerial images (Koblet et al., 2010). Also, a dataset including scans of 300 (analogue) aerial images that were obtained between August and October of 1954 by the U. S Air Force over the province of Trento is used for 3D modelling of glaciers and change analysis and result of comparison between acquired model of 1954 and 2015 showed changes up to 70-80 m in height (D.Poli et al., 2020). When working with historical aerial images of glaciers, image quality is important: the images were almost always acquired for reasons other than glacier mapping (surveying of populated regions or major infrastructures), and with much lower radiometric dynamics and resolution than today's technology.

This context looks at how historical aerial photographs may be used to derive DTMs and 3D models from glaciers. Our primary focus is on quality evaluation, with a particular focus on coverage, geometric accuracy, and completeness, as well as how these factors can affect the conventional photogrammetric workflow and how DTMs and 3D data can be obtained within certain constraints.

1.2 Aim of thesis

Unlike field-based techniques, aerial photogrammetry enables large-scale study in inaccessible places. As a result, the surface conditions of glaciers can be studied in great detail, greatly improving our understanding of the evolution and interactions of mountain glaciers and snow cover, as well as assisting in the development and evaluation of models for distributing permafrost melt and measuring freshwater discharge.

This thesis intends to contribute to the knowledge of the aforementioned cryospheric challenges through the use of aerial photography. In this research, the focus is on evaluation of glaciers in the north of Aosta Valley’s mountains where more than two hundred glaciers are nested. In this regard, the two main goals are pursued in this Master thesis:

- Extraction of morphological data from historical aerial photos and identification of the primary data quality controls.

a case study on glaciers investigated photogrammetric techniques for extracting high-resolution data from historical aerial photos. To identify the important controls on the quality of generated data, a range of available material was used.

- Use the retrieved data to quantify and visualize the glacier changes.

This goal entailed acquiring a variety of spatial outputs from the extracted data and demonstrating their potential value in quantifying and visualizing glacier height changes.

- Determine the role of historical image sequences in the comprehension and modelling of glacier-related hazards.

The various products derived from historical imagery were assessed for accuracy and applicability to long-term glacier dynamics monitoring and hazard assessment.

1.3 Structure of thesis

The structure of this thesis follows this order:

Chapter 1 situates this study within its larger context, outlines the study's goals and priorities, and lays out the thesis's structure.

Chapter 2 describes data acquisition and case study on Val Veny's glaciers that because of the wide variety of historical photography, made it possible to map geomorphological progress of the area.

Chapter 3 provides a thorough survey of the literature on photogrammetry processing. Aerial triangulation, image matching, 3D reconstruction, and orthophoto creation are all covered in detail. Data quality issues are examined, and ultimately, applications of photogrammetry in geomorphologic change research are examined.

Chapter 4 describes the history of snow cover in mountain catchments and the rates at which it has decreased. Monitoring snow cover and its multiannual fluctuation helps in understanding the effects of climate change on glaciers.

Chapter 5 focuses on hazards that are directly influenced or induced by contemporary variations in mountain glaciers and permafrost. The focus is on disastrous mass flows, which can flow far downstream or downslope, probably resulting in cascading mechanisms and consequences.

Chapter 6 summarizes the major conclusions and proposals resulting from this investigation.

Chapter Two

2. Data Acquisition

2.1 Introduction

Photogrammetric reconstruction from historical and user-generated content has received a lot of attention in recent decades. Previous research focused on including large amounts of photos from web-based archives while reconstructing from heterogeneous photographs (Ioannides et al., 2013). For instance, Snavely et al. (2007) investigated at how the Great Wall of China was reconstructed using various internet photo archives. Furthermore, historical photography has been used to reconstruct lost heritage in a number of projects, some of which have gained widespread attention, such as the reconstruction of Buddha statues in Bamiyan, Afghanistan, which were destroyed in the early 2000s (Grün et al., 2004). Only a few initiatives (Gouveia et al., 2015) mainly rely on photographs older than 50 years (Henze et al., 2009). One example is Roland T. Bird that reconstructed of the Paluxy River Tracks using 1940s images (Falkingham et al., 2014). Even while basic workflows are independent of the age of the photo or the technique by which it was made – digital or non-digital — older photos are more difficult to work with due to archival quality, digitalization challenges, equipment required, and film media. Another issue in digital picture collections is determining the context and objective of photographs. Many data sources, including as surveying data and topographical papers, can be used to determine the rate and orientation of these changes (Toure, S.I.;2018). In land surface assessment, remote sensing data remains the most important source. Numerous measuring devices aboard airplanes, satellites, and unmanned aerial vehicles can be used to acquire this data (UAVs). Satellite photos, aerial photographs, and point clouds are examples of geospatial data gathered using remote sensing (Kolecka, N.;2017). Using remote sensing data from various times, it is feasible to detect the dynamics of land-use change and examine these changes in the height structure of tree vegetation (Dandois, J;2013). Historical aerial images may be especially useful in this case since they can be used to recreate the state of a specific location before other remote sensing techniques were accessible (Midgley, N.G.;2017). Converting analogue historical aerial images to digital geoinformation typically includes special considerations and challenges. Analogue photographs must be digitized from their film or paper origins before being transformed into usable geographical content, unlike their modern digitally captured equivalents. Analogue media are subjected to different physical processes prior to and even during the digitization process, which can cause nonuniform radiometric and geometric degradation (Redecker 2008; Redweik et al. 2010). Furthermore, historical images may have been captured in less-than-ideal conditions, such as low illumination and/or vision, semi-oblique camera location, fluctuating altitude, significant temperature change, and other instabilities in flight (Kingslake 1947, 6; Redecker 2008, 6). The clarity and visibility of objects photographed on reconnaissance flights is further limited by the focal length chosen, as well as lens aberrations and limits in the resolving power of older lenses and film emulsions (Kingslake 1947, 7). Following then, the conditions for image storage and transfer may have been less than ideal. Finally, prints and film scans may be derived from second or later generation media transfers. All of these parameters have the potential to influence the likelihood and quality of 3D data recovery. These difficulties can have a variety of unfavorable implications on the processing outcome when using such resources for 3D reconstruction. Localized errors can be caused by nonuniform geometric distortion exacerbated by age-related degradation, and even high-end non-photogrammetric scanners can induce nonuniform media distortion during the digitization process, including warping and stretching effects that can strongly influence terrain generation and are difficult

to compensate for due to their nature. Even though non-photogrammetric scanners can be calibrated to minimize the level of geometric distortions caused during the scanning (e.g., Nocerino et al. 2012), research shows that even scanners that have been roughly calibrated are unable to produce digital imagery that is suitable for the most demanding photogrammetric processes (Baltsavias and Waegli 1996, 19; Mitrovic et al. 2004). Additionally, the time-consuming process of manually applying calibration profiles to photos scanned using non-photogrammetric scanners may render such methods unsuitable for big image collections (Mitrovic et al. 2004, 58). Scanning photos with photogrammetric grade devices should therefore be deemed important for both current and future utilization of scanned image information. Besides that, before using them as a basis for terrain generation, a pre-processing workflow for image optimization will be required.

2.2 Aerial Surveys

2.2.1 Purpose of Aerial Image surveys

All of the collaborating organizations have obtained aerial photos in the past, both analogue and digital. Aerial images aerial surveys, both analogue and digital, were primarily used to create and update topographic maps. Digital photos are nearly often used to create photogrammetric products like orthoimages and Digital Terrain/Surface Models (DTM/DSM) (Figure 2.1). However, in the analogue instance, the production of these devices has been limited. Only one organization has calculated Digital Terrain Models using analogue aerial image surveys, while five others have created analogue orthoimages (Sébastien Giordano., 2019).

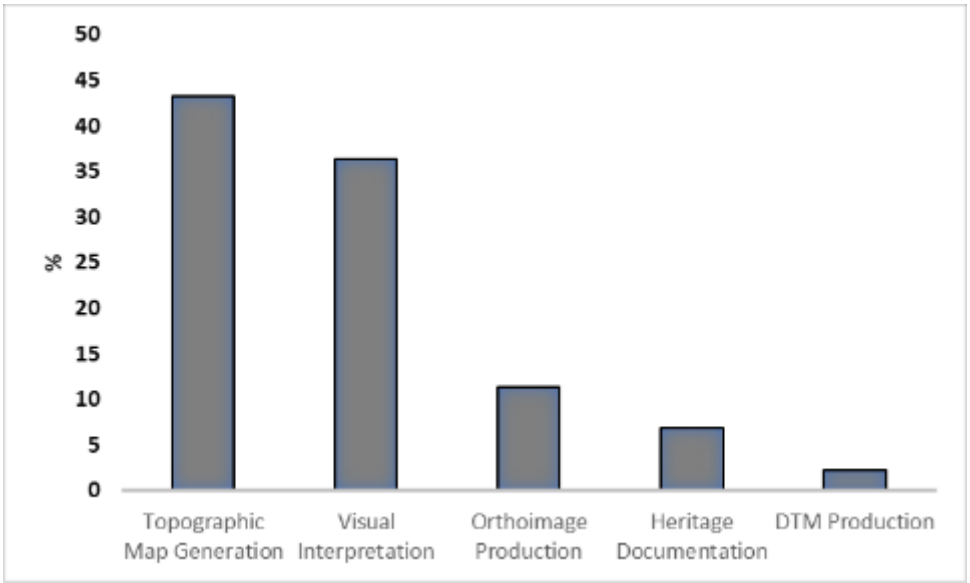

Figure 2.1. The purpose of Analogue aerial surveys by different organizations in the past.

On the one hand, the vast majority of analogue picture surveys obtained by organizations are nadir (vertical) images, with 100% of organizations doing such vertical image surveys. A few oblique photos have been captured on the other hand. Only vertical photographs were captured by 82 percent of the organizations, 12 percent acquired 90 percent of vertical images (together with 10 percent of oblique

images), and 6 percent acquired 80 percent of vertical images (along with 20 percent of oblique images). The analogue image surveys were mostly conducted using photogrammetric methods (enough circumstances (overlapping) to obtain 3D data) (Sébastien Giordano., 2019).

2.2.2 Error Sources of Archival Photographs

Every frame acquired by a camera, whether digital or film, can be affected by a broad variety of elements such as earth curvature, film and paper shrinkage, nonplanar image film plane, atmospheric refraction effects, optical distortions, tilt and relief displacements, according to the researchers. The extent of these effects varies depending on the camera's position and the subject matter in each shot. Film photos must be scanned before they can be used in computer systems. Scanned film pictures are subjected to further degradations, resulting in the loss of radiometric and tonal variation, as well as spatial resolution (Morgan, Gergel, & Coops, 2010, p. 50). The following sections provide an overview of each main photo error cause, as well as its impacts and implications for historical aerial photography study.

2.2.2.1 Interior Orientation Parameters

The interior orientation parameters of a camera are used to determine the camera's internal geometry, including the position of the camera's principal point and focal length, as well as distortion adjustments (Jain, Kasturi, & Schunck, 1995). These factors are combined to convert coordinates from an image pixel coordinate system to an image space coordinate system with precision. The geometric center of the shot is the principal point position. It is also at this point that the focal length of the lens is calculated. The distance between the principal point and the perspective center is known as the focal length. There are two types of lens distortion corrections: radial and tangential lens distortion. In a lab, these parameters are calibrated by taking target photos and comparing their actual image locations with the positions they should have occupied if the camera had created a perfect perspective view (Wolf & Dewitt, 2000, p. 64). As seen in Figure 2.2, this comparison is made via the image's fiducial markers.

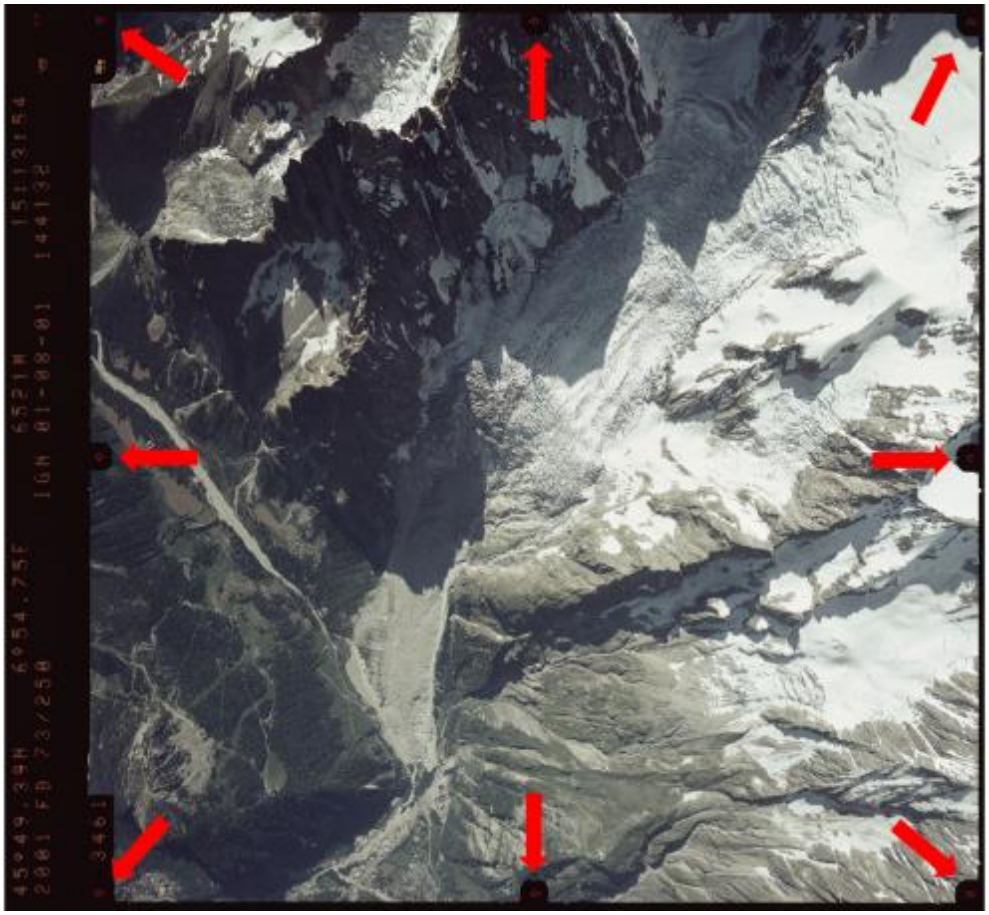

Figure 2.2. Aeiral photograph illustrating the location of fiducial marks

There are eight fiducial markers on each photograph; they form the reference coordinate system for image positions on a photograph (Wolf & Dewitt, 2000, p. 58). The intersection of the fiducial markers denotes the photograph's specified principal point, and their uniform placements in each image allow for distortion parameter calibration. These camera parameters are presented in the manufacturer's camera calibration report, which is supplied with picture products. However, for many old aerial photographic archives, this information has been lost, and metadata regarding the camera used is limited. When working with historical images, this is one of the most common causes of uncertainty.

2.2.2.2 Exterior Orientation Parameters

The external orientation parameters of a camera describe the camera's location and orientation in space. In a ground coordinate system, the location is described by X, Y, and Z coordinates, with Z denoting the image height at altitude (Jain, Kasturi, & Schunck, 1995). Three rotation angles along three axes, commonly called omega, phi, and kappa, establish the orientation; they reflect the angular rotations of the ground system and the image coordinate system. Omega and phi are expected to be close to zero in a vertical image. The tilt of the camera leads the photo to skew in the direction of rotation as they rise, as seen in Figure 2.3.

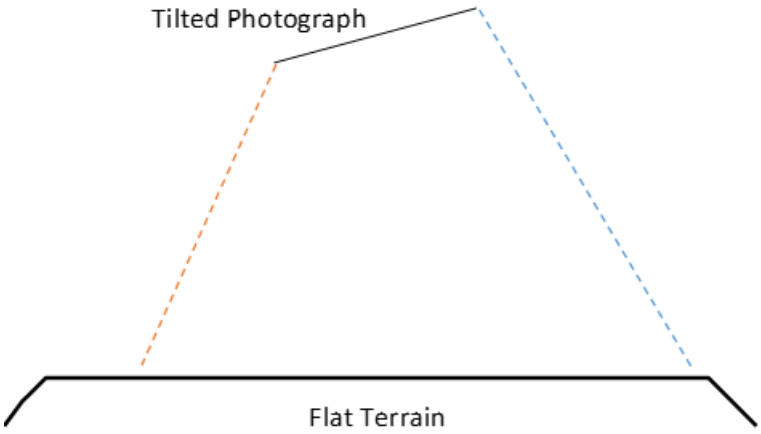

Figure 2.3. Image skew in a tilted photograph, adapted from Wolf and Dewitt, 2000, p. 218.

Skew occurs when one side of the image is closer to the ground (orange line) than the other (blue line), and it must be adjusted. Tilt was previously reduced by applying estimated corrections to the imagery-derived estimates (such as area). Some external orientation characteristics of historical surveys can be estimated; however, the calculation contains errors and Uncertainties (Broadbent., 2017).

2.2.2.3 Environmental

Environmental conditions present at the moment of photo capture can have a significant impact on image quality. The time of day, glare, and meteorological conditions such as haze, clouds, or scene brightness can all have an impact (Wolf & Dewitt, 2000). These impacts are mitigated by careful project planning that ensures aerial photography is taken at the best possible times of day and weather (Wolf & Dewitt, 2000). Environmental conditions may frequently have an influence on image quality and lead an image to be eliminated from processing when employing historical aerial photography.

2.2.2.4 Scanning Film Aerial Images

Aerial photography taken on film must be converted into a digital version before being used in computers. Scanning turns an analogue (continuous surface) into a digital raster surface with 12 discrete pixels. The type of scanner used has an impact on the quality of the digital photo. (Wolf & Dewitt, 2000) Photogrammetric scanners can capture pixels with excellent spatial precision (2-3 microns) and high resolutions up to 5 to 15 microns. In order to scan aerial photography, standard desktop scanners lack the image resolution and precision required. Choosing the right scanning resolution might have an influence on the image processing capabilities. Small defects in the photographs can be introduced by the physical scanning process, such as rotation of the resultant scanned image, displacement of the principal point (the image center), and uneven image sizes from image to image. Small uncertainties can have an influence on processing methods; hence they must be standardized before processing.

2.3 Study Area

The Aosta Valley (Figure 2.4) is a high elevation and relatively small administrative district in Italy's Western Alps (3,262 km^2). The population density in the valley bottom is 39 people per square kilometer, with the maximum density in Aosta city,1,610 people per square kilometer. Around 80% of the regional GDP is generated by the service industry, with tourism playing a major role. The altitudes range from 321 to 4808 m a.s.l., with more than 80% of the surface lying above 1500 m a.s.l. (D'Amico et al. 2020). It has substantial glaciated massifs including Gran Paradiso (4061 m a.s.l), Mont Blanc (4808 m a.s.l), and Monte Rosa (4559 m a.s.l). The Aosta Valley has the largest glacier coverage of any area in Italy. Based on the latest Italian Glacier Classification (Smiraglia et al. 2015), there are 192 glaciers in the Aosta Valley Region with a total area value of 133.7 km^2, accounting for 36 percent of the Italian glacier area between 2005 and 2011. The glaciers range in altitude from roughly 1400 to 4800 m a.s.l.. In terms of recent glacial retreat in Italy, between 1959 and 1962 and 2005–2011, the Aosta Valley contributed 24% to the overall global glacier loss, which is 30.5% (Smiraglia et al. 2015).

Since the end of the Little Ice Age (LIA), between 100 and 300 years ago, most mountain glaciers and minor ice caps have been retreating (Barry, 2006; Zemp et al., 2008). Glaciers, on the other hand, have recently begun to melt at rates that cannot be explained only by natural climate fluctuation (Dyurgerov and Meier, 2000). Glacier shrinkage is most likely caused by significant changes in mid-tropospheric conditions, such as the widely acknowledged rapid increase in temperature (IPCC, 2001, 2007) that has been discovered to be more than twice the Planetary average over the last 50 years in the Alps (Böhm et al., 2001; Casty et al., 2005). Since the end of the 19th century, data on terminus instability in the Alps has shown a rather consistent retreating tendency (Citterio et al., 2007; Hoelzle et al., 2003; Zemp, 2010). Between 1950 and 1990, there was just one significant break in the general pattern, when a modest glacier advance occurred (Citterio et al., 2007; Patzelt, 1985; Wood, 1988). After this small (in magnitude) glacier advance, retreat reigned supreme once more (Hoelzle et al., 2003; Zemp, 2010). Over the last six decades, mass balance data in the Alps have revealed significant ice losses, which have recently increased (i.e., 1985 to present; Zemp, 2008; Zemp et al., 2006, 2008).

Data from glacier inventories also show a considerable and rather consistent glacier shrinking, with the smallest glaciers making up the majority of the ice losses. According to Lambrecht and Khun (2007), Austrian glaciers shrank by roughly 17% between 1969 and 1998. According to Knoll and Kerschner (2009), the area of Tyrolean glaciers decreased by about 36% between 1983 and 2006, owing primarily to small glaciers (0.1 km^2 < area < 1 km^2), which accounted for 23.8 percent of the total decrease. In preparing the Swiss Glacier Inventory 2000, Paul et al. (2004) discovered that glaciers less than 1 km^2 were responsible for 44% of the area decline between 1973 and 1998/1999, accounting for 18% of the overall initial area. Maragno et al. (2009) investigated the area variations of 34 glaciers in the Adamello group (Lombardy, northern Italy) from 1983 to 2003 and discovered a surface decrease of 19% with an increased area rate variation recently. Diolaiuti et al. (2011) examined the area and geometry fluctuations of a small but representative sample of glaciers in the Italian Alps (Piazzi Dosdè Group) from 1954 to 2003, finding a 51 percent drop, with small glaciers accounting for the majority of the decrease. Diolaiuti et al. (2012) used three surface area recordings from 1991, 1999, and 2003 to show the recent surface trend of a group of 249 glaciers in the Lombardy region (200 km east of the Aosta Valley Region). Between 1991 and 2003, the size of the glaciers assessed shrank by 21%. Glaciers smaller than 1 km^2 contributed for 53% of the overall area reduction (13.1 km^2) between 1991 and 2003. In recent years, the area variation has been higher, with a rate of –11.7% between 1999 and 2003.

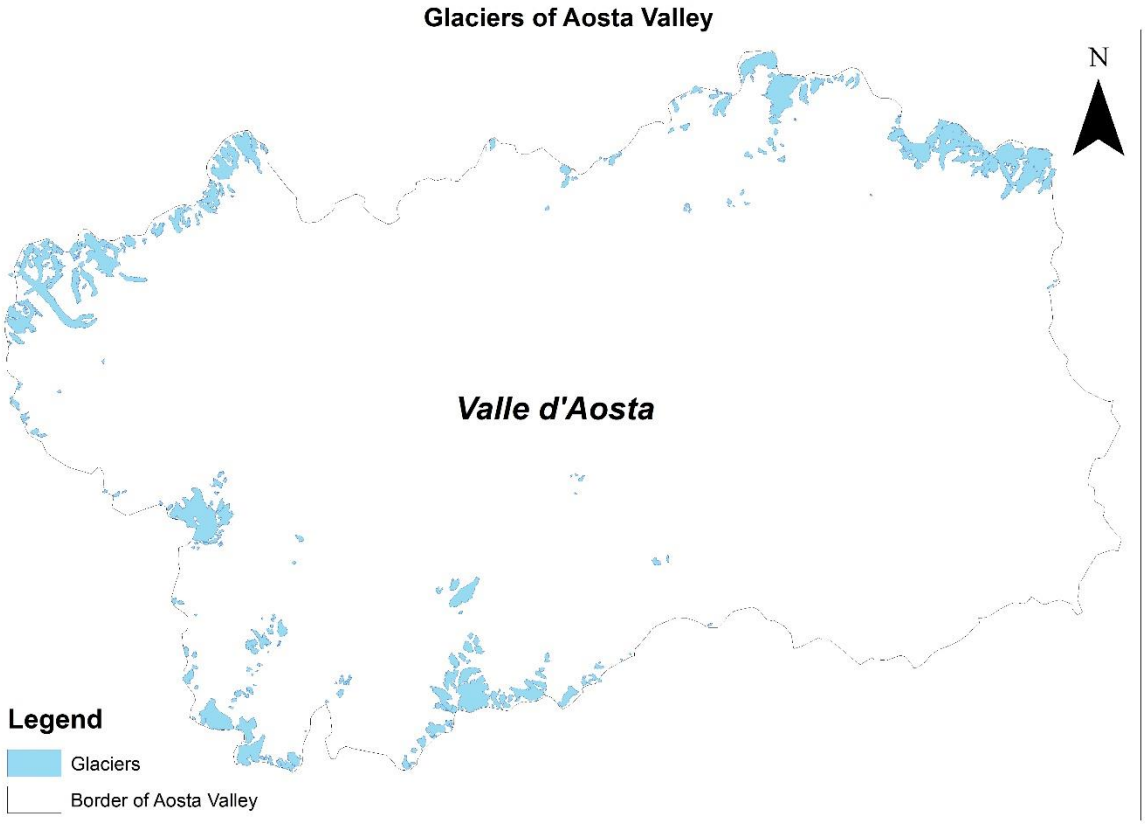

Figure 2.4. The distribution of glaciers over the Aosta Valley at the north of Italy.

According to coverage area of the available archival images, this work mainly is focused on the evaluation of glacier changes in Val Veny area (Figure 2.5). Val Veny is a lateral valley of the Mont Blanc massif located west of Courmayeur. Val Veny is split into three sections: the section that runs parallel to the Mont Blanc massif between the Seigne pass (2,512 m a.s.l.) and part of the Miage Glacier, the middle part that is called Plan Vény, the valley's mouth (1,444 m a.s.l.) which is surrounded by Mont Blanc and the lower Brenva Glacier.

The existence of significant geological components and varied outcropping lithologies, which are molded by glacial activity and result in a diverse geological environment, is an important aspect of this small region (sensu Gisotti 1993). In fact, the geologic control of the relief is obvious: the difference in altitude between the two sides of the Veny Valley and the characteristics of the slope mechanisms that dominate the opposing sides of the valley reflects the resistant Northern crystalline basement vulnerability to erosion in comparison to the weak Southern sedimentary coverage. Because of the many typologies and many geographical elements found in the Miage area, lakes in the Veny Valley offer another significant aspect, not only for their scientific significance but also for their educational value. Lac de Combal, Lac du Miage, Lac du Jardin du Miage, and Lac du Breuillard are the most notable lakes, all of which are supported by moraines or the glacier ice cliff (Bollati., 2013).

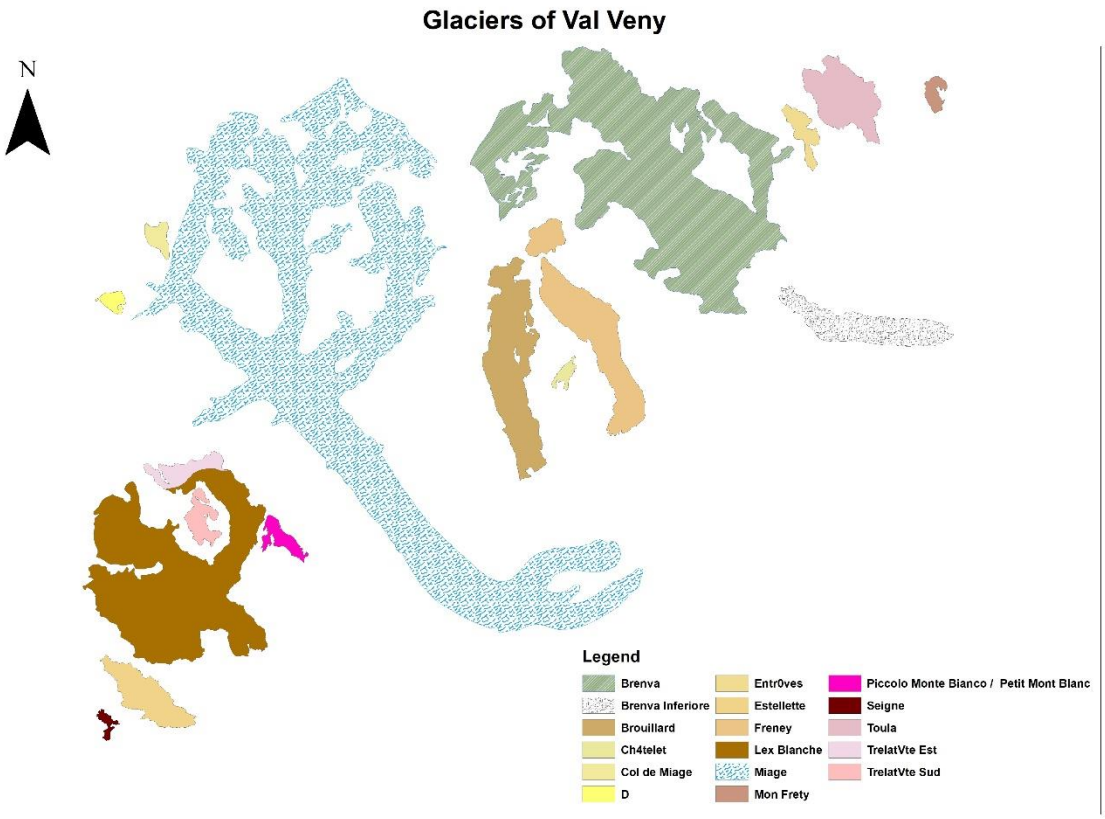

Figure 2.5. Val Veny area and location of glaciers around this valley.

As is clear, Miage and Brenva are the two primary glaciers in this area, and our research is mostly focused on these glaciers (Figure 2.6). Since the 18th century, when De Saussure first noticed it, the Miage region has been investigated (De Saussure, 1774). Many studies have been undertaken on its glaciological elements, as listed below; consequently, the glacier's scientific relevance contributes to the site's geohistorical importance. The Miage Glacier is Italy's longest glacier and Europe's largest debris-covered glacier, measuring roughly 10 kilometers in length (Deline et al., 2005). Debris covers around 5 km^2 of its 11 km^2 total area, mostly from rockfall from neighbouring walls (Deline et al., 2005) and avalanching in deposition regions of its four tributaries (Mihalcea et al., 2008). Due to the quick thinning of the glacier tongue, debris transported along within the glacier is also being exposed at an accelerated pace. The variety of supraglacial debris sources, as well as the peculiar mica schist-dominated lithology of the rock walls surrounding the glacier, results in a diverse debris lithology; the debris cover becomes continuous around 2,400 m a.s.l. and continues intact until the terminus. Crevasses or moulins, on the other hand, can cause inconsistent areas (Mihalcea et al., 2008). Although the spatial distribution of thicknesses is uneven, especially on sections of the northern terminal lobe, debris thickness usually increases between a few centimetres at 2,400 m a.s.l. to over 1 metre at the terminus at 1,775 m a.s.l.. Because of several key features (Pelfini and others 2005), the Miage Glacier is the best example of a 'Himalayan Glacier of the Alps,' including its accumulation zone, steep cliffs characterised by avalanches, avalanches that indirectly feed the glacier, a notable difference in altitude between the accumulation area and the terminus, and variations in ice thickness in the frontal area .

The Brenva Glacier is a valley glacier on the Alps' southern flank. It flows into Val Veny, in Entrèves, near Courmayeur, and is Italy's second longest and eighth largest glacier. It has been subjected to a series of significant rock avalanches throughout the millennia, which have formed the glacier and altered its flow. Brenva glacier is a valley glacier that stretches for 7.5 kilometers, with a maximum

width of 2.15 kilometers, and a mean tongue width of 0.5 kilometers. Between 2460 and 2550 meters a.s.l., a rock step, the "Pierre a Moulin," divides the tongue transversely into two regions (Figure 2.7). The active component of the glacier is located up-valley from this step. Because the down-valley sector is disconnected from the main body, it lacks dynamic continuity. Debris has completely buried the lower section (Giani et al., 2001).

It is worth noting that Brenva Glacier has experienced some disastrous incidents in its history. On the afternoon of November 14, 1920, a massive rock fall detached from the east flank of the Mont Blanc near Grand Pillier d'Angle, close to the 1997 scar, down the Brenva Glacier on a similar course for roughly 5000 m and ran up the other valley side (S.G. Evans and J.J. Clague., 1998). The Brenva Glacier was hit by a massive rock-ice avalanche for the second time during the twentieth century. On January 18, 1997, in the upper Aosta Valley, a massive block of granite rock detached from thawed permafrost (0 to -5°C) (J. Noetzli., 2003) in the Mont Blanc east face at 3725 m asl and slid downward onto Brenva Glacier, causing a major Alpine avalanche event. A vast volume of ice and snow was mobilized by the mass movement, generating a powder avalanche with a total volume of 6 to 7 million m^3 (G.Barla., 2000). The horizontal and vertical movements were 5500 and 2150 meters, respectively, with a reach angle of 21.6 degrees. The right lateral moraine was overflowed by one lobe of the rock-ice avalanche. The right lateral moraine channelled the other portion, which eventually reached the glacier's front.

Figure 2.6. location of Miage and Brenva glaciers in Val Veny.

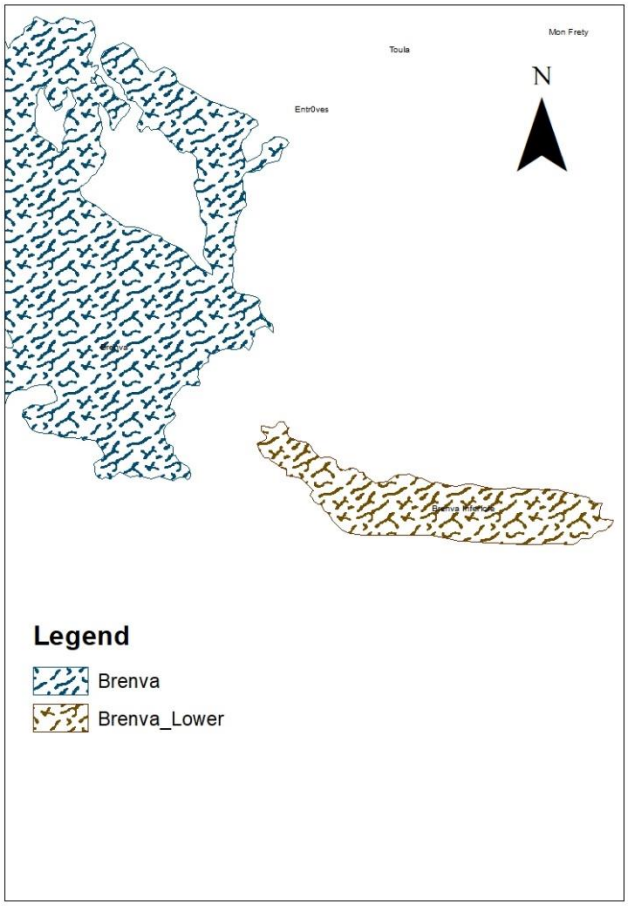

Figure 2.7. the separation of Brenva Glacier in the middle part by a rock step called “Pierre a Moulin”.

Two other considered glaciers to be evaluated are Brouillard and Freney Glaciers, which are located between Miage and Brenva (Figure 2.8). The Brouillard glacier is a glacier that descends on the Italian side of the Mont Blanc. It is placed between the Brouillard ridge to the west and the Innominata ridge to the east in the Italian Buttresses of Mont Blanc. It begins to form at an altitude of 4,000 meters and reaches 2,000 meters a.s.l. The glacier surface is heavily crevassed.

Also, the Freney glacier is found in the Aosta Valley, In the Mont Blanc Mountain Range. It is located between the Peuterey ridge and the Innominata ridge. It has a total size of 1.1 km^2 and a height range of 1785 meters, with the maximum height at 4120 meters a.s.l. and the lowest point at 2335 meters a.s.l..

Figure 2.8. The location of Freney and Brouillard Glaciers between Miage and Brenva

2.4 Data description

In Europe, the first aerial photograph flights took place in the 1920s and 1930s. Stability and shutter speed were technological hurdles in the early aerial photogrammetric operations, but Sherman M. Fairchild created a camera with the shutter placed inside the lens system around the end of The World war I. Over the following 50 years, this design enhanced the image quality dramatically and became the industry standard for aerial camera systems (Doyle, 1980, Baumann, 2019). The aerial images used in this work over the Val Veny were obtained from various aerial missions from1967 to 2006. The scanned images are provided by the French IGNF (Institut National de l'Information Géographique et Forestière). All datasets include a certificate containing information on the camera and lens used, the maximum aperture, the focal length before and after calibration, the location of fiducial markers on the photographs, and the distance between them, as well as information regarding distortion. Georeferenced information is not available, as is common with archive photos. The majority of image parameters vary from one flight to the next, including flight height, acquisition scale, and side overlap. The camera model used in different datasets may vary, but the pixel size in most of them is around 0.02 mm x 0.02 mm and the focal length is around 153 mm, with the exception of the 2006 dataset, which was taken with a digital camera. (Table.2.1)

In all datasets, the variation of flying altitude is 4.7 to 6.35 km, with the photos from the 2001 dataset having the lowest flying height and the data from 1967 showing the highest-flying altitude. The coverage area of the photos from 1996 to 2001 is between 300 and 345 km^2, whereas the data from 1967, 1979, and 2006 cover an area of 132 to 173 km^2. Furthermore, camera coordinates are only provided for three datasets: 2001, 2000, and 1996, and are displayed on the image's side panel. Using camera data for georeferencing allows faster processing times. Ground control point coordinates, on the other hand, are often more precise than telemetry data, allowing for more exact georeferencing. The model is linearly changed throughout the georeferencing process using a 7-parameter similarity transformation (3 parameters for translation, 3 for rotation and 1 for scaling). Only linear model

misalignment may be compensated using this transformation. All of the photographs were acquired during the warmer months, from June to September, with the exception of the 1967 photos, which were taken in October.

Year	Date	No. Images	Camera Coordinate	Camera Model	Flying Altitude [km]	Coverage Area [km^2]
2006	August 23rd to September 5th	78	Not Available	Digital	5.54	173
2001	August 1st to 13th	73	Available	RMKTOP15	4.78	345
2000	June 23rd to August 1st	25	Available	RMKTOP15	5.54	310
1996	July 3rd to August 4th	35	Available	RMKTOP15	5.02	301
1988	July 26th	23	Not Available	RC10	6.15	321
1979	September 5th	19	Not Available	RC10	5.7	144
1967	October 11th & 12th	24	Not Available	RC10	6.35	132

Table 2.1. Properties of dataset from 1967 to 2006 via Aerial survey

The side information on the image frame provides the date and time of the flight, the lens type, and the estimated altitude, as was typical practice in analogue aerial photography (Figure 2.9). The coordinates of camera position are included in the side information of photos from datasets 1996, 2000, and 2001, which might be useful for the alignment method. Other datasets do not have this attribute.

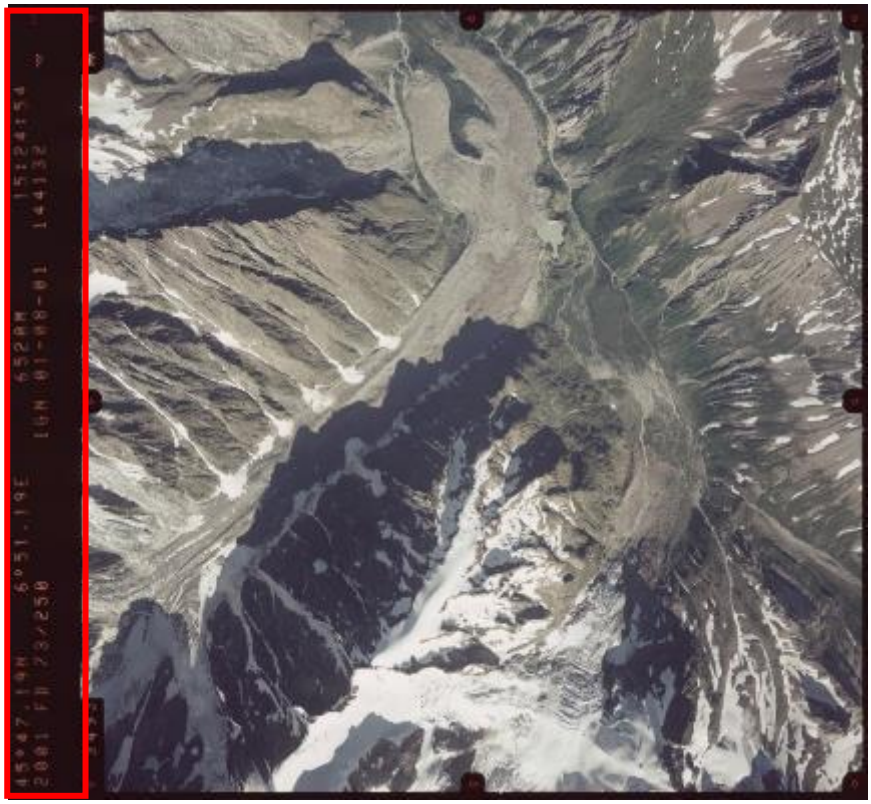

Figure 2.9. example of scanned aerial image over glacial zone with side information on the image

The image quality was evaluated by taking into consideration some factors. Firstly, the aerial photographs completely encompass the Val Veny, particularly the glaciers. In flat, hilly, and mountainous locations, the coverage is acceptable for aerial triangulation and orthophoto creation. Secondly, the analogue photo is transformed to a digital data set after scanning, which degrades the image quality even further. Analog films should be scanned with photogrammetric scanners with geometric precision of a few microns and high radiometric dynamics to retain the original image quality. Also, Steep slopes, mountain peaks, and deep cirques characterize the mountains around Val Veny and dark shadows can be seen in images of these regions (Figure 2.10). Shadows frequently look as essentially uniform black surfaces due to the photos' limited dynamic range. Snow may also be a concern; even if the amount of snow is small, it will smooth out a convex or concave flat surface. As the snowfall increased, sharp edges and concave sections were covered, resulting in flat terrain. As a consequence, identifying and measuring any important trait is rather difficult in some images of older datasets.

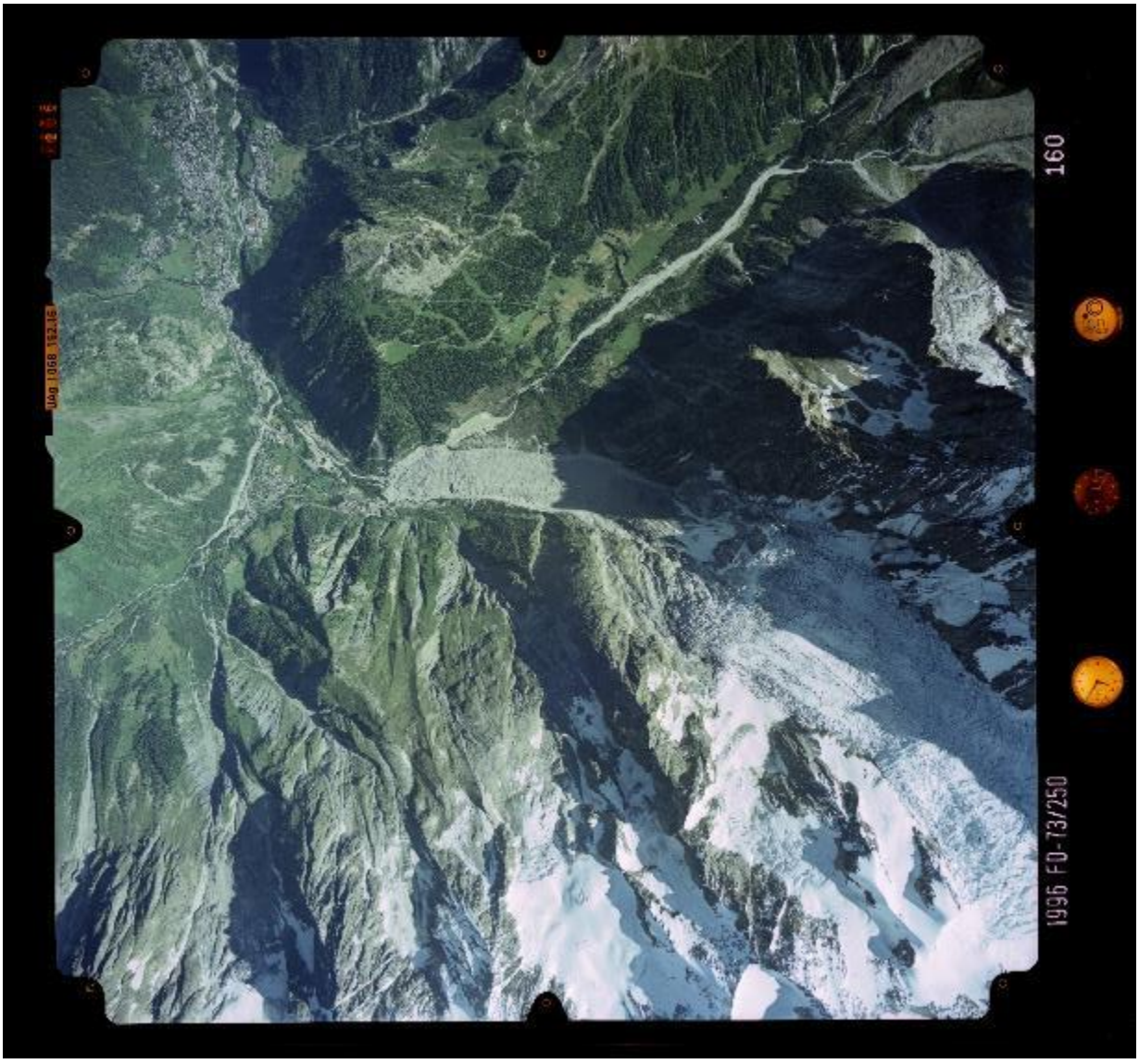

Figure2.10. Example of dark shadows on glaciers near vertical surfaces in 1996 image

The information on the side of each photograph is useful for a variety of objectives such as georeferencing and dynamic of glaciers. The date and time of each set of images helps to better understand the dynamics of the glaciers by identifying the mean temperature in that region. To be compatible with satellite data used for georeferencing in this study, camera coordinates supplied at the side information of photos for datasets 1996 to 2001 were changed to UTM coordinates.

Structure from motion captures the geometry of the scene, the camera's location (external orientation), and an estimate of the camera's calibration (interior orientation) parameters by utilizing algorithms to match features across a sequence of overlapping photos using triangulation. Following chapters describe the phases of the procedure from the original aerial photographs to the different outputs.

2.5 Conclusion

According to the literature, recent advances in photogrammetry techniques have considerably boosted the use of these techniques in landform studies, particularly glacier monitoring. It has been observed that data collecting is the most crucial part of the task, and that having the best possible data quality is critical for further processing. The sources of errors in aerial images have a significant influence in determining the data's quality. At the acquisition phase of historical photos, aspects such as time of photography, meteorological conditions, and flying altitude are vital, and they influence subsequent procedures including scanning films and digitalization. Some of the concerns mentioned in this study's findings, such as shadows near high cliffs, will be troublesome in later stages. Each dataset has a distinct number of photographs, as well as a different flight altitude and coverage area, and their side information indicates that they were mostly acquired during warmer months, which is appropriate for the objectives of the study. Furthermore, having a certificate for each dataset that describes characteristics such as focal length, pixel size, and distances between fiducial markers in each image facilitates image processing in subsequent stages.

The focus of the work is on glaciers around the terminal part in the valley zone, though the images cover mountains areas as well. Also, the hazard history of the glaciers and their vicinity of them to the city represent their hazard potential to be assessed according to availability of the data and coverage area of datasets.

Chapter Three

3. 3D Model Reconstruction

3.1 Introduction

Three-dimensional (3D) reconstruction and modelling of objects from photographs or range data has been a very popular study subject over the last 30 years (Haala and Anders, 1996, Haala and Kada, 2010, Rottensteiner et al., 2014, Mcclune et al., 2016, Song et al., 2020). Disaster risk management, urban planning, population density study, mobile telecommunication, solar potential evaluation, 3D GPS navigation, and environmental modelling are just a few of the applications for digital building models. In recent decades, acquiring 3D information about the Earth's topography became more pursued for a better knowledge of the planet's surface. Digital elevation models (DEMs) and geomorphological terrain assessment may now be used for geoscience applications thanks to technology breakthroughs and reformation software algorithms (Carrivick et al., 2016). snow avalanches, glaciology/geomorphology, rock slope stability, and geological processes have all benefited from high resolution and accuracy 3D models. Without using 3D spatial data, we will not be able to comprehend many of these mechanisms as well as we do nowadays (James & Robson, 2012).

Developing 3D models from a series of images is a classic problem in computer vision (Hartley and Zisserman, 2003), and it has been widely researched (Snavely et al., 2008; Sweeney et al., 2015; Moulon et al., 2013; Schonberger and Frahm, 2016; Furukawa and Ponce, 2010; Barnes et al., 2009; Schonberger et al., 2016). The most typical method for creating a 3D reconstruction from a series of photos starts with feature recognition and matching, which is then put into a Structure-from-Motion (SfM) algorithm to retrieve camera positions and a sparse model (Snavely et al., 2008). The Multi-View Stereo (MVS) technique is then used to densify the structure of the reconstruction supplied by the sparse 3D point cloud (Hartley and Zisserman, 2003). The approaches can be adjusted to the specifics of the scene (e.g., terrain smoothness (Ruano et al., 2014)), but the many of them are developed for generic scenarios, and the opensource versions are particularly popular (Stathopoulou et al., 2019). Computer systems can extract a lot of spatial and temporal information from patterns in overlapping photographs of the same scene (Trucco & Verri, 1998). Computer vision is the process of extracting, processing, and evaluating information from single or series of digital photographs. It was developed in the 1950s in the field of computer science with the purpose of modelling human vision in computing for artificial intelligence applications (Mayer, 2008). In the last 15 years, computer vision technology has grown in combination with computer systems, robotics, and machine learning. The technology's primary emphasis was on pattern matching and automation, rather than precision (Remondino, Del Pizzo, Kersten, & Troisi, 2012). This led to disagreements in the 1990s between traditional photogrammetrists who desired a stronger focus on accuracy and reliability (Remondino, Del Pizzo, Kersten, & Troisi, 2012), with some claiming that it was not a valid approach since it did not use the camera's true calibration parameters in the solution and was only useful for visualization, object-based navigation, or other equivalent objectives (Remondino, Del Pizzo, Kersten, & Trois). This is due to the fact that computer vision evaluates the camera's internal orientation parameters, and these calculated constants fluctuate from image series to image series, even when the camera is the same. Mayer (2008) discovered evidence of how applications of computer vision technology in photogrammetry began to develop in the early 2000s in his review of the history of computer vision. First, an image panorama was constructed using photos that had no specified size, ordering, or illumination information (Brown &

Lowe, 2003). This was quickly followed by claims that a series of images could be self-calibrated if the series' perspective was known (Pollefeys, Van Gool, Vergauwen, Verbiest, & Cornelis, 2004), and finally claims that the triangulation methods used could deliver a DSM produced from the imagery series that could challenge those produced by laser scanners began to emerge (Nister, 2004).

Web services (e.g., Google Earth, Maps, Bing Maps, etc.) raised the requirement for orthophotos, and led to the creation of new algorithms and sensor in the early 2000s (Barazzeti, Brumana, Oreni, Preyitali, & Roncoroni, 2014, p. 57). This eventually led to a combination of classical photogrammetry with computer vision to solve two main challenges: automation in the orientation process and reconstruction, that produces dense 3D models with better resolution than laser scanner models in some applications. Second, the photograph capture procedure is more flexible now that photogrammetric software has advanced significantly in recent years, allowing any sort of image to be used (GarciaGago, Gonzalez-Aguilera, Gomez-Lahoz, & San Jose-Alonso, 2014, 6(6), p. 5671). Through self-calibration algorithms in the 3D model calculation procedure of computer vision known as structure from motion (SfM), the hybrid method eliminates the necessity for precise camera input interior or exterior orientation parameters (Visockiene, Brucas, & Ragauskas, 2014). Commercial photogrammetric software programs such as Agisoft Metashap and Pix4D Professional have included these hybrid approaches (Visockiene, Brucas, & Ragauskas, 2014). Remondino, Del Pizzo, Kersten, and Troisi (2012) compared the accuracy of several photogrammetric computer vision approaches to classical photogrammetry on a range of object categories. They used cubes, spheres, a lighthouse, and a railway to evaluate image databases. Although the approach did not preserve reliability and repeatability while calculating the camera's interior orientation parameters, their conclusion was that the actual final object coordinates were unexpectedly precise (within a scale factor and a check point mean difference of less than 10cm). Verhoeven (2014) validated that, stating that the procedure fails for individual photos or those that are blurry, noisy, or insufficiently exposed.

3.2 Methodology

Photogrammetry is the process of reconstructing the location, orientation, form, and dimension of objects from photographs, which can be either photochemical (conventional photography) or photoelectric (digital photography) (digital photography). A third type of image, laser scanner images, has only recently become available; laser scanner pictures feature distance information connected with each picture element.

Analogue photogrammetry is a form of photogrammetry that starts with conventional photographs and processes them with optical-mechanical devices. Analytic photogrammetry is a type of photogrammetry that is based on traditional photographs but handles the entire analysis process using computers. Digital photogrammetry is the third phase of development. In such instance, light falling on the focal plane of the capturing camera is recorded using electronic detectors rather than a light-sensitive simulation. Starting with such digital photos, the entire assessment procedure is carried out by computers, which imitate human sight and perception. In contrast to hardcopy photogrammetry, which works with digitized film-based photos, digital photogrammetry is often referred to as softcopy photogrammetry, especially in English. Pattern recognition is one component of machine vision, or computer vision, of which photogrammetry is a part (Karl Kraus, 2004). Photogrammetry enables for the reconstruction and study of an object without making direct contact with it. The collection of information about the Earth's surface in this manner is now known as remote sensing. All ways of obtaining information about the Earth's surface by measuring and interpreting electromagnetic radiation2 reflected from or generated by it are referred to as remote sensing. While remote sensing comprises the element of photogrammetry

that deals with the Earth's surface, it is photogrammetry, not remote sensing, when the primary focus is in geometric qualities.

3.2.1 3D Point Cloud generation using SfM

Structure-from-Motion (SfM) is based on the same principles as stereoscopic photogrammetry, in that it can discern 3-D structure from a series of overlapping, offset pictures (Figure 3.1). It varies from conventional photogrammetry in that the geometry of the scene, camera locations, and orientation are automatically solved without the requirement to provide a network of targets with known 3-D coordinates a priori. Instead, a highly redundant, iterative bundle adjustment technique based on a database of characteristics automatically derived from a collection of numerous overlapping photos is used to solve them all at once (2008, Snavely). This technique, which was developed in the 1990s, has its roots in the computer vision community (e.g., Spetsakis and Aloimonos, 1991; Boufama et al., 1993; Szeliski and Kang, 1994) and the advancement of automatic feature-matching algorithms the decade before (e.g., Förstner, 1986; Harris and Stephens, 1988). The technique has gained traction due to a number of cloud-processing engines which employs SfM approaches described by Snavely (2008). These systems may directly employ user-uploaded and crowd-sourced photography to produce the required coverage of a target location, as well as generate sparse 3-D point clouds from these photosets.

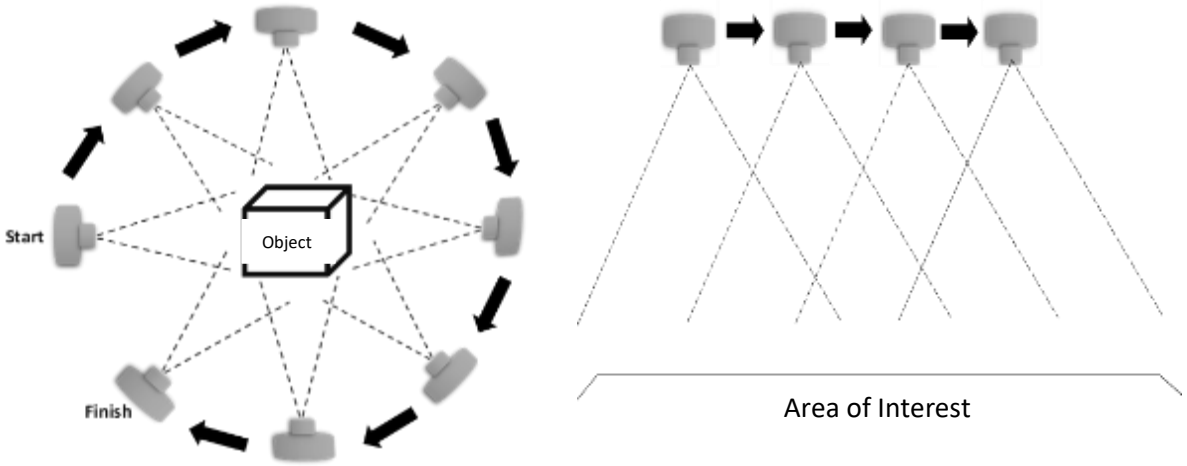

Figure3.1. the two image capture methods used in photogrammetry. The convergent method on the left shows how to acquire overlapping photos around an object of interest, while the plane method on the right shows how to acquire overlapping images at a continuous flight height.

Traditional softcopy photogrammetric approaches need the 3-D position and posture of the camera(s) or the 3-D location of a sequence of control points to identify the 3-D location of points inside a scene. In the case of the former, triangulation can be used to rebuild scene geometry in the absence of a camera-mounted GPS and electronic compass, whereas in the case of the latter, control points are manually recognized in the input photographs and a procedure known resectioning, or camera pose estimation, is used to evaluate camera position. The SfM technique, on the other hand, does not need any of the aforementioned to be known prior to scene reconstruction. The automated recognition of matching characteristics in numerous photos is used to recreate the camera orientation and scene geometry at the same time. These characteristics are tracked from image to image, allowing for initial

estimations of camera locations and object coordinates to be revised iteratively using non-linear least-squares minimization (Snavely, 2008).

The camera locations produced via SfM, unlike standard photogrammetry, lack the size and orientation given by ground-control coordinates. As a result, 3-D point clouds are created in an image-space coordinate system that should be aligned to a real-world, object-space coordinate system. In most circumstances, a 3-D similarity transform based on a limited set of known ground-control points (GCPs) with known object-space coordinates may be used to convert SfM image-space values to absolute coordinates. Such GCPs can be generated after the fact by evaluating possible features that are fully evident in both the resultant point cloud and the field, and then getting their coordinates via a ground survey (i.e., by GPS). In fact, although, it is frequently simple to install actual targets in the area with a high contrast and clearly defined centroid before taking photographs. This method facilitates the explicit co-location of image and object space targets, as well as ensuring a dependable, well-distributed network of targets over the region of interest, allowing for the evaluation of any non-linear structural faults in the SfM reconstruction. It's also a good idea to include some redundancy in the GCP network to compensate for the potential of sparse data in the target area.

3.2.2 Structure from Motion Pipeline

A typical SfM pipeline, as shown in Figure 3.2, consists of several processing phases, each of which addresses a particular problem in the reconstruction pipeline. Each stage might use different algorithms to handle the problem at hand, resulting in a large number of distinct SfM pipelines. In the literature, there are numerous SfM pipelines. Incremental SfM, in particular, is a pipeline that comprises of a first step of image correspondences search and a second step of iterative incremental reconstruction. Feature Extraction, Feature Matching, and Geometric Verification are the three processes in the correspondence search step. This step takes the image set as input and produces the Scene Graph or View Graph, which provides geometrically verified image associations. An initialization stage is followed by three reconstruction steps: Image Registration, Triangulation, and Bundle Adjustment in the iterative reconstruction phase. It creates a 3D reconstruction as a sparse point cloud using the scene graph and an estimation of the camera position for each photograph.

3.2.2.1 Correspondence Search

In feature exctraction stage, a collection of local features is built for each image sent into the pipeline to describe the image's places of interest (key points). Different solutions can be employed for feature extraction, and the algorithm used has an impact on the robustness of the features and the effectiveness of the matching phase. After obtaining key points and descriptions, the following stage is to look for correspondences of these points in various photos. Then in feature matching phase, the key points and features extracted via Feature Extraction are utilized to identify whether photographs depict common elements of the scene and are thus partially overlapping. If two points in different photographs have the same description, they may be considered to be the same in the scene in terms of appearance; if two images share a similar set of points, they can be said to depict the same part of the scene. To efficiently compute matches between photos, many methodologies might be utilized. This phase produces a set of overlapping images, at least in pairs, as well as a set of feature correspondences. Because the previous matching step simply checks that pairs of photos appear to have points in common, geometric verification phase of analysis is necessary. It is not guaranteed that identified matches represent true correspondences of 3D points in the scene, and outliers may be present. A geometric transformation

must be found that successfully transfers a sufficient number of common points between photographs. If this occurs, the two photos are regarded geometrically verified, implying that the points correspond to the scene's geometry. Different ways for describing the geometric connection between the images might be utilized depending on the spatial arrangement in which they were acquired.

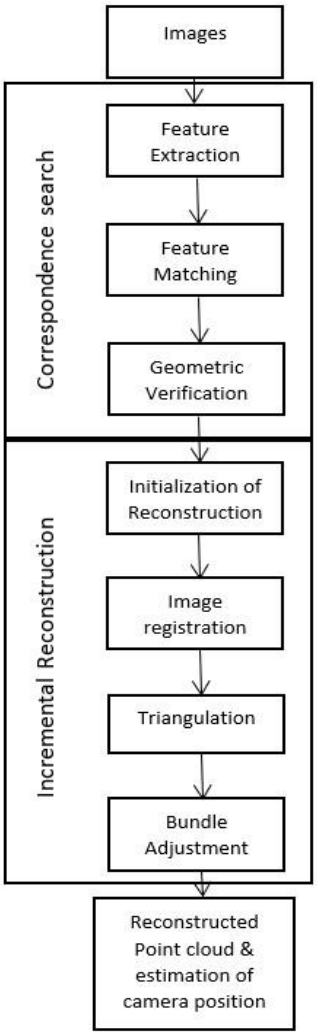

Figure 3.2. Common flowchart of incremental structure from motion algorithm.

Because outliers might contaminate correspondences acquired during the matching phase, robust estimate approaches such as RANSAC (RANdom SAmple Consensus) must be used throughout the geometry verification step. Some of RANSAC's optimizations can be utilized instead of RANSAC to minimize execution times. The Scene Graph, a graph whose nodes represent images and edges join the pairs of images that are regarded geometrically confirmed, is the result of this step of the process. Next step is reconstruction initialization. The initialization of the incremental reconstruction is crucial since a poor initialization leads to a substandard three-dimensional model reconstruction. It is advisable to begin with a dense part of the scene graph in order to ensure that the redundancy of the correspondences offers a firm base for the reconstruction. If the reconstruction begins with a small number of photos, the Bundle Adjustment procedure will not have enough data to adjust the location of the reconstructed camera positions and points, resulting in an accumulation of errors and a poor end result. A pair of geometrically verified photos in a dense area of the scene graph are picked for the reconstruction's initiation. If several photograph pairs could be utilized as a starting point, the one with the most geometrically validated matching points is picked. The initial points of the rebuilt cloud are

the spots that are shared by both images. They're also utilized to set up the first two cameras' positions. Following that, the Image Registration, Triangulation, and Bundle Adjustment processes add new points to the reconstruction iteratively, taking into account a new image.

3.2.2.2 Incremental Reconstruction

The initial stage in incremental reconstruction is image registration. A new photo is contributed to the reconstruction at this step, and it is therefore identified as a registered image. The position of the camera that took the image (position and rotation) must be determined for the newly registered image. This may be accomplished by exploiting the correlation with the reconstruction's known 3D points. As a result, this stage utilizes the 2D-3D relationship between the key points of the newly added photograph and the 3D reconstruction points linked with the key points of the previously registered photographs. To estimate the camera pose, the location must be defined in terms of 3D coordinates of the reference world coordinates system, as well as the rotation (pitch, roll, and yaw axes), for a total of six degrees of freedom. Solving the Perspective-n-Point (PnP) problem makes this achievable. The PnP issue can be fixed using a variety of algorithms. Outliers in the 2D-3D correspondences are frequently present, and the aforementioned algorithms are employed in conjunction with RANSAC (or its variants) to generate a robust estimate of the camera position. The newly recorded image has not yet contributed to the addition of new points and the triangulation phase will do so. Then, next phase would be triangulation. The previous stage identifies a new image that certainly detects points in common with the 3D point that the cloud has so far reconstructed. The new registered image may notice additional new points and such points can be contributed to the three-dimensional reconstruction if at least one previously registered image observes them. A triangulation technique is utilized to identify the 3D coordinates of additional points that may be added to the reconstruction, resulting in a denser point cloud. The triangulation issue starts with a pair of registered images that share points and an estimate of the respective camera positions. it then attempts to estimate the 3D coordinates of each point shared by the two photos. An epipolar constraint is used to tackle the issues of triangulation. The places from which the images were obtained must allow identification of the position of acquisition of the counterpart in the image; these points are known as epipoles. In an ideal situation, the epipolar lines can be used to establish the epipolar plane on which the point whose position is to be evaluated lies. However, due to errors in the pipeline's prior phases, it is probable that the point does not fall at the exact intersection of the epipolar lines; this is known as a reprojection error. Special algorithms that consider inaccuracies are required to overcome this challenge.

Because the determination of camera positions and triangulation can result in inaccuracies in the reconstruction, a strategy for minimizing the accumulation of such errors is required. The Bundle Adjustment (BA) phase's purpose is to avoid inaccuracies in camera position estimation from propagating into cloud point triangulation and vice versa. BA may thus be defined as the refining of the reconstruction that yields optimum condition for the 3D reconstructed points and camera calibration parameters. The Levenberg-Marquardt (LM) algorithm, also known as Damped Least-Squares, is used for BA; it enables the least squares technique to be resolved for non-linear cases. there are a variety of implementations that may be employed. This step is computationally costly and must be performed for each image contributed to the reconstruction. BA can be performed just locally (i.e., for a limited number of photos/cameras, the most connected ones) to save processing time; BA is only performed globally on all images when the rebuilt point cloud has expanded by at least a specific percentage because the last time global BA was performed.

3.2.3 Camera Calibration Parameters

Several parametric lens distortion models are supported by software packages for image processing. In pre-processing, a specific model that best approximates an actual distortion field should be chosen. A central projection camera is assumed in all models. Brown's distortion model is used to model non-linear distortions. The translation from point coordinates in the local camera coordinate system to pixel coordinates in the image frame is specified by a camera model. The camera projection center is the origin of the local camera coordinate system. The Z axis points in the direction of looking, the X axis to the right, and the Y axis to the bottom. The origin of the image coordinate system is at the top-left pixel with coordinates (0.5, 0.5). In the image coordinate system, the X axis points right and the Y axis points down. Pixels are used to quantify image coordinates. At following parts, the calibration coefficients and correlation matrix related to processing of each dataset are represented.

For every supported camera type, the equations needed to project points in the local camera coordinate system to the image plane are listed below.

X, Y, Z: Point coordinates in the local camera coordinate system

u, v: Projected point coordinates in the image coordinate system (in pixels)

f: Focal Length (in pixels)

cx, cy: Principal point offset (in pixels)

K1, K2, K3, K4: Radial distortion coefficients (dimensionless)

P1, P2: Tangential distortion coefficient

B1, B2: Affinity and non-orthogonality (skew) coefficients (in pixels)

w, h: Image width and height (in pixels)

3.2.4 Application of SfM to Historical Imagery

At least once, this method has been used to historical aerial photogrammetry: the University of Porto scanned film archives from 1947 to 1958 1:30000 from Royal Air Force and United States Air Force coverages over Portugal and Spain (Goncalves, 2016). The SfM approach was chosen since prior attempts and traditional application of orthorectification were too costly and difficult. Each collection contains 10 to 12 thousand photographs. They were also lacking the camera calibration certifications in this instance, so they chose 24 photographs as a use case. They executed a similar SfM procedure using an unnamed commercial software package after standardizing the scanned photographs for rotation and size and successfully recovered an orthorectified mosaic and DSM from the data, even in mountainous regions. The DSM height discrepancies between checkpoints ranged from -25m to + 22.7m, with a mean of 1.2 and a 4.7m RMSE. When compared to Open Street Map, the photo alignment was found to be satisfactory. Unfortunately, no information concerning faults or opportunities for development were mentioned, but the approach was found to be adequate for processing huge archives in a timely and cost-effective way.

3.3 Materials and Methods

The purpose of this work is to apply the described methodologies to reconstruct a 3d model from aerial historical photos over a 50-year period covering the Val Veny region (see Chapter 2). The steps to reach this aim are as follows:

3.3.1 Editing Images

For categorization and editing, the images were loaded into Adobe Lightroom. Lightroom is a professional-grade program for managing photography catalogues that is both affordable and user-friendly, in addition to having efficient processing algorithms. As a result, it's frequently employed in scientific photogrammetry for image and lens distortion adjustment. The image adjustments used in this investigation were straightforward and consistent across all photos. In all datasets the clarity and contrast are adjusted according to properties of the images. This procedure increases the SfM software's effectiveness in common-point detection while reducing errors (McNaughton and Cox, 2020).

3.3.2 Alignment

In this work 3D point cloud reconstruction is performed by using Structure from Motion software package Agisoft Metashape (www.agisoft.com). Agisoft Metashape is a stand-alone software package that perform photogrammetric processing on digital photos and provides 3D spatial data for use in GIS applications, cultural heritage documentation, and visual effects generation, as well as for indirect measurements of objects of various dimensions. In Metashape, common photogrammetry processing tasks include creating a 3d model and an orthomosaic. The Agisoft Metashape image data processing approach has three primary steps.

At First, alignment is the initial phase in the process. Aerial triangulation (AT) and bundle block adjustment are included (BBA). During this step, Metashape scans the photos for feature points and matches them among images to create tie points. The application also calculates camera calibration parameters such as interior (IO) and exterior (EO) camera orientation parameters and identifies the camera's location for each image. A sparse point cloud and a series of camera locations are used to illustrate the outcomes of these operations (Figure 3.3). Due to overlapping of image datasets, this step additionally assessed internal camera lens distortion properties and scene geometry using a bundle adjustment with high redundancy. Only points with a reprojection error of less than 0.6 were kept, and evident outliers such as shadow zones behind overhanging cliffs were carefully deleted. The sparse point cloud contains the outcomes of image alignment and will not be directly employed in subsequent processing except in the case of the sparse point cloud-based surface reconstruction approach, which is only useful for rapid estimations, such as data set completeness.

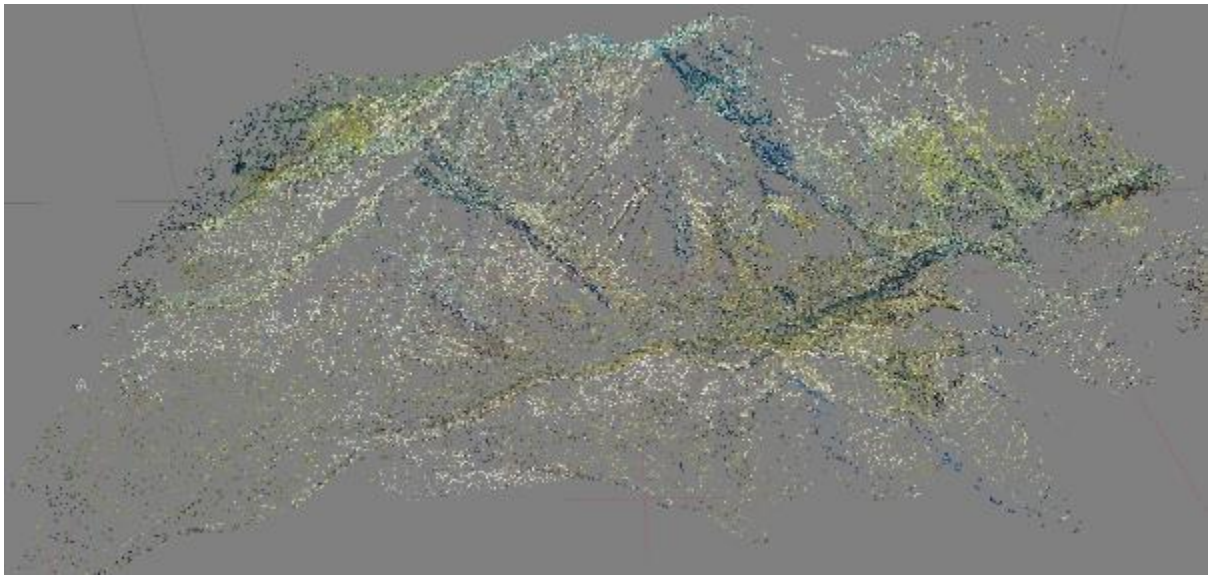

Figure 3.3. Example of sparse point cloud generated after initial alignment

Prior to the more computationally intensive generation of dense point clouds, the user can assess precision and recognize problematic tie points using the sparse point cloud. Each point has its own level of uncertainty. Because points with a lot of uncertainty are more likely to be wrong, it's usual practice to enhance model quality by systematically removing points that don't fulfil particular criteria. Uncertain points were discovered and eliminated using two passes of Agisoft's Gradual Selection tool, with the reconstruction uncertainty level set to 10 (Mayer et al., 2018).

3.3.3 Georeferencing

Georeferencing is the procedure of applying a transformation technique to convert a model's local coordinate system to a global coordinate system. The model is now scaled and placed correctly in the global coordinate system. This is required in order to compare a model to other models from another period of time, compare it to a model created using a different approach, and perform area and volume analyses. In all of the models in this work, the global coordinate system WGS 84/UTM zone 32N is used. The main issue is lack of ground control points in the archive photos to utilize for georeferencing. To solve this problem, ground control points are chosen as objects that are stable over time and across all datasets, such as buildings or crossroads, and their coordinates are determined using accessible satellite data. The georeferencing error between multiple models will be minimized if the same points are reliably picked for georeferencing in all datasets and points are distributed well enough on the model. The challenging issue is to minimize the relative error of georeferencing between models in order to limit the ultimate error in the comparison of two models as much as feasible.

In picking the points procedure to use them as georeferenced points, it is important to avoid picking them to be distributed in a line. They should be distributed over the whole area as much as possible (Figure 3.4). The problem in all dataset is the absence of enough stable points in the area to be selected as ground control points. The building and houses are available only inside the city and in the bottom of the valley and there are no stable parts in the northern part of glaciers to be selected as ground control points. Then, it is possible only to distribute the ground control points within the city and valley. However, in some dataset, the northern part of glaciers is available to be used as ground control points.

Figure 3.4. Example position and distribution of GCP's over the Val Veny mountains in one of the datasets

3.3.4 Assessment of Alignment Result

The residuals of the control points are provided by the bundle adjustment, which indicate the difference between measured coordinates and newly calculated values (based on the estimated exterior orientation parameters and measured image coordinate values). Errors in the photogrammetric network of observations (due to incorrectly measured control points, data input errors, poor control point quality, or bad camera calibration) are indicated by relatively large residual values. Large residuals in control points were modified or deleted until an optimal solution was found. This is a technique that is both participatory and subjective. In general, residuals bigger than the measurement's pre-defined standard deviation were seen as questionable. Nevertheless, removing too many control points might reduce the photogrammetric model's validity, especially if numerous parameters were to be estimated. It was justifiable to tolerate greater residuals if there were apparent explanations for errors, such as inadequate camera calibration (Walstra ,2006).

3.3.5 Optimization of Camera Alignment

The Optimize Cameras command applies a comprehensive bundle adjustment method to the aligned photogrammetric block, revising exterior and interior camera orientation parameters as well as triangulated tie point coordinates at the same time. All relevant measures and precisions, such as image projections of tie points and markers, GCP coordinates, and so on, are used to make adjustments. Following adding or updating measured values or their accuracies, such as adding GCPs or modifying accuracy settings, it is critical to always optimize cameras to guarantee maximum geometric accuracy of processing outputs.

3.3.6 Dense Cloud Generation

The next stage is to create a 3D (mesh) and/or 2.5D surface (DEM). The polygonal model (mesh) may be textured for a photorealistic digital representation of the object/scene and exported in a variety of formats appropriate for post-processing tools, which can be used in both CAD and 3D-modeling processes. Metashape can build tiled models for city-scale applications to give quick model representation response and smooth navigation over the whole area. The original resolution of the photos applied to the model as a texture is preserved in this hierarchical form, which is compatible with both standalone and web-based viewers. Metashape can create a dense point cloud based on the predicted camera locations and the photos themselves (dense stereo matching). The depth maps computed via dense stereo matching are used to generate dense point clouds. For the overlapping image pairs, depth maps are produced using bundle adjustment to determine their relative exterior and interior orientation components. Multiple pairwise depth maps created for every camera are integrated into a combined depth map, with extra information in overlapping locations used to filter out incorrect depth measurements. The camera's combined depth maps are turned into partial dense point clouds, which are then blended into a final dense point cloud with further noise filtering done in overlapping locations. After that, the dense cloud was modified to eliminate points that were not on solid surfaces, such as supraglacial lakes, as well as visible outliers (Figure3.5). All procedures were carried out in a high-quality setting.

Figure 3.5. Point clouds were generated and manually modified to eliminate points that were not belong on solid surfaces (e.g., supraglacial ponds)

Then it is possible to create an Orthomosaic that may be georeferenced and utilized as a basis layer for many types of maps, as well as for post-processing assessment and vectorization. Orthomosaics are created by projecting pictures onto a surface of the user's choice.

3.3.7 Accuracy assessment

Many studies have been conducted to assess the accuracy of the Agisoft Metashape process and 3D reconstruction with or without GCPs, as well as the quality of the model created for area and volume calculations. for instance, the research by (Maraş., 2021) was to see how well a 3D photogrammetric model without GCPs operated and how sensitive it was (Ground Control Points). Two distinct tests are conducted in two places with diverse features such as altitude, slope, topography, and meteorological variants to evaluate if the models without GCPs demonstrate accuracy in all sorts of terrain as well as climatic or metrological situations. GCPs were used to simulate the research regions at first, and then

they were removed. In addition, for accuracy analysis, some of the dimensions and regions inside the simulated area were surveyed using terrestrial approaches (using GPS/GNSS). Varying territories with different slopes and geometric forms were selected after modelling inside the areas with and without GCPs. The results of the length measurement revealed varying levels of success. The first research area showed promising outcomes in length measuring, with a relative error of less than 1%. In the instance of area measurement, a minimum relative error of 0.04% and a maximum relative error of 1.05% were recorded in the first research area. A lowest relative error of 0.56% and a maximum relative error of 5.27% are reached in the second study regions for area measurement. Finally, in the case of volume measurement, a minimum relative error of 0.8% and a maximum relative error of 6.8% are determined for the first study area. In this study, the ultimate aim is comparison of 3D models and find the variations of glaciers. Then, for GCPs, steady points from all datasets are employed. Although the precision is in the order of 1 or 2 meters, the acceptable accuracy can be verified at the 3D reconstruction stage, and models must be co-registered before the final comparison.

3.4 Result and analysis

The approach described in the preceding section was applied to process all of the datasets. For datasets including images from several cameras, a pre-calibration procedure is used before alignment. Except for the data from 1967, all datasets had pixel size and focal length information. In addition, for image sets containing camera position coordinates, the Reference preselection approach was combined with the general preselection method for alignment. In the sparse model, high-quality alignment is used, and stationary tie points are excluded. GCPs are chosen in a way that they have at least two projections on the images and are spread out as much as feasible throughout the whole region, avoiding linear distribution.

3.4.1 Dataset of 2006

This is the newest dataset available in this work and the images in this dataset are obtained by digital camera. It contains 78 images and camera station that covers 97.6 km^2 of Val Veny. In this case the camera coordinate and georeferencing data are absent. In the alignment process, 103,270 tie points were obtained for this dataset.

Also, the camera stations over the whole area are found and number of overlapping of images in each zone can be illustrated in figure 3.6. The highest overlapping is at the center part of the region and lowest overlapping are at the side zones of area in north, east and west sides. Then some gaps between the points of 3D model is expected at those zones.

As it is obvious from figures, the model is complete from west side of Miage glacier to East side of Brenva glacier except the middle part of Brenva and Miage glaciers that are affected by shadows and probably point density is lower.

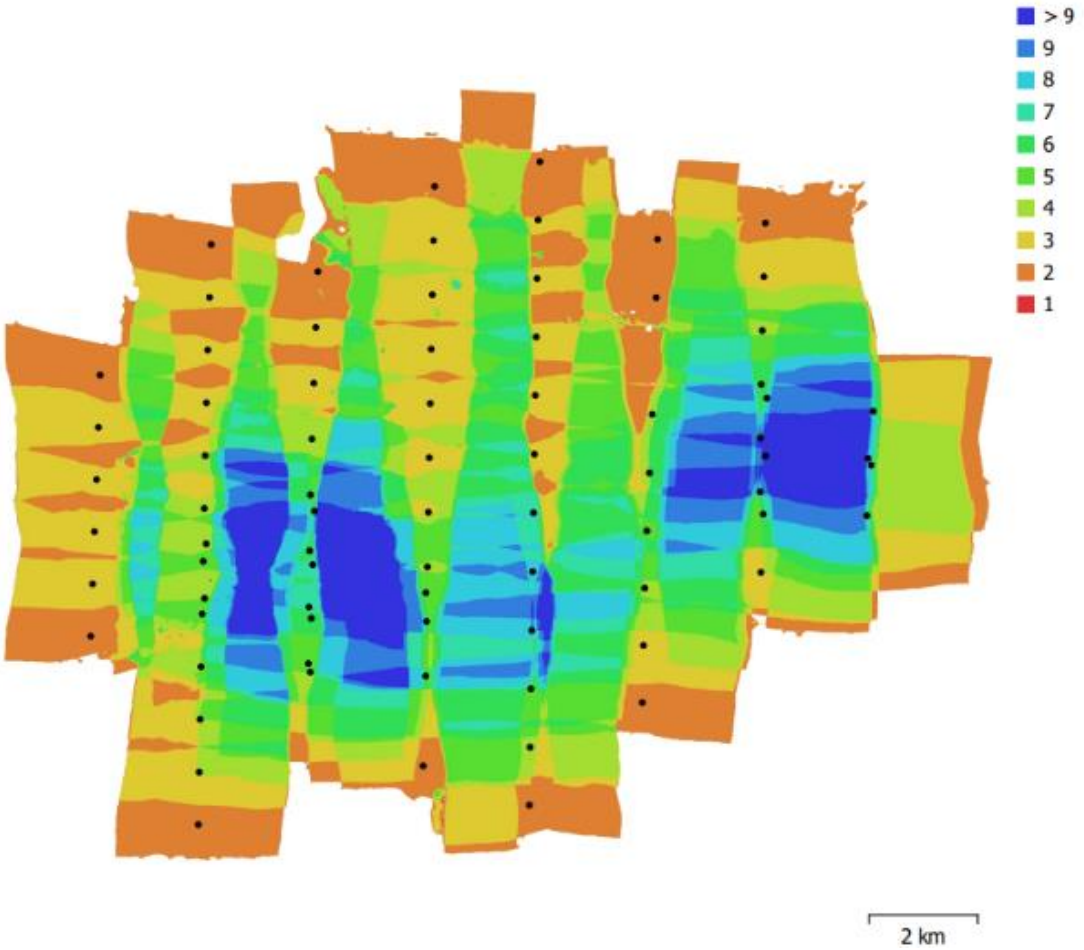

Figure 3.6. Distribution and location of cameras and overlapping map of the images of 2006.

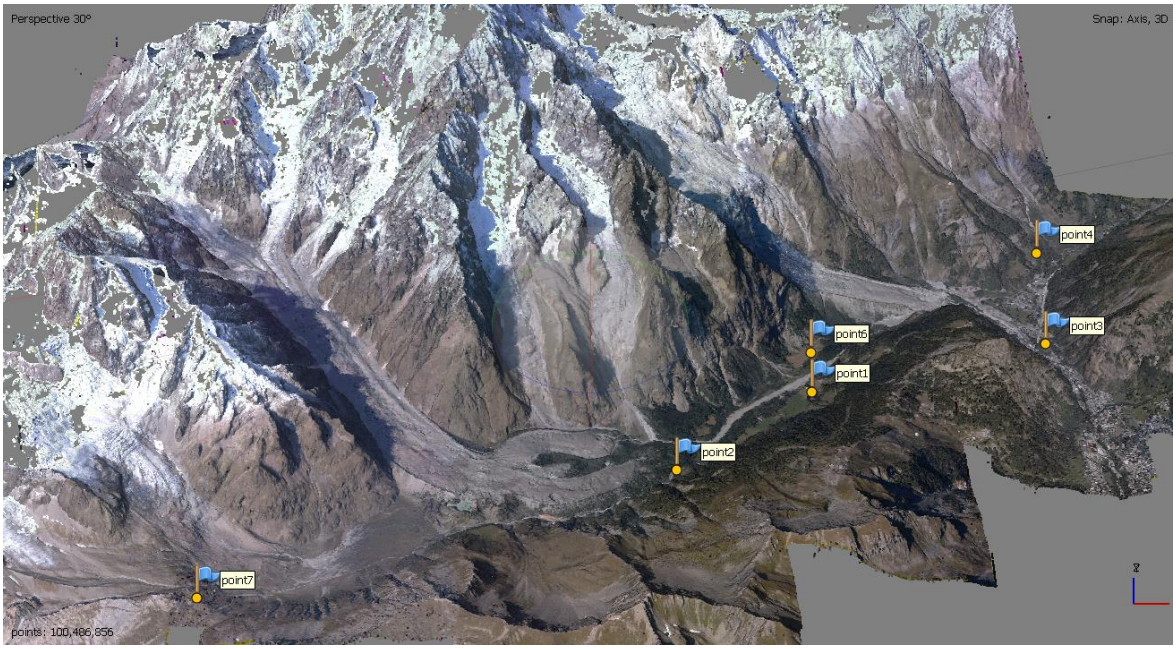

Figure 3.7. Area of interest in 3D dense cloud from 2006 dataset, Location and distribution of GCP's for dataset 2006.

Camera Stations	Focal length [mm]	Pixel size [μm]	Resolution [mm]	Ground Resolution (cm/pix)	Tie Points	Dense Cloud points
78	59.95	9 x 9	4096 x 4096	82.5	103,270	100,486,856

Table 3.1. Properties of the images and 3D model reconstructed for dataset 2006.

3.4.2 Dataset 2001

This dataset contains 73 images that are obtained with a flying altitude of 4.78 km to cover about 345 km^2 of area. The camera model used is RMKTOP 15, focal length is 153.023mm and pixel sizes are 28 x 28μm. In contrast with previous dataset, here camera coordinates are shown in side information of each image (figure 3.9) in Degrees Minutes that should be converted to UTM coordinates to be consistent with satellite data that are used for georeferencing. Additionally, fiducial marks can be used as well for the alignment procedure. Then in this case the alignment procedure can be done either using fiducial marks or maskin them out. In this case, masking out the fiducials results in better alignment and denser point cloud.

Alignment procedure results in 88,191 tie points and Calibration parameters and correlation matrix is obtained. The camera locations and overlapping in each zone are obtained after alignment. As the camera coordinates are known, the alignment is done with reference to preselection source. As in this dataset camera coordinates are available the position of cameras is known. After camera optimization the dense cloud is produced with more than 220 million points. In this situation, due to the broader coverage, it was also feasible to choose certain GCPs in the north-east side of the valley to disperse more GCPs. Because of the higher overlapping of cameras and the higher number of photos in this 3D model, the center region is much denser.

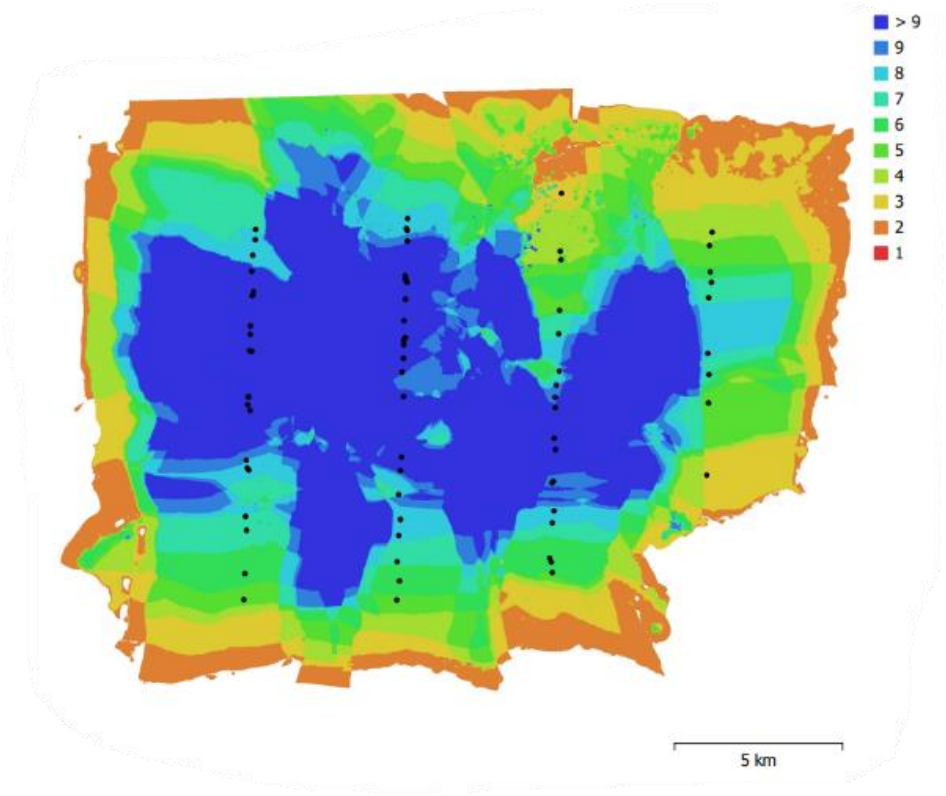

Figure 3.8. Distribution and location of cameras and overlapping map of the images of 2001.

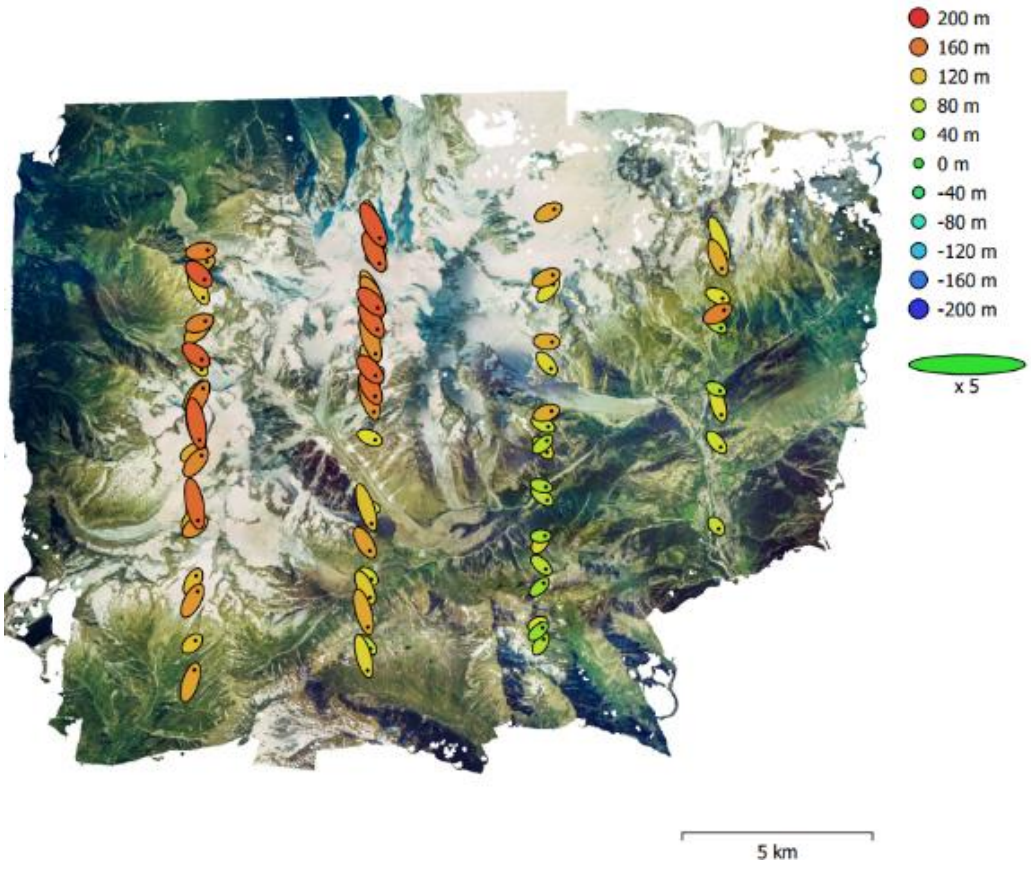

Figure 3.9. Distribution and location of cameras according to image coordinates of the dataset 2001.

Figure 3.10. Area of interest in 3D dense cloud from 2001 dataset, Location and distribution of GCP's for dataset 2001.

Camera Stations	Focal length [mm]	Pixel size [µm]	Resolution [mm]	Ground Resolution (cm/pix)	Tie Points	Dense Cloud points
73	153.023	28 x 28	7744 x 7799	75.6	88.191	223,706,568

Table 3.2. Properties of the images and 3D model reconstructed for dataset 2001.

3.4.3 Dataset 2000

In this dataset there are 25 images which were obtained with a flying altitude of 5.54 km with camera RMKTOP15. These images can lead to a 3D model that covers 310 km^2. In this situation, likewise, camera coordinates are known. Fiducial markers can also be utilized for alignment, however after comparing the results of processing with and without fiducial marks, masking away the fiducials produced superior results. The position of the cameras was previously known using the image coordinate reference. Because image overlapping is maximum at the center regions heading to the Miage glacier, a denser model is reconstructed at the Miage region. Some holes exist in the upper portions of the Brenva, Freney, and Brouillard glaciers, but the lower parts are dense enough. Only the Val Veny portion is dense and complete in proportion to the number, distribution, and location of the cameras, whereas the rest of the region has several gaps between sites.

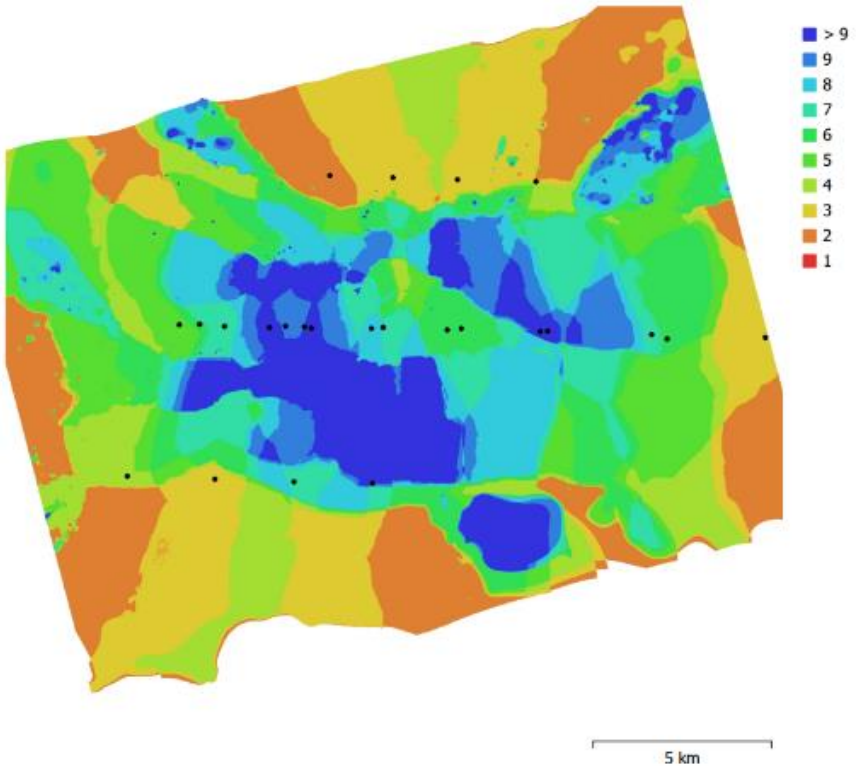

Figure 3.11. Distribution and location of cameras and overlapping map of the images of 2000.

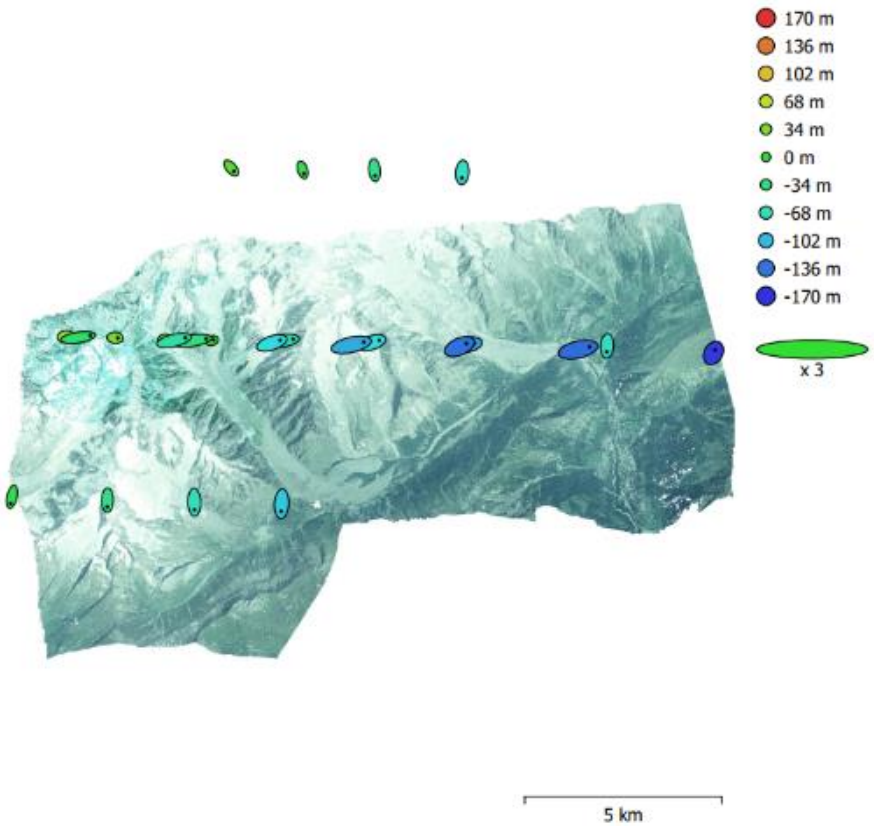

Figure 3.12. Distribution and location of cameras according to image coordinates of the dataset 2000.

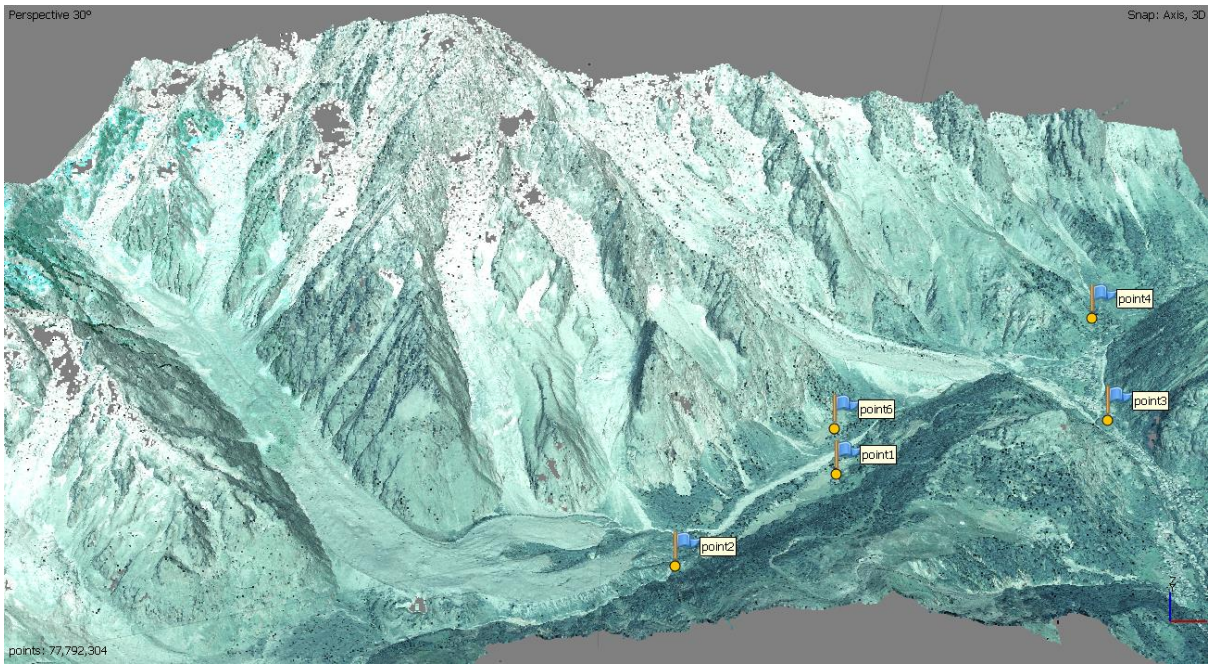

Figure 3.13. Area of interest in 3D dense cloud from 2000 dataset, Location and distribution of GCP's for dataset 2000.

Camera Stations	Focal length [mm]	Pixel size [μm]	Resolution	Ground Resolution (cm/pix)	Tie Points	Dense Cloud points
25	153.023	28 x 28	9076x8325	90.2	29,725	77,792,304

Table 3.3. Properties of the images and 3D model reconstructed for dataset 2000.

3.4.4 Dataset 1996

This dataset contains 35 photographs from two separate cameras: 27 images taken with the RMK TOP 15 camera type, which has a certificate, and 8 images taken with another camera, which does not have a certificate. The 8 photographs acquired by separate cameras will not be aligned with the other 27 images if the conventional methodology is followed. To overcome this issue, two groups are aligned independently in two chunks, and then the camera calibration properties are exported. Pre-calibration parameters will indeed be based on the calibration data of two groups of images.

Second, GCPs can be placed into the images, and the goal is to locate the GCPs that are common by the 8-image group and the 27-image group. This method leads to the processing of all 35 photos being aligned. These 35 photographs cover a total area of 301 km^2, with 27 of them taken from a height of 5.02 meters. The camera coordinates for these 27 photographs are known, and fiducial markers can be used based on the certificate, but because the objective is to align all 35 images and there is no certificate for the remaining eight, all fiducial marks should be masked.

In this scenario, the overlapping in the Val Veny area is sufficient, resulting in a dense 3D model. However, the existence of shadows has an impact on the procedure's ultimate outcome, as the highest areas of the Brenva Glacier are not precisely reproduced and include certain discrepancies. (Figure 3.14).

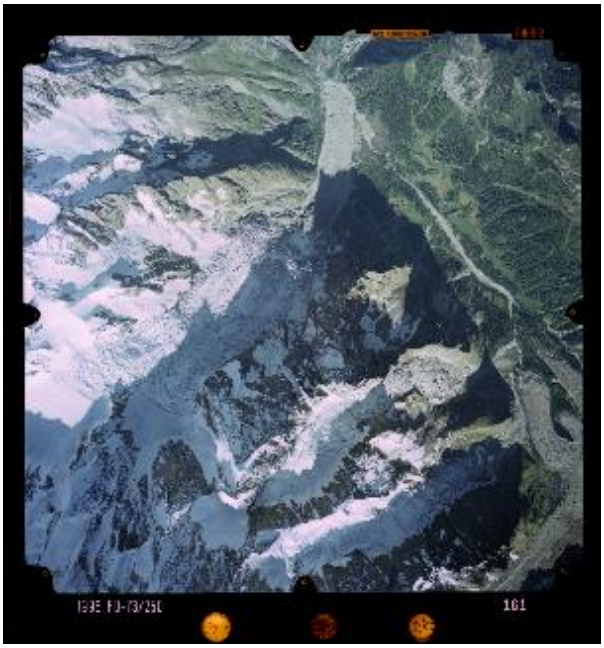

Figure 3.14. Effect of shadows on the Brenva glacier that avoid proper point extraction and 3D reconstruction in dataset of 1996.

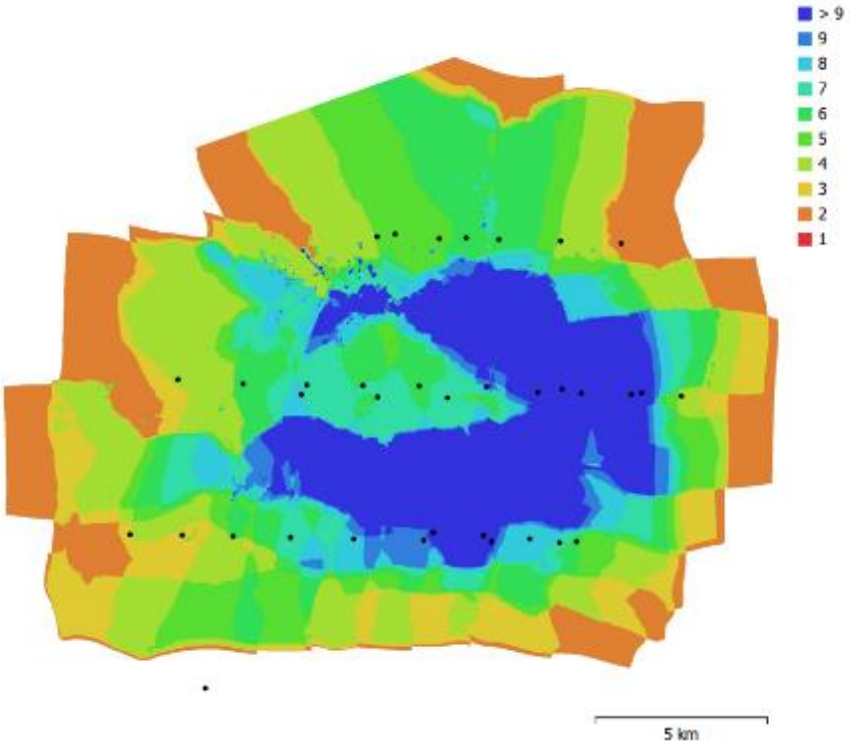

Figure 3.15. Distribution and location of cameras and overlapping map of the images of 1996.

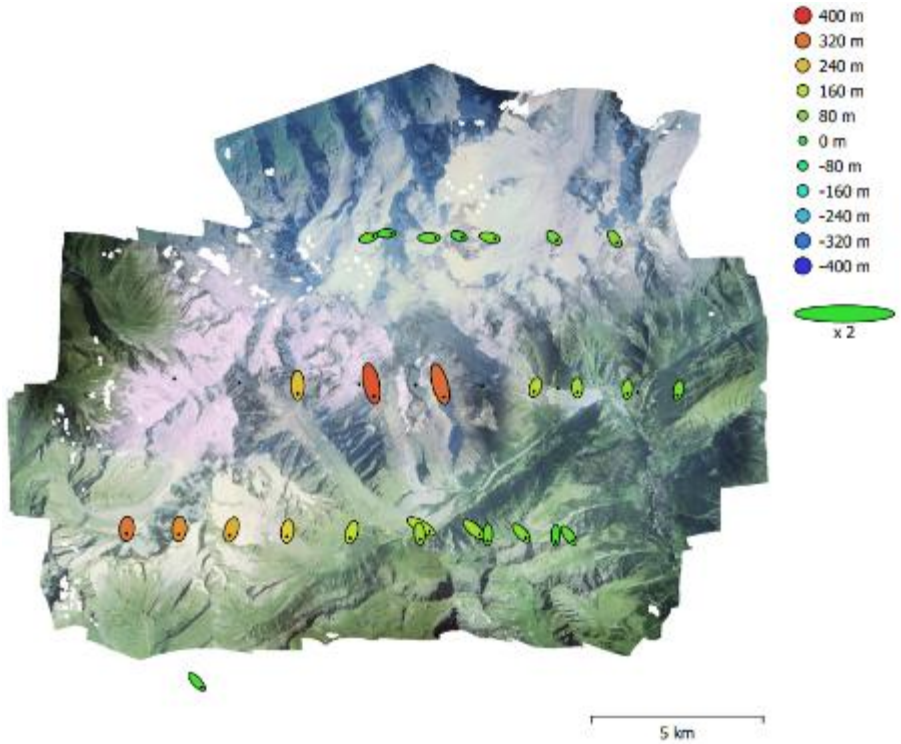

Figure 3.16. Distribution and location of cameras according to image coordinates of the dataset 1996.

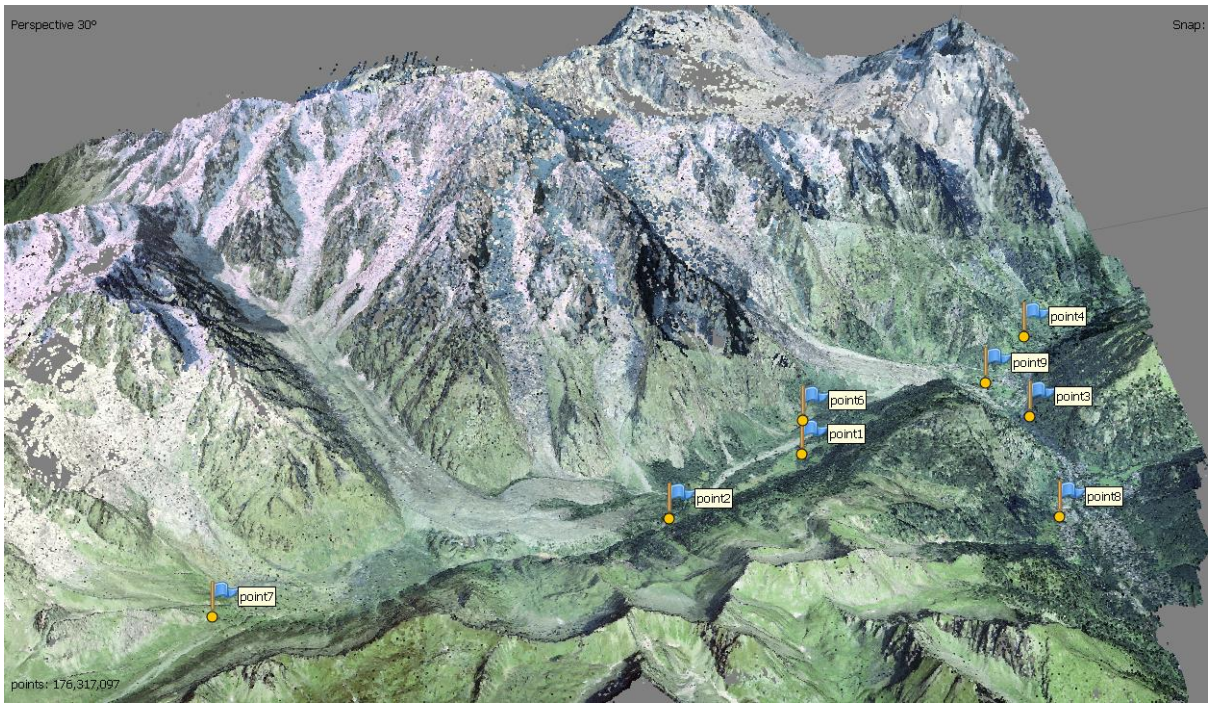

Figure 3.17. Area of interest in 3D dense cloud from 1996 dataset, Location and distribution of GCP's for dataset 1996.

Camera Stations	Focal length [mm]	Pixel size [μm]	Resolution	Ground Resolution (cm/pix)	Tie Points	Dense Cloud points
35	153.466	28 x 28	8673 x 9324	76.7	46,616	176,317,097

Table 3.4. Properties of the images and 3D model reconstructed for dataset 1996.

3.4.5 Dataset 1988

There are 23 photographs in this set that were taken from a flying height of 6.18 km with the camera RC 10, and the model covers an area of 277 km^2. The certificate is provided, and photographs may be aligned using fiducial markings. No obvious differences were found in the modelling of this dataset with or without using fiducial markers. The overlapping in this case is not as good as in previous datasets, but the absence of shadows results in a good quality 3D dense cloud in the valley section, where there are the most overlaps. However, due to decreased overlapping, some areas of the region were reconstructed with considerable irregularity.

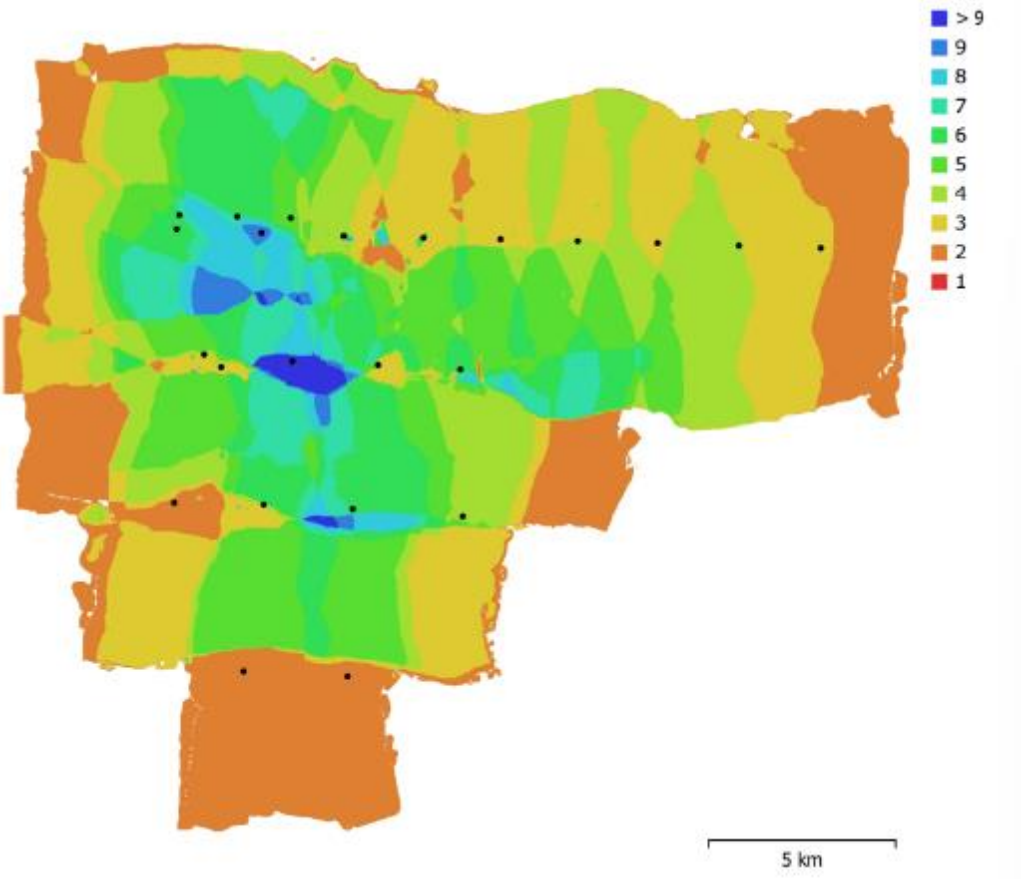

Figure 3.18. Distribution and location of cameras and overlapping map of the images of 1988.

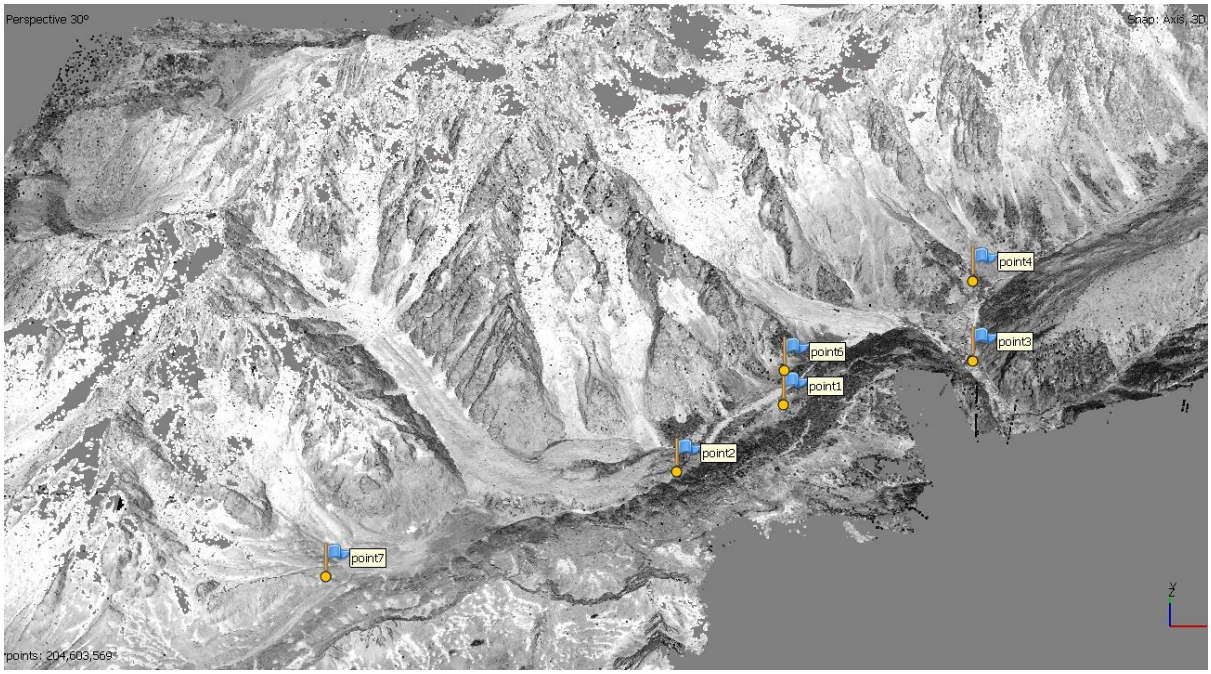

Figure 3.19. Area of interest in 3D dense cloud from 1988 dataset, Location and distribution of GCP's for dataset 1988.

Camera Stations	Focal length [mm]	Pixel size [μm]	Resolution	Ground Resolution (cm/pix)	Tie Points	Dense Cloud points
23	152.06	21.1x21.1	11232x12089	73.8	27.851	204,603,569

Table 3.5. Properties of the images and 3D model reconstructed for dataset 1988.

3.4.6 Dataset 1979

It contains 19 photos captured by the Wild RC 10 camera at a height of 5.7 kilometers and a surface area of 144 square kilometers. The photos certificates allow for the use of fiducial markers, but the camera coordinates are missing. This is the only dataset in which utilizing fiducial markers in the alignment operation results in an increased number of aligned images and a denser 3D model.

The overlapping in the east part of the valley approaching the city is extremely low and insufficient, causing the bottom portion of the Brenva Glacier to be missed. The top sections of Brenva and other glaciers, on the other hand, were fully represented and with sufficient density. Overall, many gaps exist in 3D model reconstruction due to the low number of photos and vast coverage area, particularly in zones outside the valley where appropriate camera overlapping is lacking.

Figure 3.20. Distribution and location of cameras and overlapping map of the images of 1979.

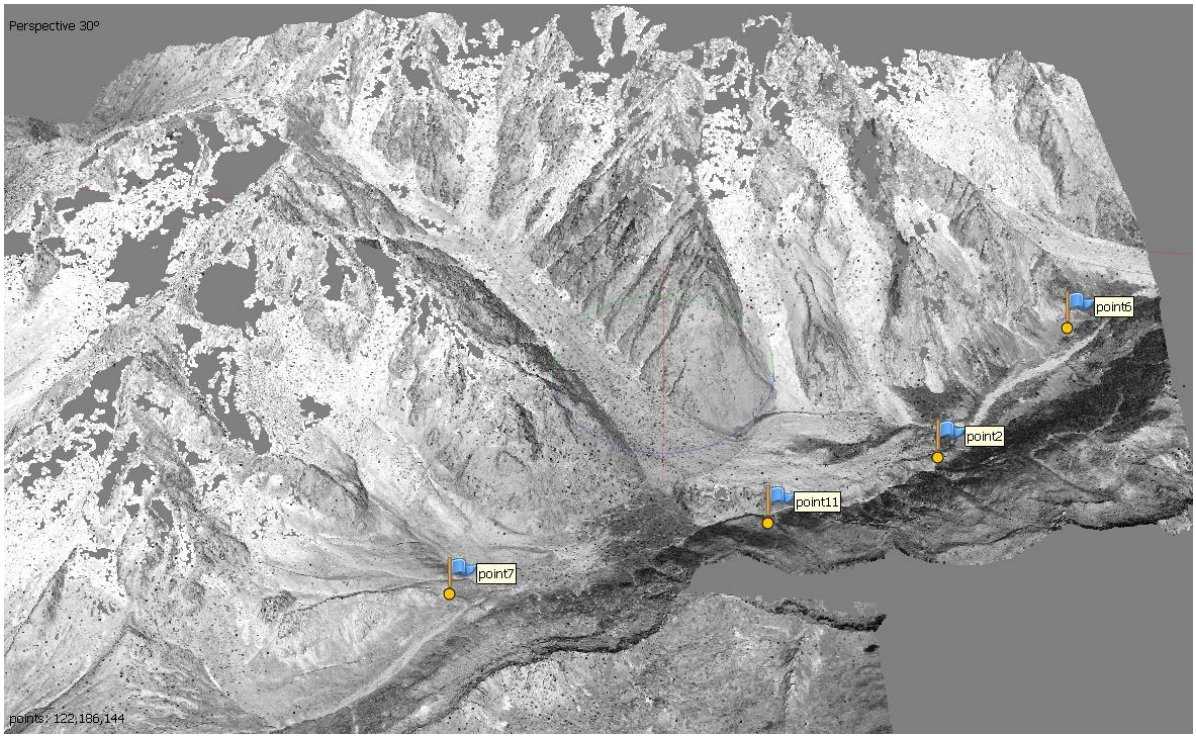

Figure 3.21. Area of interest in 3D dense cloud from 1979 dataset, Location and distribution of GCP's for dataset 1979.

Camera Stations	Focal length [mm]	Pixel size [μm]	Resolution	Ground Resolution (cm/pix)	Tie Points	Dense Cloud points
19	153.179	21x21	11285x12142	68.3	18,784	122,186,144

Table 3.6. Properties of the images and 3D model reconstructed for dataset 1979.

3.4.7 Dataset 1967

Because it is the oldest dataset in this study and because there is no certificate for it, using fiducial markers is unfeasible, and they should be masked off. It comprises 24 photographs covering 132 km^2 at a flying altitude of 6.35 km. The existence of mountain shadows is troublesome in this dataset, and the 3D dense cloud has gaps in some parts of the model, particularly at the top regions of the Miage glacier. Furthermore, the low number of overlapping sections exacerbates the problem by making the model less dense in most areas. However, other glaciers and lower parts of Miage are completed and have enough density.

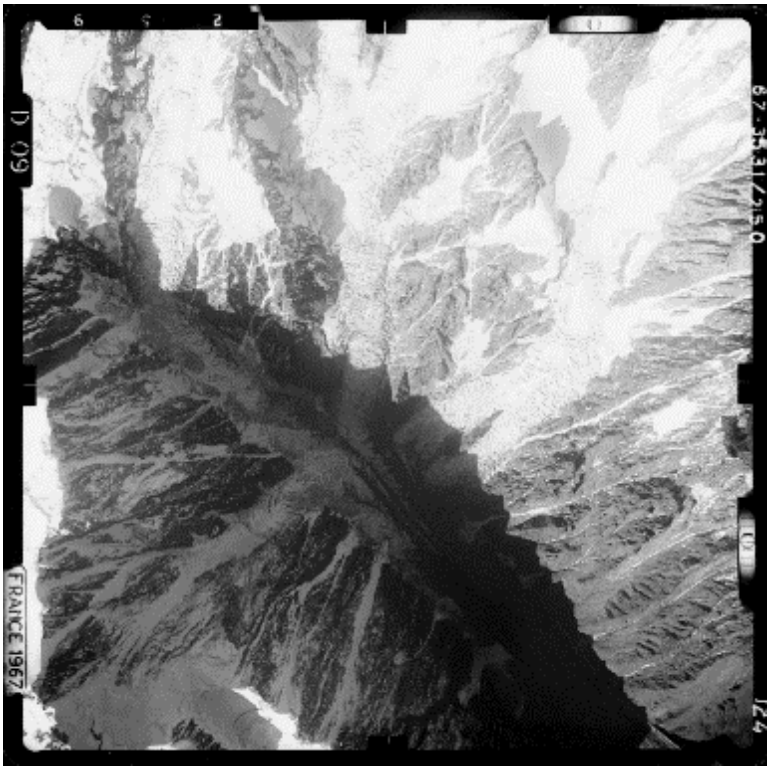

Figure 3.22. Effect of shadows on the upper parts of Miage glacier that avoid proper point extraction and 3D reconstruction in dataset of 1967.

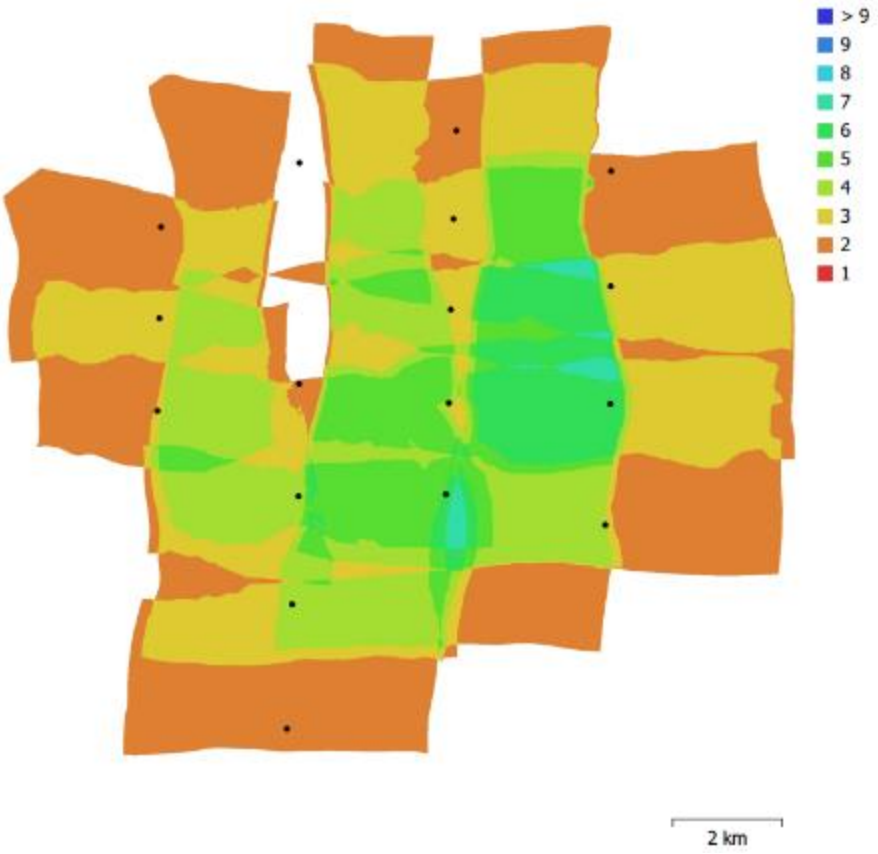

Figure 3.23. Distribution and location of cameras and overlapping map of the images of 1967.

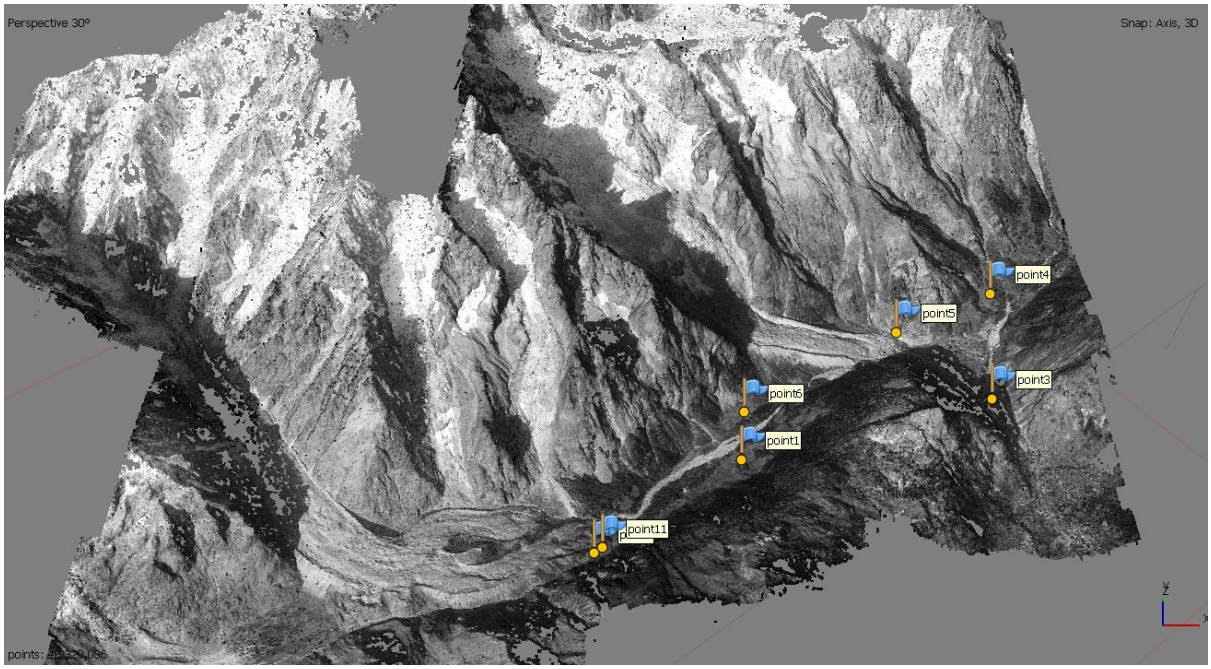

Figure 3.24. Area of interest in 3D dense cloud from 1967 dataset, Location and distribution of GCP's for dataset 1967.

Camera Stations	Focal length [mm]	Pixel size [μm]	Resolution	Ground Resolution (cm/pix)	Tie Points	Dense Cloud points
24	153	21x21	5396x5396	99.5	26,088	48,320,086

Table 3.7. Properties of the images and 3D model reconstructed for dataset 1967.

3.5 Point cloud analysis

The point density study reveals considerable disparities between the 3D reconstruction through the years (Table 3.8). Depending on the surveying method which were aerial photography for all, values varied from 0.439 to 0.889 points/m^2, although the density was typically sufficient for the reconstruction of the various surfaces. The maximum point density was found in the 1988 dataset, whereas the lowest was found in the 1967 3D model. Similar point densities were discovered in all sample locations as the same method of capturing were used for all of them, notably for the standard deviations, which were always in the 0.2 to 0.4 point/m^2 range. Compared to more recent models collected with powerful cameras and specifically for 3D reconstruction applications, the point densities are low in regard to the purpose of the captured photographs at the time of operation, flying height of the cameras, and the size of the area.

year	**Number of points in sample window**	**Mean of point density [point/m^2]**	**Standard deviation [point/m^2]**
2006	617k	0.474	0.229
	645k	0.504	0.275
	1319k	0.631	0.329
2001	486k	0.532	0.293
	990k	0.615	0.377
	1224k	0.773	0.422
2000	331k	0.433	0.179
	337k	0.658	0.390
	557k	0.656	0.366
1996	709k	0.570	0.295
	567k	0.660	0.375
	703k	0.724	0.410
1988	739k	0.608	0.322
	614k	0.890	0.473
	895k	0.808	0.403
1979	980k	0.889	0.484
	684k	0.660	0.871
	531k	0.796	0.427
1967	215k	0.460	0.266
	216k	0.511	0.304
	246k	0.439	0.224

Table 3.8. the mean of point density of sample windows extracted from reconstructed 3D point clouds in different years.

In terms of spatial coverage, the entire area covered by aerial photogrammetry methods ranges from 130 to 345 km^2, though the concentration of overlapping between photos is largely near the city

at the valley's downstream parts, with data gaps on the vertical and sub-vertical cliffs. The point cloud derived from the photos covers regions that are inaccessible using other photogrammetry approaches which most likely present higher spatial resolutions.

It is also likely that, while three GCPs are the technically required minimum for SfM photogrammetry, there are other factors determining the level of error. The flight parameters, image quality, resolution, image blur, flight plan, and so on as well as the processing approach including error reduction, or the software's capacity to estimate the scale with fewer GCPs, could all have an effect on the results. As a result, it is possible that the acquisition hardware and processing methods will have a stronger impact on defining the GCP requirements. Overall, the outcomes in all cases are pretty similar. When processing with self-calibration, the optimal number of GCP to make an adequate precision orthomosaic and DTM is 8 GCP to obtain accuracy of 1m to 2m for X, Y and Z.

Year	Count	X error (m)	Y error (m)	Z error (m)	XY error (m)	Total (m)
2006	8	1.293	0.704	1.380	1.473	2.018
2001	10	0.570	3.156	0.331	3.208	3.225
2000	9	1.328	2.429	0.679	2.768	2.850
1996	8	1.465	3.239	2.453	3.556	4.320
1988	8	1.486	4.300	0.693	4.550	4.603
1979	8	2.480	1.789	0.197	3.058	3.064
1967	6	0.218	0.941	0.939	0.965	1.347

Table 3.9. number of GCP's employed in each model and the RMSE in X-easting, Y-Northing and Z-altitude.

In practice, adding more GCP makes the survey more difficult and expensive. These elements, on the other hand, enable the production of higher-quality products. It is important to note that this methodology may not produce the same results when used with different equipment over very different region characteristics than those described in this research, as well as when performing different flight configurations.

3.6 conclusion

The purpose of this research was to reconstruct 3D models using 7 datasets containing photographs of Val Veny's glaciers over the duration of five decades, and then use the reconstructed model to assess glacier changes in the following sections. Before the image processing, some pre-processing was performed to confirm that the images were prepared for the alignment procedure. The georeferencing procedure was also carried out using satellite data and applying it to stable parts of the images, with the same GCP's being used for all datasets to provide the same georeferencing precision and alignment for a more accurate comparison afterwards. The following are the chapter's primary findings:

- Where there are high cliffs, the influence of shadows might degrade the quality of the reconstructed model, thus photography should be conducted when there are no shadows in the region.
- Image pre-processing improves the extraction of key points and, as a result, image alignment, especially for older photos.
- For datasets involving images from various cameras, it is preferable to pre-calibrate each group of cameras in its own file and then employ the pre-calibration data for image alignment.
- Despite the fact that fiducial marks were present in all datasets for use in the alignment procedure, masking fiducial markers resulted in a better alignment procedure and better final 3D models.

The accessible 3D models derived from historical photographs may be used to examine glacier movements and identify possible hazards. To aid in risk management in the region, a consistent continuous monitoring system might be built, including sending alerts and assisting mountain guides in changing hiking and skiing routes as needed. The research of glacier thickness fluctuations reveals a feedback system that requires more investigation, with higher retreat rates resulting in more collapses. Glacier down waste is particularly significant for risk reduction in the protected area since it offers valuable information for analysing the increased risk of rockfalls and enhancing glacier meltwater production estimates.

Chapter Four

4. Assessing the Evolution of Glaciers

4.1 Introduction

The process of detecting changes between paired photos from the same location by monitoring them at various times is known as change detection (L.T. Luppino., 2017). It's often employed to determine between interesting distinctions, such as changes caused by natural disasters and building reconstruction. As a result, change detection is an important topic in a variety of important applications, such as urban development plans, real-time environmental monitoring, land cover transitions, resource inquiry, disaster damage assessments, and so on. When monitoring the environment, there are four characteristics of change detection that are crucial to consider (S. Pathak., 2014): (1) Detecting the changes that have happened; (2) determining the type of the change; (3) determining the change's area extent; and (4) determining the change's trend. Various strategies have been efficiently developed and applied in the above-mentioned applications in relation to these change detection challenges. Also, the concentration of problem is different with examining different data sources, which results in that several methods are developed to handle change detection problem. There are roughly two sorts of viewpoints for identifying land cover changes: street view (K. Sakurada., 2017) and remote sensing (V. Walter.,2004). The utilization of street view data for dynamic or real-time change detection might offer more specific information on relatively limited regions. However, Remote sensing view is a reliable approach for earth surface monitoring and inspection since remote sensing data covers broad regions with sufficient information for analysis, and the vast amount of effort is involved in the research of remote sensing image evaluation. High-resolution satellite imaging, hyperspectral photos, aerial photographs, synthetic aperture radar (SAR) images, geographical information system (GIS) images, and other types of data are all included in remote sensing data (T. Lillesand.,2014; Y. Zhang., 2015; C. Wu., 2013).

To identify variations in aerial photographs, numerous methodologies and approaches have been developed and deployed. However, the availability and fusion of many sorts of valuable and profitable remote sensing data, such as data generated from Digital Elevation Models (DEM), Light Detection and Ranging (LiDAR) technology, and other types of remote sensing technologies, prompted all of these methodologies (J. D. Kiser., 2012). DEMs are especially effective for detecting glacier thickness and volume fluctuations (Fischer et al., 2015; Berthier et al., 2016), as well as identifying steep slopes that are more susceptible to geomorphodynamic variations, including mass movements (Fischer et al., 2015; Berthier et al., 2016). (Blasone et al., 2015). Most cryospheric hazards might well be identified using multispectral photos with adequate spatial resolution (Quincey et al., 2005; Kääb et al., 2005b). While satellite images from Landsat and ASTER sensors (15-30 m ground sample distance - GSD) are useful for regional-scale mapping (Rounce et al., 2017), hazard assessment at the scale of individual glaciers or basins necessitates a higher spatial resolution, which was previously only possible through aerial laser scanner/photogrammetric surveys (Vincent et al., 2010; Janke, 2013) or dedicated field campaigns with terrestrial laser scanners (TLS) (Kellerer-Pirklbauer et al., 2005; Riccardi et al., 2010) . Due to significant advances in technology, such as the progress of Structure-from-Motion (SfM) photogrammetry and its application in fully automatic processing software, as well as enhancement of the quality of camera sensors, terrestrial photogrammetric surveys for the generation of 3D models have seen a re-emergence in recent years (Piermattei et al., 2015, 2016; Kaufmann and Seier, 2016).

(Westoby et al., 2012; Eltner et al., 2016). Even though the number of research using these platforms in mountainous regions is growing (Fugazza et al., 2015; Gindraux et al., 2017; Seier et al., 2017), their full capabilities for monitoring glaciers and especially glacier hazards has yet to be realized. The usefulness of UAV and terrestrial SfM-photogrammetry, as well as the feasibility of data fusion and volume change assessment to enhance hazard management approach in glacial areas, must be studied and analysed.

Examining the various change detection methods, they can be divided into three categories: image algebra, which is used to calculate the difference between multi-temporal images (F. Bovolo.,2007), image transformation, which transforms multi-temporal data into a new feature space to extract information (A.A. Nielsen., 2007) and categorization processing, which compares the class labels of the associated landscapes after independent classification (S. Ghosh.,2014). They may be classified into two types: pixel-based and object-based techniques (Y. Zhang.,2018). Pixel-based approaches always try to obtain a difference map following pixel-by-pixel comparison of two pictures. Change vector analysis (CVA) (L. Bruzzone., 2000), principal component analysis (PCA) (J. Deng., 2008), post-classification (S. Ghosh.,2014), and so on are examples of representative approaches.

Another family of 3D change detection techniques directly rely on raw PCs. For a quicker computation, Girardeau-Montaut et al. presented a cloud to cloud (C2C) comparison based on the Hausdorff point-to-point distance and an octree sub-division of PCs. In a more sophisticated approach for assessing mean surface change along a normal direction, Lague et al. developed a new approach. Based on local surface roughness, the surface normal and orientation are retrieved at a consistent scale. Multi scale model to model cloud comparison is the name of this approach (M3C2). This second strategy distinguishes between positive and negative changes, which the C2C approach does not, and it does so with less computation cost. Pre-classification approaches, in contrast to post-classification methods, reveal changes before characterizing them (Xu, H., 2015). First they create an octree from one of the two PCs, and then directly extract changes in the other PC by finding missing leaf nodes. To eliminate noise and distinguish the different changes, changed points were clustered. Finally, the remaining clusters were categorized using predetermined criteria such as area, height, and roughness (Iris de Gélis., 2021).

4.2 Materials and Methods

The 3D models created in the previous stage are utilized in this chapter to calculate the variation in glacier thickness. The comparison will focus on the Miage, Brenva, Freney, and Brouillard glaciers and will cover the years 1967 to 2006. CloudCompare (www.danielgm.net/cc/) is a software for performing quantitative comparisons and analyses. It is a free and open-source application for comparing and analysing 3D point clouds and triangular meshes. It first appeared in 2003, and it has since evolved into a full 3D data processing program, containing methods for registration, noise filtering, point categorization, normal computation, and a range of other tasks. Prior to analysing cloud pairs, some pre-processing based on the quality of the 3d model in different datasets is required.

4.2.1 Noise Filtering

The first step is to eliminate all outliers and noisy points from each point cloud. The geometry of the point cloud, as well as the relative location and distance of each point, may be used to automatically delete certain points. One approach to generate a clean point cloud with a homogenous surface density,

the procedure is to extract the related components using a 3D grid which is called Label Connected Component. The octree structure is used to generate this grid. One may determine how short the minimum distance between two components is, by selecting on the octree level. The greater the level, the smaller the disparity i.e., the more components you might get. It is feasible to determine minimum point for each component. The smallest components will be omitted if they have fewer than the set number of points, which is effective for removing the smallest group of points. This tool divides the chosen cloud(s) into smaller sections separated by a set distance. Each component is a linked component (i. e., a group of 'connected' points).

Another technique is S.O.R Filter/ Noise Filter. These methods are fairly similar in that they both eliminate points that are over a specific distance from the plane fitting a particular number of neighbours for each point (kNN). The distinction is that the S.O.R. (Statistical Outlier Removal) filter uses a fixed number of neighbours that the user specifies and removes points based on a relative error: the maximum distance is equal to the average distance plus the standard deviation multiplied by a factor (nSigma) that the user specifies. Alternatively, the noise filter allows the user to provide a constant radius that determines the number of neighbours and the maximum distance from the fitting plane.

4.2.2 Registration

Because the data sets had residual, non-homogenous geo-referencing errors, a fine registration of each individual sample position was necessary, which was done in CloudCompare using the ICP (iterative closest point) technique (Pomerleau et al., 2013). ICP iteratively aligns a source point cloud with a reference point cloud in Euclidean space by minimizing a distance metric in a point-to-point method and calculating the appropriate rotation and translation to align the source point cloud with the reference. As all dataset are georeferenced in previous steps, there are acceptable pre-alignment of point clouds when they are imported to CloudCompare. A visual evaluation of the point clouds is carried out to ensure that the automated projection of the points into the software environment is of high quality.

Due to the vastness of the area of interest, two different approaches to co-registration were examined. The initial strategy used in this study was the co-registration of cloud pairs with the entire area of interest. To accomplish this, the many expected stable areas of the region were segmented, and the transformation matrix of their registration results using the ICP approach was exported and applied to the remaining parts of the region as well. The second approach, on the other hand, was to simply divide the regions of interest (e.g., glaciers) to individual point clouds in order to have a smaller area for registration in each cloud pair, and then apply the ICP method. It should be highlighted that some stable aeras should also be retained in order to test the adequate quality of cloud pair registration. The comparison of data in both methods shows that separating areas to individual point clouds yields to greater co-registration and shorter distances between points in steady sections.

Stationary regions in the model are investigated, and distance between the clouds is identified, to assess the quality of the registration and calculate the value of error in each set of point clouds. As a result, the inaccuracy for each model's registration quality would be represented by the values of the mean distance between the points.

4.2.3 Point Clouds Comparison

The comparison of two entities, such as two point clouds or one point cloud and a mesh, is the most typical use in CloudCompare. To do such operation, different algorithm can be used.

One of the usable algorithms is Cloud to Cloud comparison. It is a method based on detecting the closest point using a Hausdorff algorithm that identifies the nearest neighbour distance or calculates the distance using a local model of the reference point cloud defined by the least-square best fitting plane that passes through the nearest point and its neighbour. This approach does not enable you to discriminate between negative and positive variations, but it is the simplest and fastest way to compare two point clouds. The density of the point clouds and the overlapping of the models have an impact on the ultimate precision of the distance calculation.

Cloud to Mesh (C2M) comparison method is another alternative approach. This approach is similar to the last one in theory, but it uses a triangular mesh as a reference model. A mesh-to-mesh comparison may also be done, in which case the compared model is regarded as a point cloud based on the triangles' vertices. The quality of the mesh, which is difficult to generate for point clouds with substantial roughness or missing data owing to obstruction, as in this work, has a major influence on the efficacy of the distance calculation.

Lague et al. presented Multi-scale Model to Model Cloud Comparison (M3C2) approach, and CloudCompare has implemented the algorithm. There are two basic phases to the technique. First, surface normal calculation and orientation in a three-dimensional space, according to a user-defined scale and commensurate with local surface roughness. Then, it is feasible to identify both positive and negative values using mean distance calculation between point clouds in the normal direction with explicit computation of local confidence interval. The developers of this method proved that it can support complicated three - dimensional geometries with flat and vertical edges in the same scene and reducing the uncertainty caused by the model's local roughness. The M3C2 was developed to calculate the 3-D distance between two point clouds in the normal surface direction and present a 95% confidence interval based on point cloud roughness and co-registration uncertainty. As a result, the approach is well-suited to assessing statistically significant ice cliff evolution where the geometry varies in three dimensions, and it is resistant to changes in point density and point cloud noise (Barnhart and Crosby, 2013; Lague and others, 2013). In investigations of Nourbakhshbeidokhti et al. 2019 concerning these methods for estimating geomorphologic variations in channel sedimentation, M3C2 emerged as the most reliable method for highlighting erosion and deposition rates from point cloud comparisons, due to the fact that this procedure does not use interpolation, which might cause errors, particularly for complex landform.

Therefore, M3C2 is considered as main method for comparison of datasets. At following the result of comparison of dataset in sequence years are illustrated.

4.2.4 Volume calculation

For the evaluation of volume change through the years, CloudCompare use calculation of the volume between two 2.5D clouds or between a 2.5D cloud and an arbitrary plane with constant height. It is based on a cloud rasterization/gridding method. If merely considering volume calculations, the CloudCompare is totally sufficient and offers results equal to those computed by the top commercial solutions among the evaluated software solutions built for diverse purposes. The method of computing the convex envelope, which might possibly skew the findings, is the only warning when using this program (Martin Štroner., 2019). The resolution of the raster grid used to estimate the volume is determined by the step value. The larger the number, the less accurate the outcome. As a result, the lowest feasible step should be the goal. The density of the clouds, though, will restrict the outcome. The percentage of average neighbours in each cell should be considered. It should be kept close to 8, or gaps would emerge between the cells, resulting in an incorrect volume estimation.

The percentage of cells that have a matching cell in the other grid is the number of cells that have a matching cell in the other grid. It simply shows how completely the two clouds overlap, though. Step size of generated grid should be optimized to make Average neighbour per cell as close as possible to 8. In all the comparison cases, the step value is optimized between 3 and 5 to obtain value 7.9 for the Average neighbour per cell. Due to importance of height difference in these comparisons, the projection direction for the volume calculation is considered to be Z direction and height of each cell is considered to be average of the points inside the cell.

4.3 Results and Analysis

In the case of volume variability and variations in point height within glaciers over time, 3D models are compared. Because GCPs contain the same coordinates, they aid in improved co-registration by causing models to overlap on each other. To ensure the quality and reliability of co-registration, some possibly stable locations are segmented in 5 sample windows to detect registration error in all comparisons. Then, based on the registration accuracy, the significant changes, either positive or negative, are distinguished for a better understanding of glacier dynamics. The volume variation and height variations will be examined, and the results will be used to determine each glacier's hazard potential based on regional mean temperature.

4.3.1 Miage Glacier

This glacier is located at east side of the valley and has many branches at its upper part (see chapter 2). In this part of study, evaluation is done on change of glacier thickness on approximately 3 km^2 of glacier surface except the cases that have contribution of data from 1967 that missed the middle parts of Miage due to the problems discussed in chapter 3. The accuracy of the co-registration is in the range of 0.5 to 1.5 meters (table 4.1). Also, root means square error of distances vary from 2 to 4 meters. As a result, the maximum average height reduction occurred between 2001 and 2006 with 3.5 meters of decrease and the variation is minimum for 2000 to 2001. Similarly, the largest volume changes mostly occurred from 2001 to 2006. In contrast, the only major increase of glacier thickness occurred in 8 years from 1979 to 1988; after 1988 the glacier started losing mass. Distribution of height variation of point clouds (figure) represent mostly mass loss condition in Miage glacier through the decades and last 5 years of data had the most contribution to that. The comparison between 2001 and 2006 shows that glacial mass loss occurred largely in the lower regions of the Miage, whereas in 2000-01, the losses happened in the middle part, while the lower part remained roughly intact. From 1996 to 2000, the volume and height decreased primarily in the lower half of the glacier body, with some gain seen in the top half. In contrast, in the lower section of Miage glacier mass increased from 1967 to 1988.

Time Period	Number of points in sample windows	Mean of M3C2 distances [m]	Standard deviation of M3C2 distances [m]	RMSE of M3C2 distances [m]
2001-06	114k	1.310	1.613	2.818
2000-01	74k	0.900	2.609	2.696
1996-2000	158k	1.616	2.945	3.203
1988-96	218k	0.674	2.260	2.267
1979-88	230k	1.955	4.671	4.952
1967-79	128k	0.670	3.267	3.531

Table 4.1. Error of the co-registration in sample windows of stable parts around Miage Glacier.

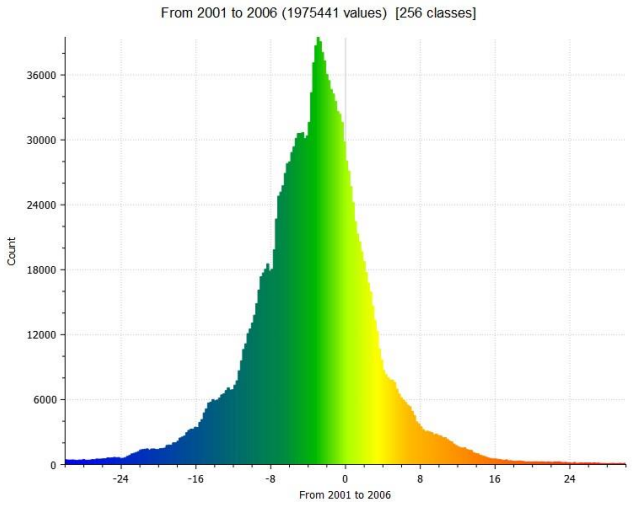
From 2001 to 2006 (1975441 values) [256 classes]
Count
From 2001 to 2006

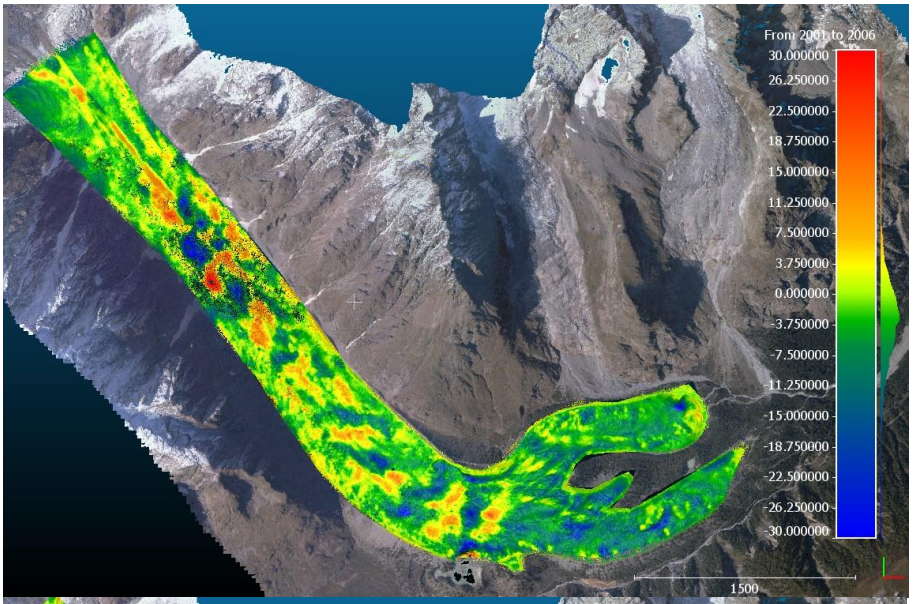
From 2001 to 2006
30.000000
26.250000
22.500000
18.750000
15.000000
11.250000
7.500000
3.750000
0.000000
-3.750000
-7.500000
-11.250000
-15.000000
-18.750000
-22.500000
-26.250000
-30.000000
1500

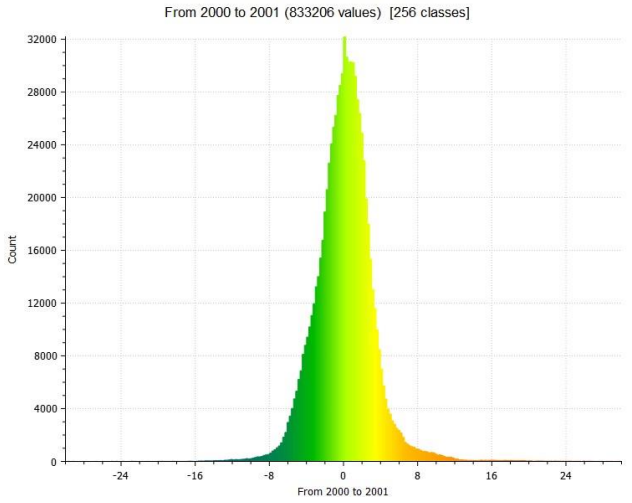
From 2000 to 2001 (833206 values) [256 classes]
Count
From 2000 to 2001

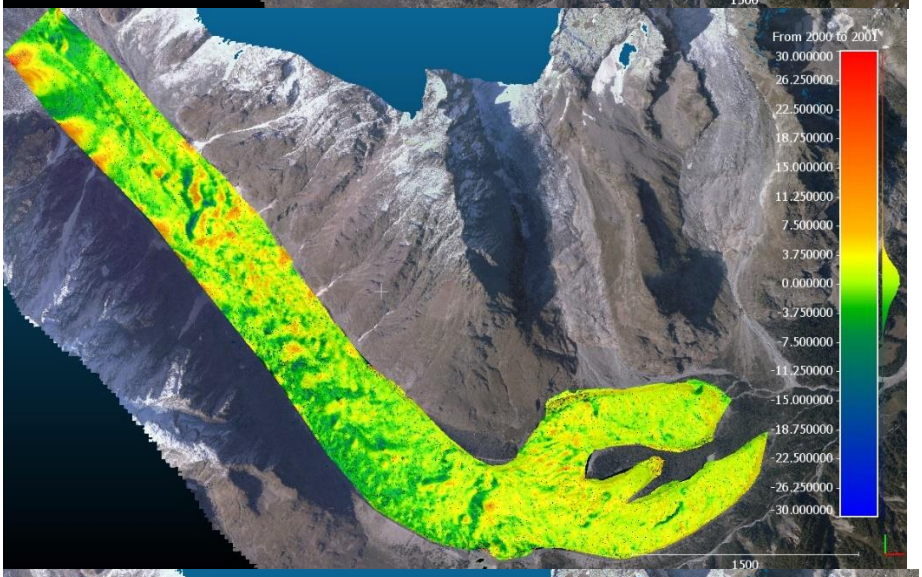
From 2000 to 2001
30.000000
26.250000
22.500000
18.750000
15.000000
11.250000
7.500000
3.750000
0.000000
-3.750000
-7.500000
-11.250000
-15.000000
-18.750000
-22.500000
-26.250000
-30.000000
1500

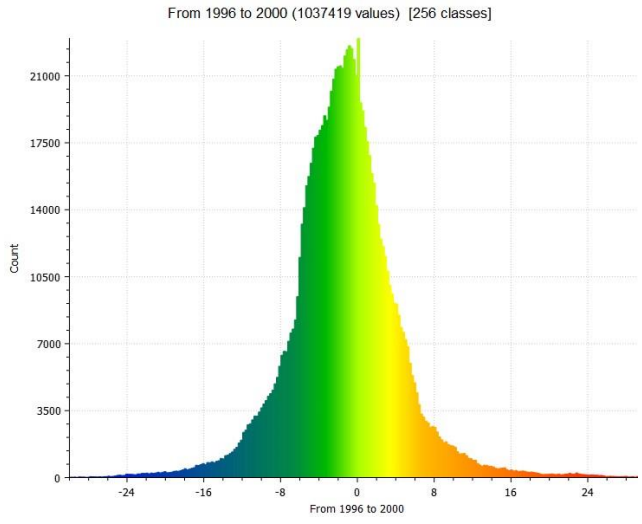
From 1996 to 2000 (1037419 values) [256 classes]
Count
From 1996 to 2000

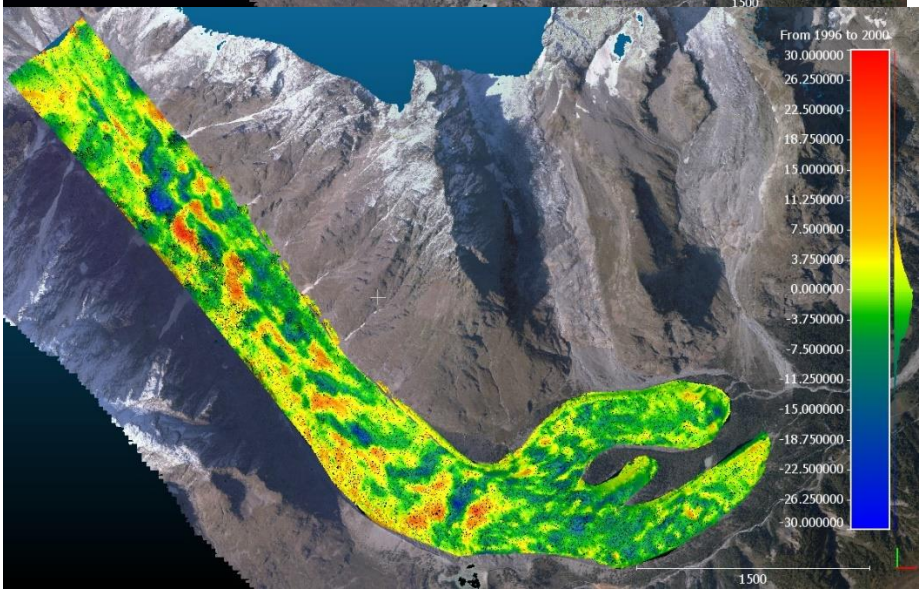
From 1996 to 2000
30.000000
26.250000
22.500000
18.750000
15.000000
11.250000
7.500000
3.750000
0.000000
-3.750000
-7.500000
-11.250000
-15.000000
-18.750000
-22.500000
-26.250000
-30.000000
1500

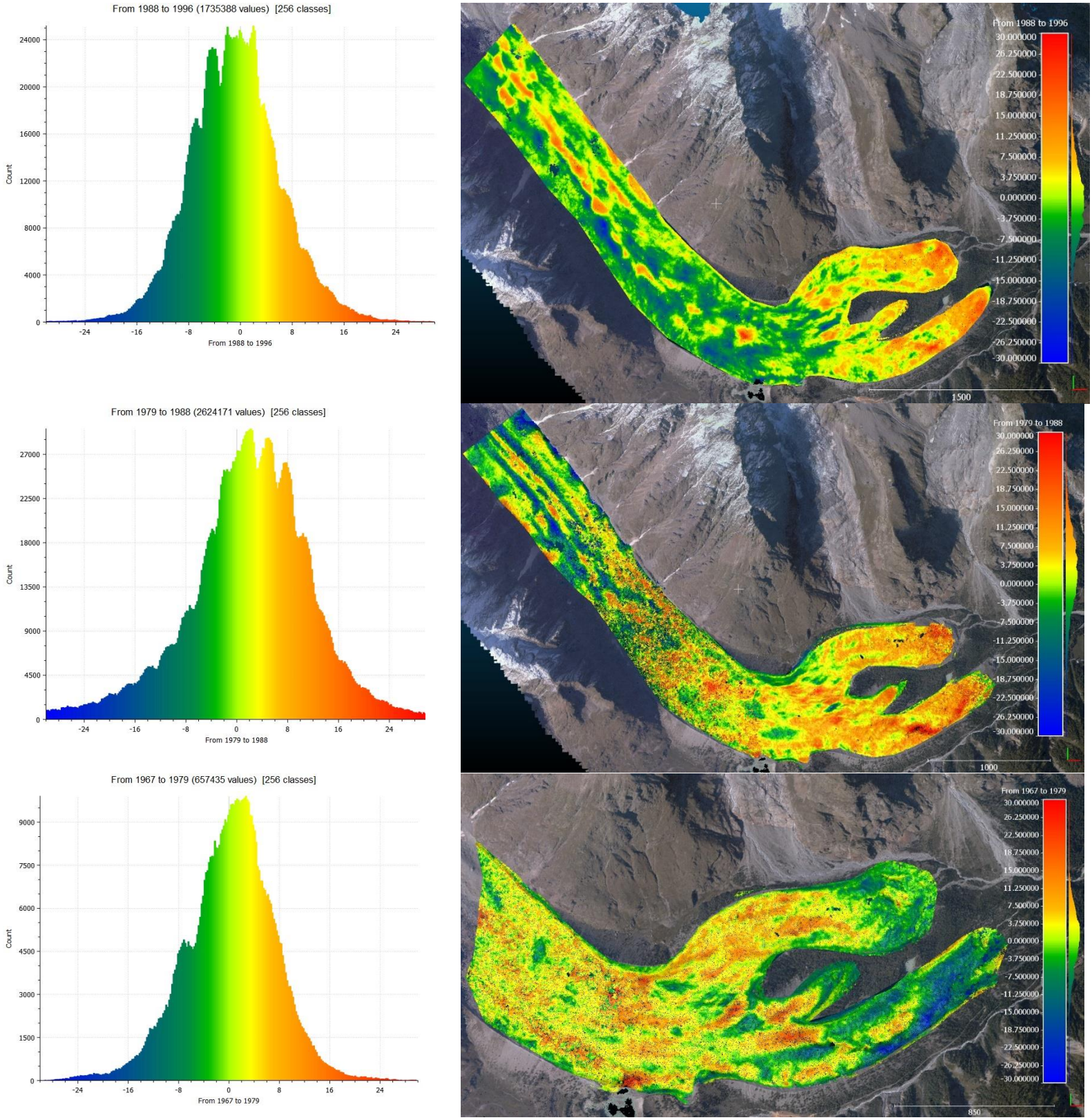

Figure 4.1. Miage Glacier evolution from year 1967 to 2006

Time Period	Mean of M3C2 distances [m]	Standard deviation of M3C2 distances [m]
2001-06	-3.560	4.242
2000-01	0.139	3.218
1996-2000	-1.334	3.942
1988-96	-0.765	5.439
1979-88	1.864	5.836
1967-79	0.225	5.065

Table 4.2. The mean height changes through the years 1967 to 2006 in Maige Glacier

Time period	Volume [m^3]	Removed Volume [m^3]	Added Volume[m^3]	Matching Cells [%]	Non-Matching Cells- ground [%]	Non-Matching Cells – Ceil [%]
1967 to 1979	2,290,250.656	(-)4,570,768.600	(+)6,861,019.257	98.3	0.8	0.9
1979 to 1988	6,332,732.431	(-)7,701,964.294	(+)14,034,696.725	98.1	0.7	1.2
1988 to 1996	-2,022,644.283	(-)9,585,398.447	(+)7,562,754.164	98.5	0.7	0.9
1996 to 2000	-5,776,350.227	(-)10,850,891.828	(+)5,074,541.602	98.9	0.9	0.3
2000 to 2001	422,118.866	(-)4,216,995.114	(+)4,639,113.980	99	0.3	0.6
2001 to 2006	-12,845,033.982	(-) 16,682,452.378	(+)3,837,418.396	98.8	0.8	0.4
Total	-11,598,926.54	(-) 53,608,470.7	42,009,544.1			

Table 4.3. The volume variation of Miage glacier from 1967 to 2006.

4.3.2 Upper branches of Miage Glacier

The Miage glacier continues up the mountainside to the north. The three Miage branches are located to the north of the valley, and their differences are assessed in this part of the study. The east side of the valley has two glacier branches measuring 0.260 and 0.379 km^2, while the west side has one measuring 0.348 km^2. The highest regions of these glaciers were deleted before the comparison process in certain reconstructions because they were not dense enough to be used for the analysis. Also, in the 1967 data reconstruction, shadows obscure the area at the higher parts of Miage (see chapter 3), causing the middle part at the north and west glaciers to be missed. The average accuracy of co-registration is 1-2 meters across all cloud pairs. A comparison of the years 2001-06 reveals a significant drop in volume and height in the west glacier up to -16 meters. In addition, glaciers lost around 5.7 million cubic meters during this time span. There have been no major variations in height in these three glaciers throughout the previous years.

Figure 4.2. the area of the comparison analysis at the upper part of Miage Glacier.

Time Period	Number of points in sample windows	Mean of M3C2 distances [m]	Standard deviation of M3C2 distances [m]	RMSE of M3C2 distances [m]
2001-06	187k	1.461	0.957	1.747
2000-01	196k	-1.318	3.128	3.395
1996-2000	210k	1.558	1.670	1.761
1988-96	147k	-2.125	1.872	2.832
1979-88	298k	1.971	4.189	4.630
1967-79	136k	-1.014	4.036	4.161

Table 4.4. Error of the co-registration in sample windows of stable parts around Upper part of Miage Glacier.

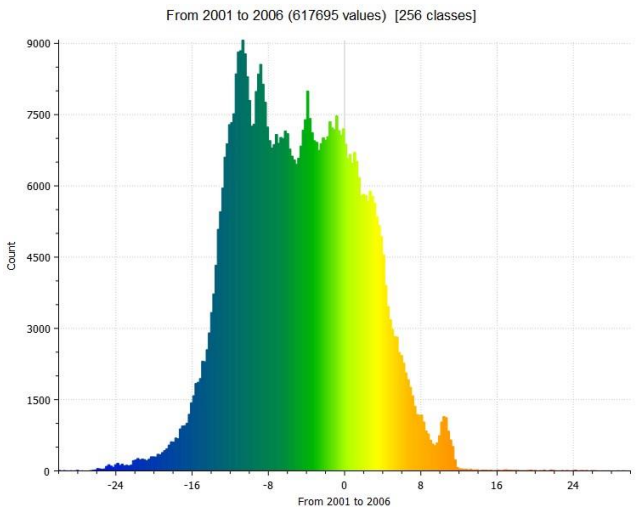
From 2001 to 2006 (617695 values) [256 classes]
Count
From 2001 to 2006

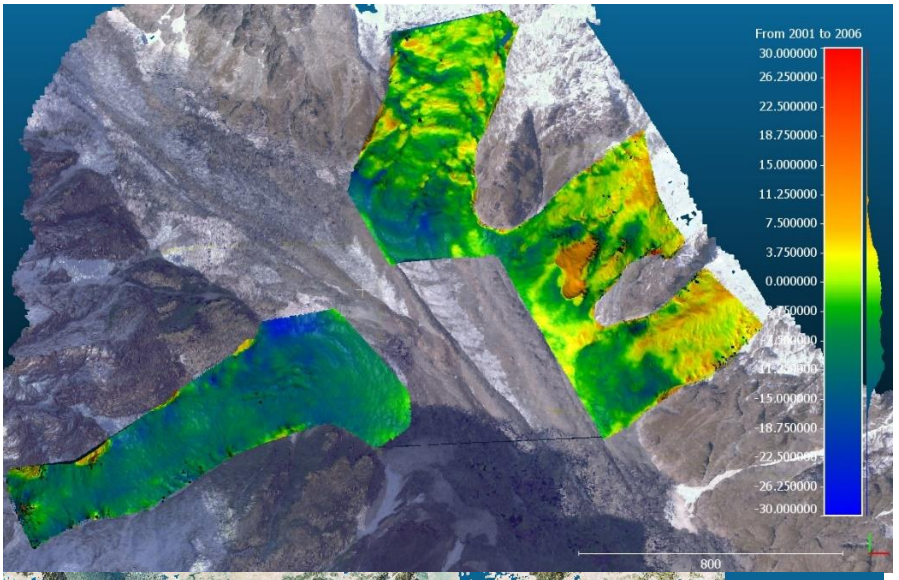
From 2001 to 2006
30.000000
26.250000
22.500000
18.750000
15.000000
11.250000
7.500000
3.750000
0.000000
-15.000000
-18.750000
-22.500000
-26.250000
-30.000000
800

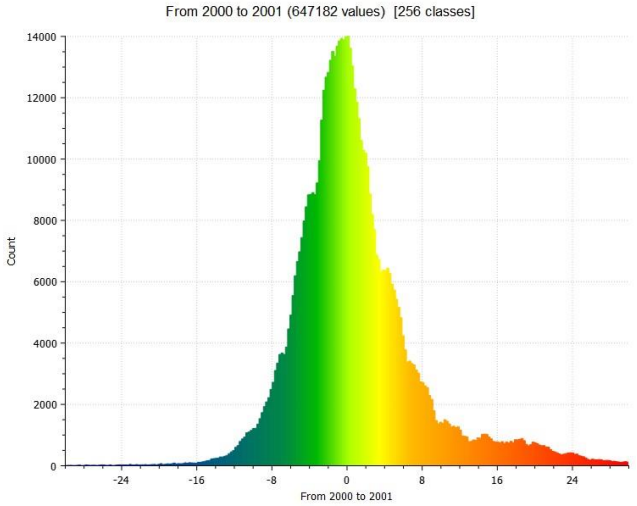
From 2000 to 2001 (647182 values) [256 classes]
Count
From 2000 to 2001

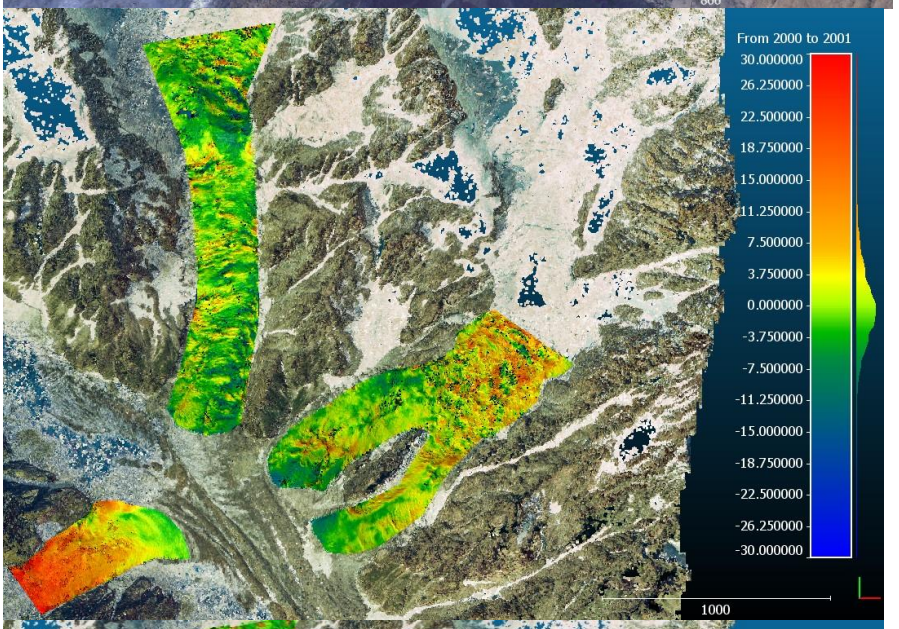
From 2000 to 2001
30.000000
26.250000
22.500000
18.750000
15.000000
11.250000
7.500000
3.750000
0.000000
-3.750000
-7.500000
-11.250000
-15.000000
-18.750000
-22.500000
-26.250000
-30.000000
1000

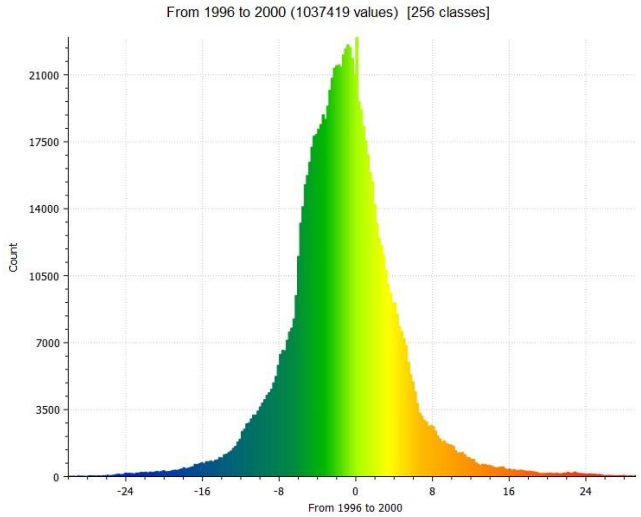
From 1996 to 2000 (1037419 values) [256 classes]
Count
From 1996 to 2000

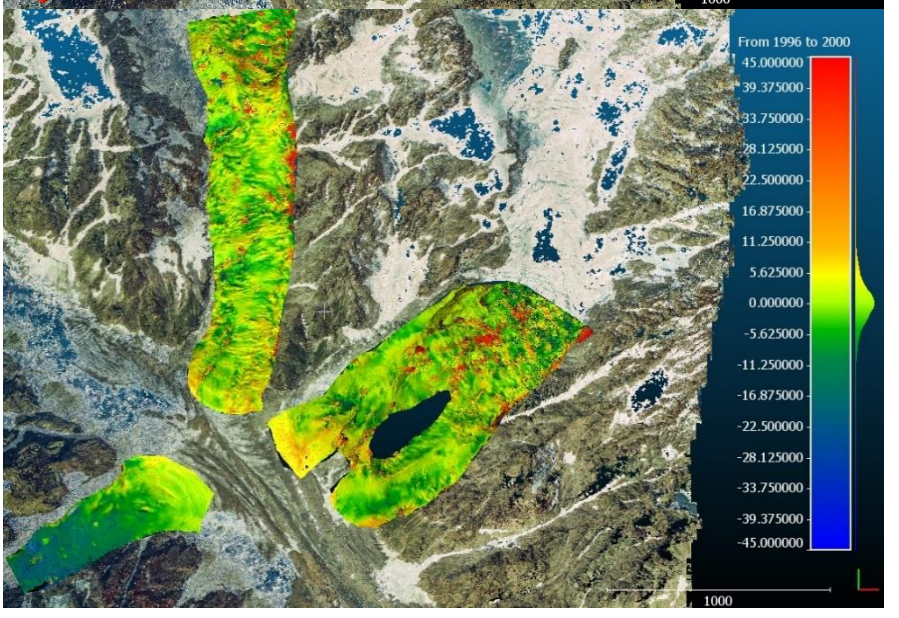
From 1996 to 2000
45.000000
39.375000
33.750000
28.125000
22.500000
16.875000
11.250000
5.625000
0.000000
-5.625000
-11.250000
-16.875000
-22.500000
-28.125000
-33.750000
-39.375000
-45.000000
1000

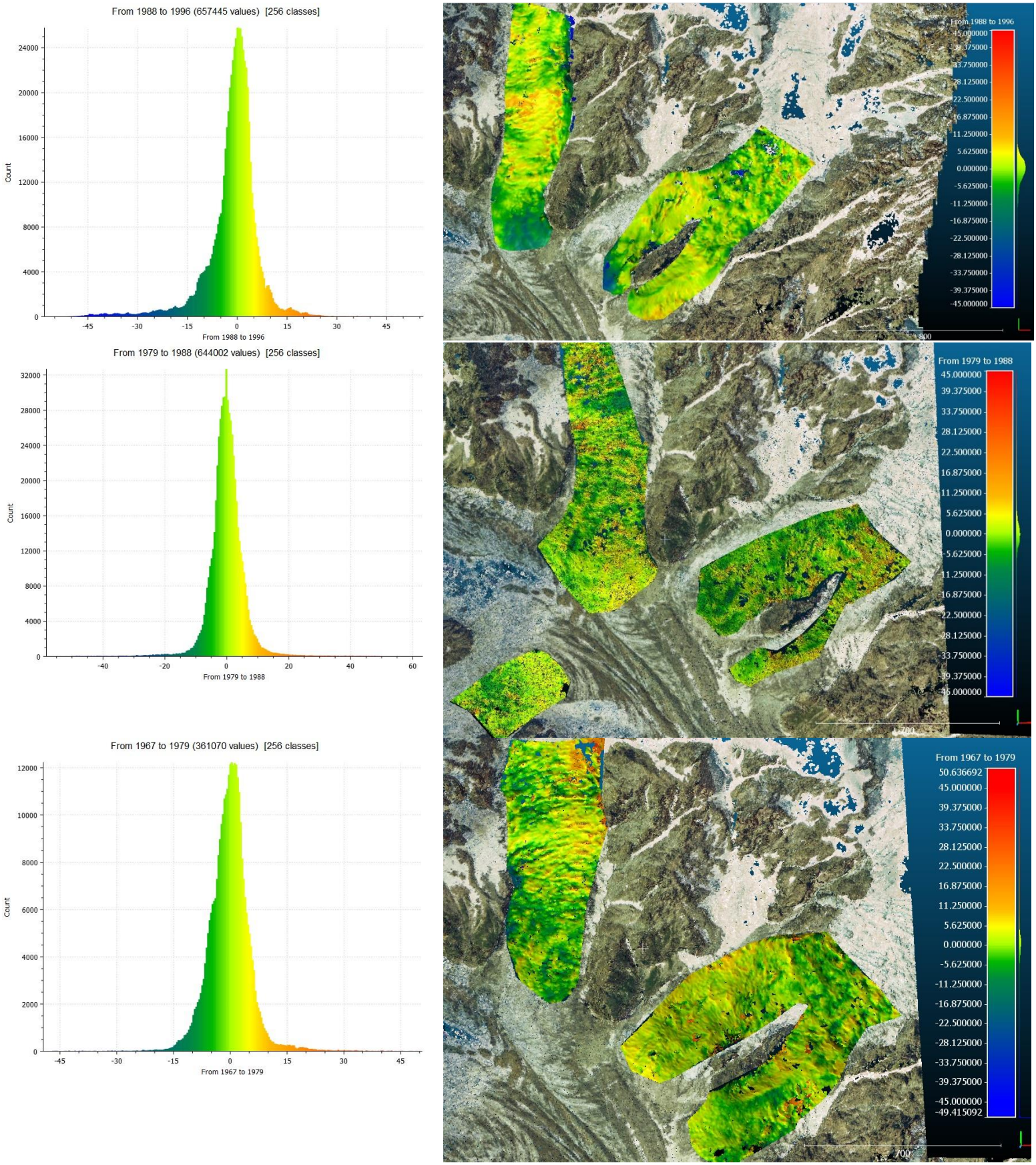

Figure 4.3. upper parts of Miage Glacier evolution from year 1967 to 2006

Time Period	Mean of M3C2 distances [m]	Standard deviation of M3C2 distances [m]
2001-06	-4.756	6.358
2000-01	1.025	7.136
1996-2000	2.831	11.248
1988-96	-1.309	7.767
1979-88	-0.249	5.614
1967-79	-0.216	5.499

Table 4.5. The mean height changes through the years 1967 to 2006 in Upper part of Miage Glacier.

Time Period	Volume [m^3]	Removed Volume [m^3]	Added Volume[m^3]	Matching Cells [%]	Non-Matching Cells- ground [%]	Non-Matching Cells – Ceil [%]
1967 to 1979	-199,647.461	(-)1,424,226.807	(+)1,224,579.346	94.1	4.8	1.1
1979 to 1988	170,703.743	(-)1,043,857.382	(+)1,214,561.125	96.5	1.5	2
1988 to 1996	-2,869,392.252	(-)4,579,239.070	(+)1,709,846.818	97.3	1.2	1.6
1996 to 2000	1,735,825.344	(-)3,978,277.963	(+)5,714,103.307	97.7	1.4	0.8
2000 to 2001	1,174,757.590	(-)2,961,095.818	(+)4,135,853.408	98.8	0.4	0.8
2001 to 2006	-5,754,268.490	(-)6,638,596.080	(+)884,327.590	99.3	0.3	0.4
Total	-5,742,021.5	(-)20,625,293.1	(+)14,883,271.6			

Table 4.6. The volume variation of upper part of Miage glacier from 1967 to 2006.

4.3.3 Brenva Glacier

The examination is carried out on the 3km^2 surface of the Brenva Glacier, with the exception of comparisons that include the contribution of a 3D model reconstruction from 1996 that lacks the upper section of the Brenva, in which case the surface of comparison is roughly 1 km^2. The typical inaccuracy in co-registration quality assessment is roughly 2.8 meters in the worst situation. In comparison to the most recent 3D model, a significant fall in elevation of 15-20 meters is apparent at the steep area of Brenva, while a slight increase of 5 – 10 meters is visible downstream. In the 3D model containing contribution of 1979, small part of the glacier tongue close to the city is missed and it shows increase of height until 1988. A little portion of the glacier tongue near the city is absent in the 3D model including contributions from 1979, and it indicates an increase in height until 1988.

Time Period	Number of points in sample windows	Mean of M3C2 distances [m]	Standard deviation of M3C2 distances [m]	RMSE of M3C2 distances [m]
2001-06	436k	0.310	3.800	3.812
2000-01	396k	1.608	4.392	4.481
1996-2000	177k	2.824	3.819	4.468
1988-96	150k	0.674	3.100	3.176
1979-88	233k	0.892	2.383	2.433
1967-79	243k	1.815	3.576	4.011

Table 4.7. Error of the co-registration in sample windows of stable parts around Brenva Glacier.

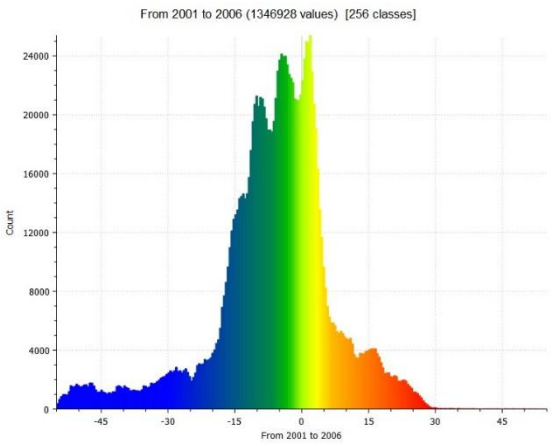
From 2001 to 2006 (1346928 values) [256 classes]
Count
From 2001 to 2006

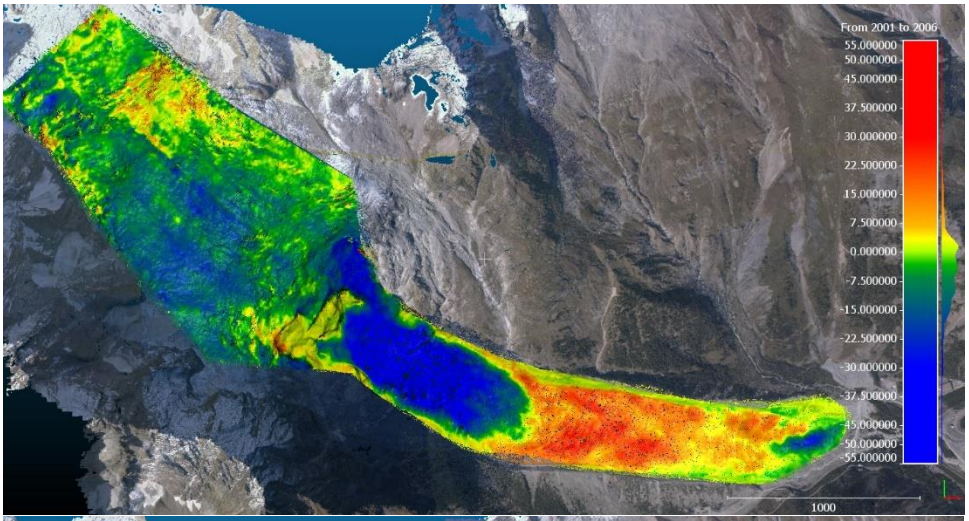
From 2001 to 2006
1000

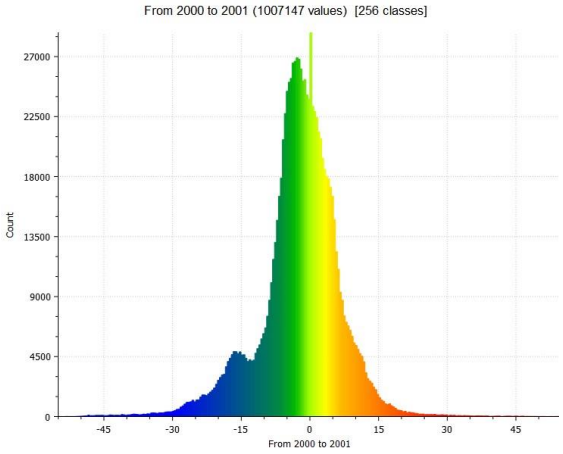
From 2000 to 2001 (1007147 values) [256 classes]
Count
From 2000 to 2001

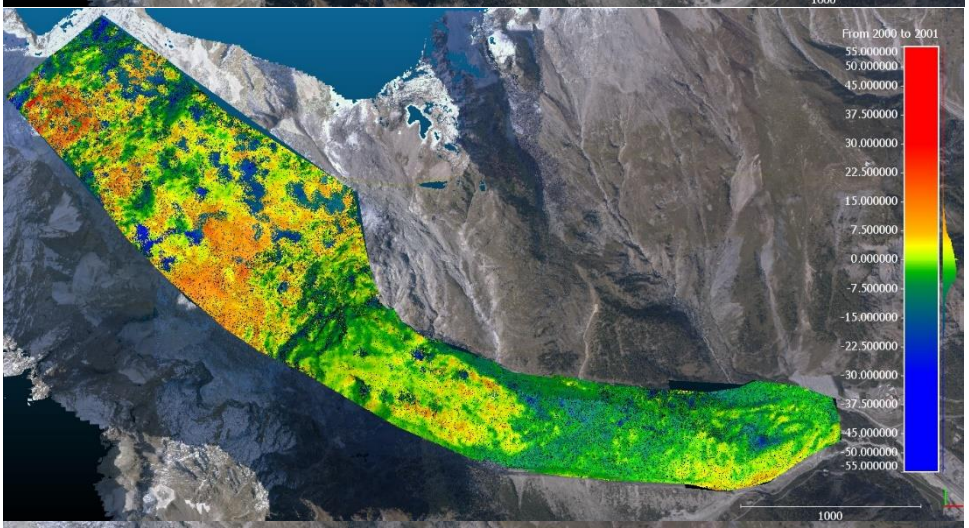
From 2000 to 2001
1000

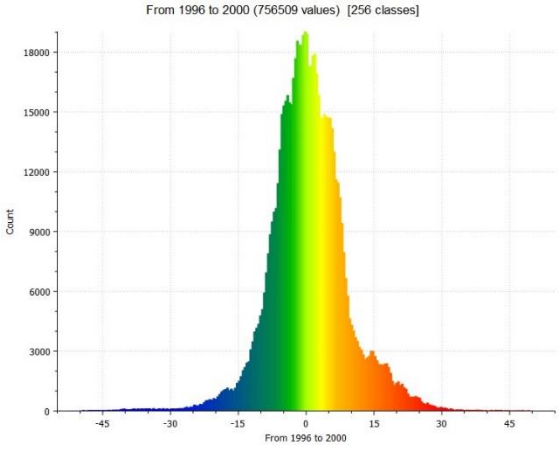
From 1996 to 2000 (756509 values) [256 classes]
Count
From 1996 to 2000

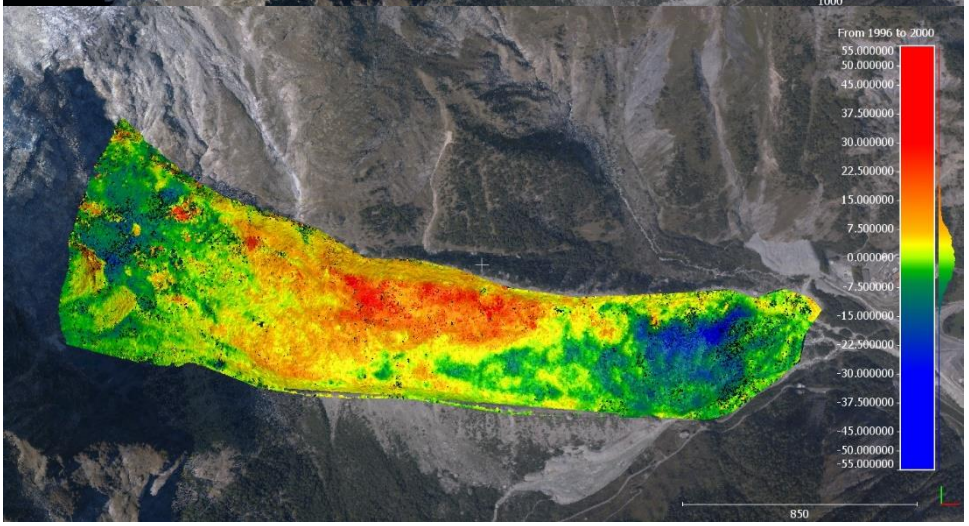
From 1996 to 2000
850

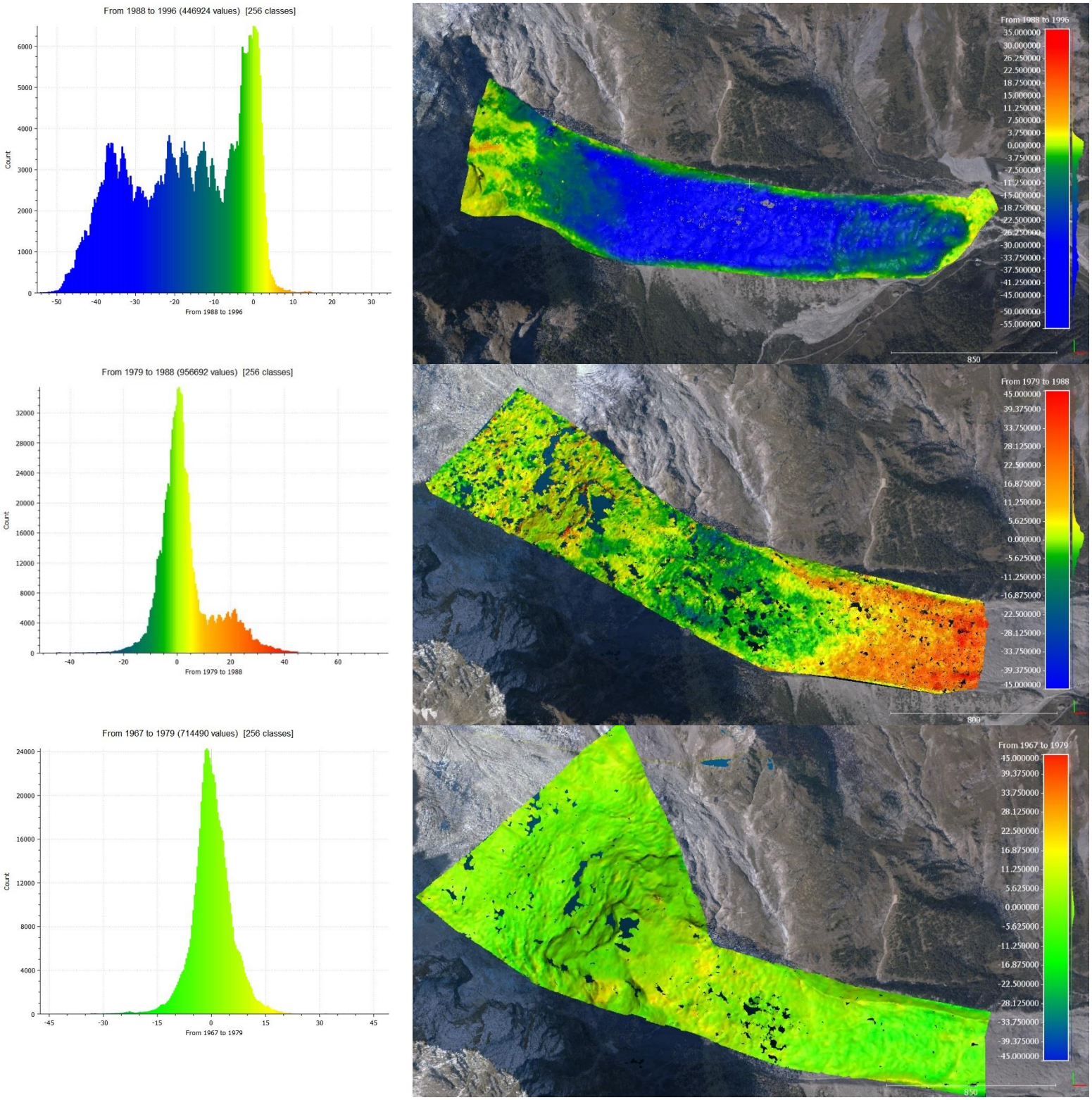

Figure 4.4. Brenva Glacier evolution from year 1967 to 2006

Time Period	Mean of M3C2 distances [m]	Standard deviation of M3C2 distances [m]
2001-06	-6.3216	13.9162
2000-01	-2.254	8.825
1996-2000	0.569	8.608
1988-96	-17.55	14.385
1979-88	3.198	10.311
1967-79	3.916	4.889

Table 4.8. The mean height changes through the years 1967 to 2006 in Brenva Glacier.

Time period	Volume [m^3]	Removed Volume [m^3]	Added Volume[m^3]	Matching Cells [%]	Non-Matching Cells- ground [%]	Non-Matching Cells – Ceil [%]
1967 to 1979	177,032.080	F	(+)4,520,968.799	97.4	1.9	0.7
1979 to 1988	4,624,761.133	(-)4,475,963.916	(+)9,100,725.049	96.4	1	2.6
1988 to 1996	-25,656,348.363	(-)25,884,575.039	(+)228,226.676	98.7	0.7	0.6
1996 to 2000	1,480,996.506	(-)3,774,890.503	(+)5,255,887.009	99.1	0.5	0.5
2000 to 2001	-3,655,358.673	(-)12,750,960.464	(+)9,095,601.791	99	0.2	0.8
2001 to 2006	-22,870,715.590	(-)32,415,178.695	(+)9,544,463.105	98.4	0.8	0.8
Total	-45,899,632.9	(-)83,645,505.3	(+)37,745,872.4			

Table 4.9. The volume variation of Brenva glacier from 1967 to 2006.

4.3.4 Freney and Brouillard Glaciers

These glaciers are located between the Miage and Brenva and has total surface 1 km^2 at the upper parts. They are located at steeper slopes than two other considered glaciers in this study.

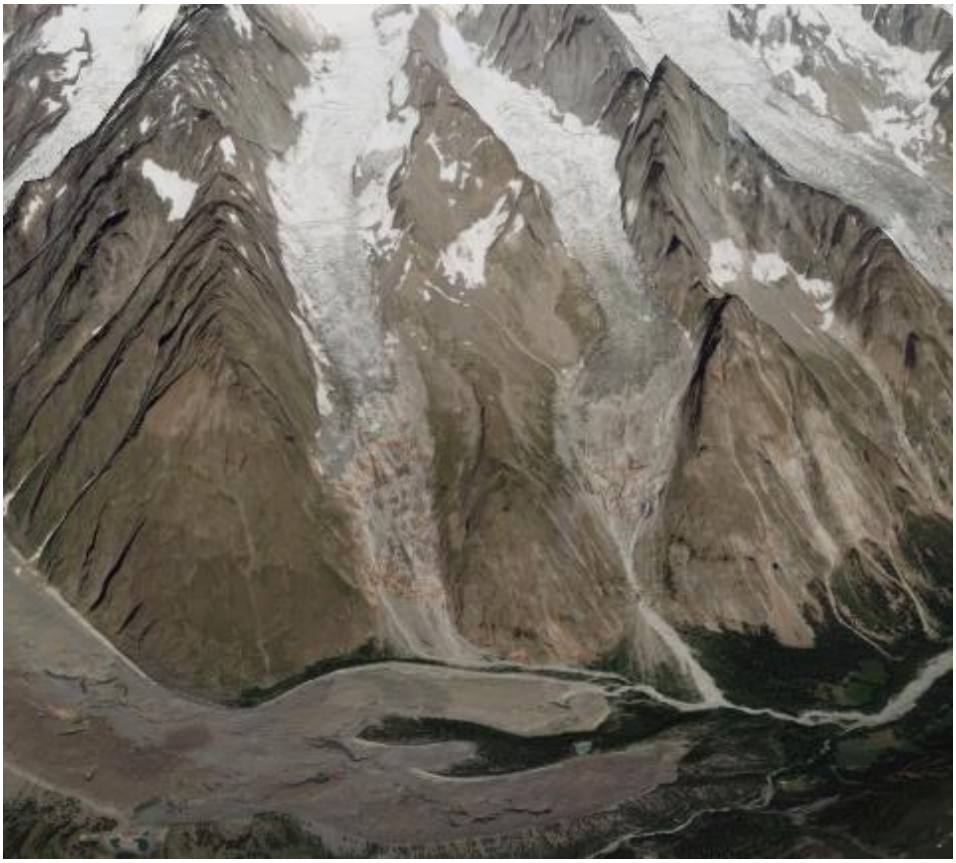

Figure 4.5. the location of Freney and Brouillard Glaciers

The evaluation of the co-registration method reveals a mean height range of 1 to 2 meters for all 3D models in anticipated steady areas. Similar to past glaciers, massive retreat occurred in the five years 2001-06. The glacier was stable in 2000-01. The upper altitudes of Freney and Brouillard show some positive height variation values in the 1996 to 2000, which is due to higher altitudes of that part and the influence of snow coverings in higher elevations. The equilibrium of height differences is shown from 1979 to 1988, but 1967 to 1979 displays largely height increase. The volume reduction is largely attributed to 2001-06, which is around 10 M cubic meters, while the highest volume rise is attributed to 1967-79, which is roughly 2 M cubic meters.

Time Period	Number of points in sample windows	Mean of M3C2 distances [m]	Standard deviation of M3C2 distances [m]	RMSE of M3C2 distances [m]
2001-06	145k	1.826	2.255	2.503
2000-01	108k	1.826	2.255	2.503
1996-2000	158k	1.143	1.817	1.966
1988-96	208k	1.002	1.203	1.203
1979-88	280k	1.279	1.630	1.804
1967-79	168k	1.104	1.489	1.854

Table 4.10. Error of the co-registration in sample windows of stable parts around Freney&Brouillard Glacier.

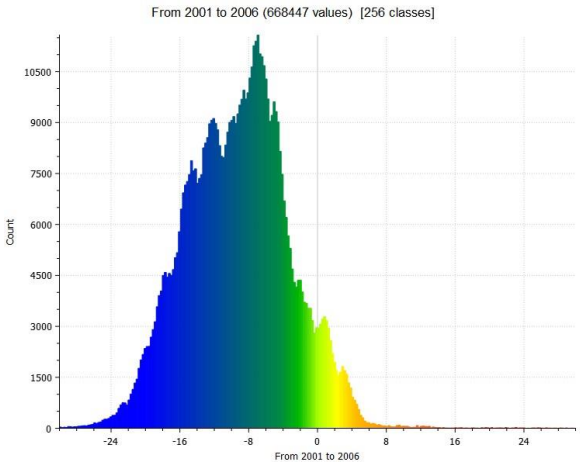
From 2001 to 2006 (668447 values) [256 classes]
Count
From 2001 to 2006

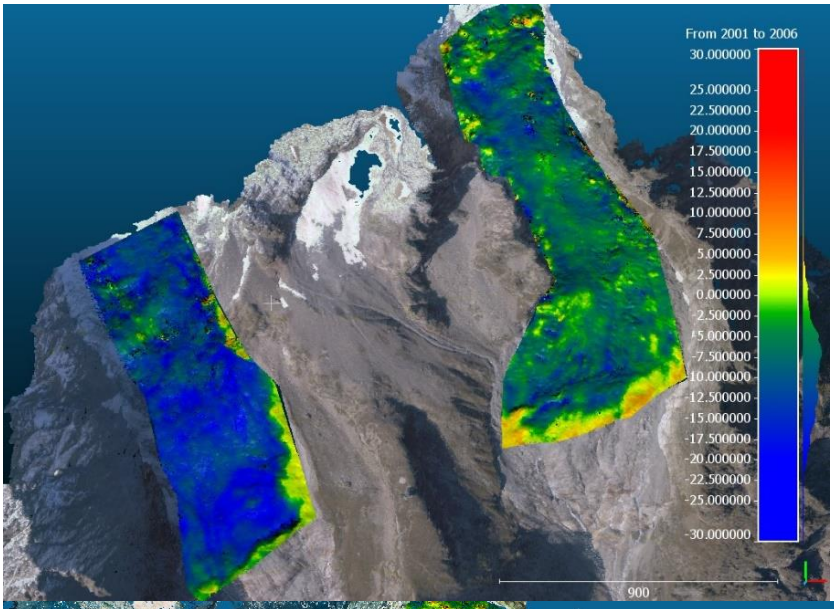
From 2001 to 2006
30.000000
25.000000
22.500000
20.000000
17.500000
15.000000
12.500000
10.000000
7.500000
5.000000
2.500000
0.000000
-2.500000
-5.000000
-7.500000
-10.000000
-12.500000
-15.000000
-17.500000
-20.000000
-22.500000
-25.000000
-30.000000
900

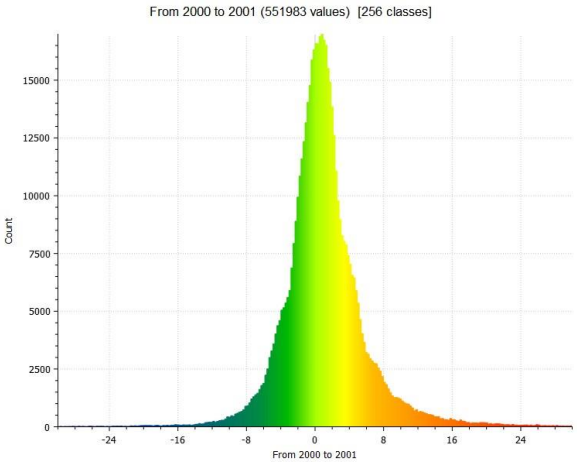
From 2000 to 2001 (551983 values) [256 classes]
Count
From 2000 to 2001

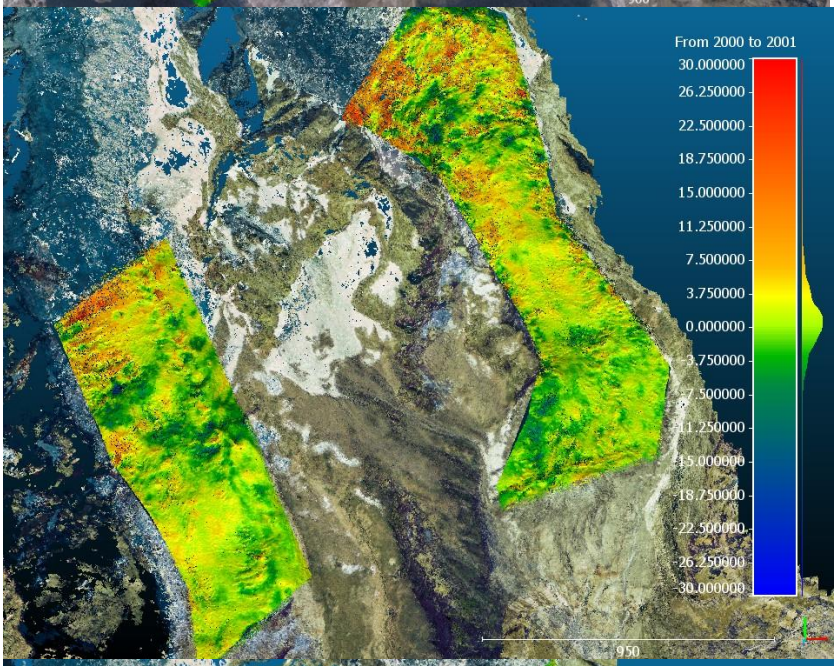
From 2000 to 2001
30.000000
26.250000
22.500000
18.750000
15.000000
11.250000
7.500000
3.750000
0.000000
-3.750000
-7.500000
-11.250000
-15.000000
-18.750000
-22.500000
-26.250000
-30.000000
950

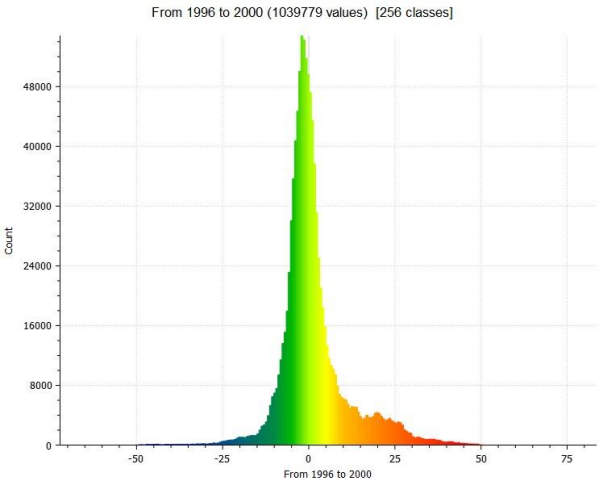
From 1996 to 2000 (1039779 values) [256 classes]
Count
From 1996 to 2000

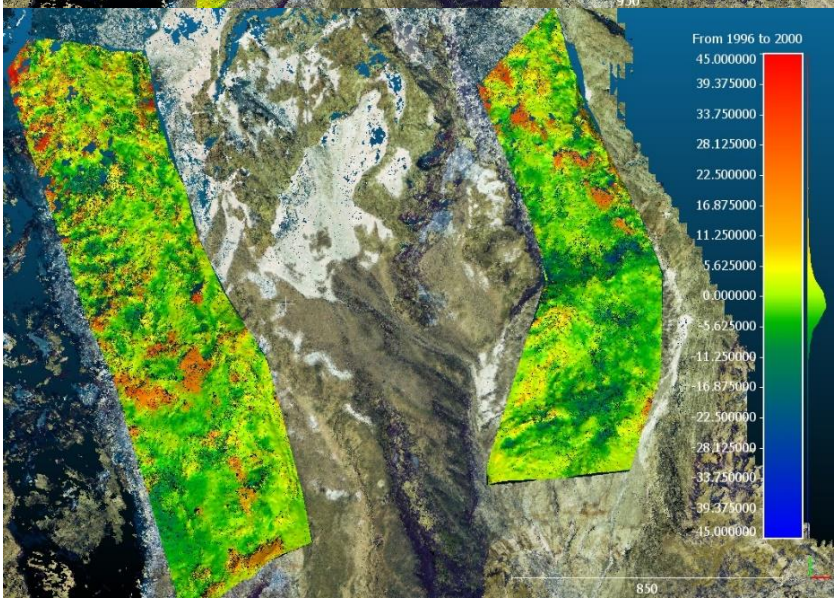
From 1996 to 2000
45.000000
39.375000
33.750000
28.125000
22.500000
16.875000
11.250000
5.625000
0.000000
-5.625000
-11.250000
-16.875000
-22.500000
-28.125000
-33.750000
-39.375000
-45.000000
850

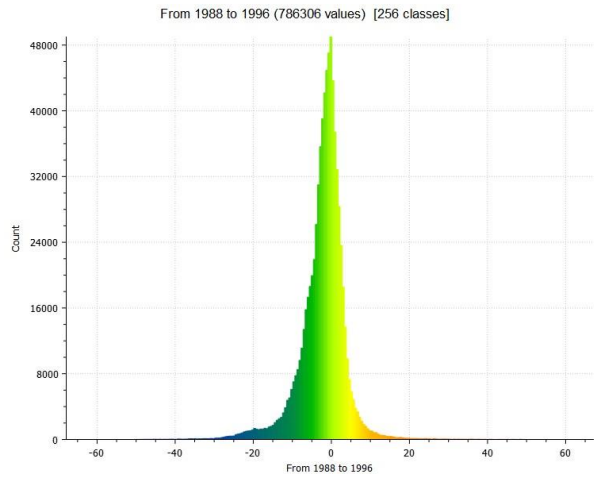

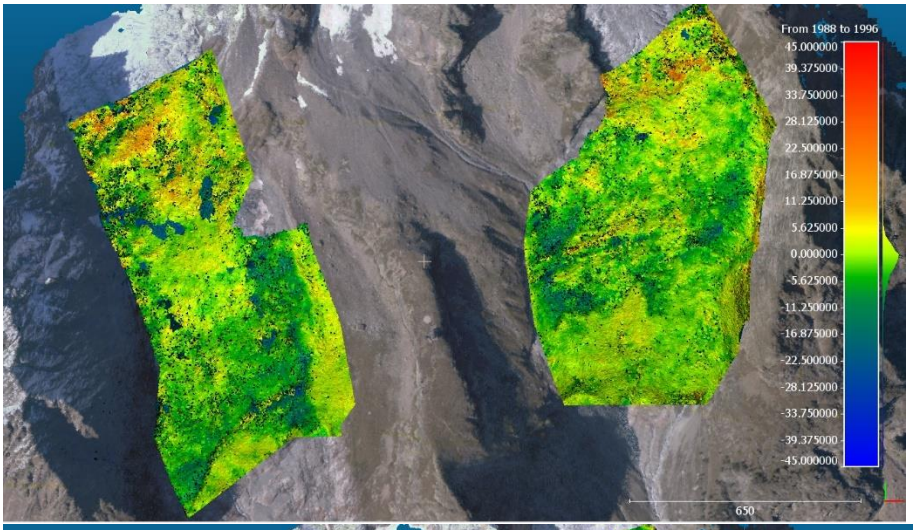

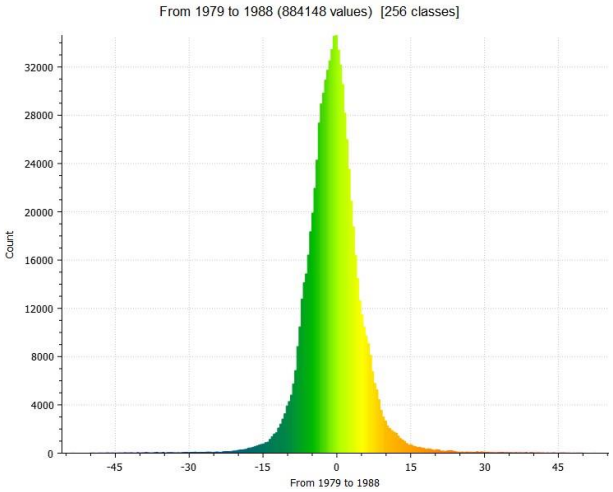

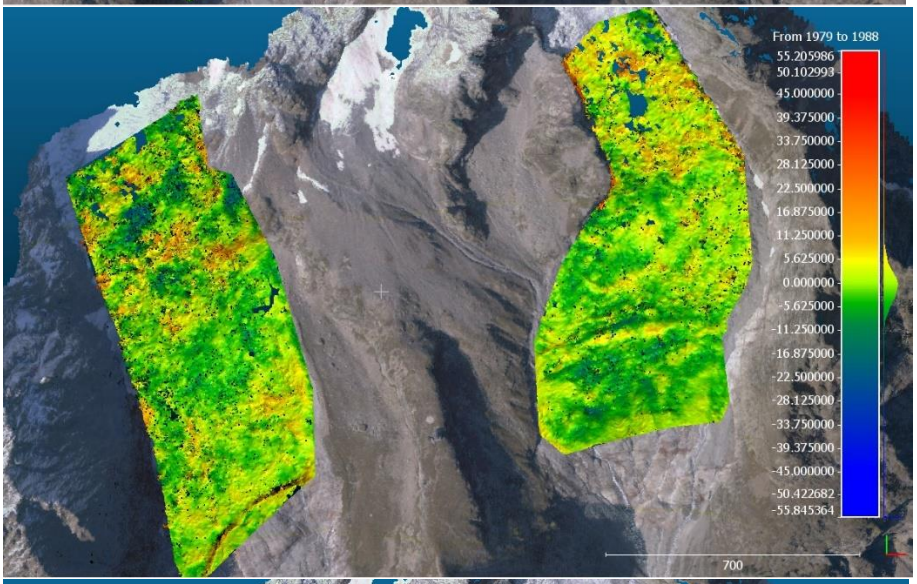

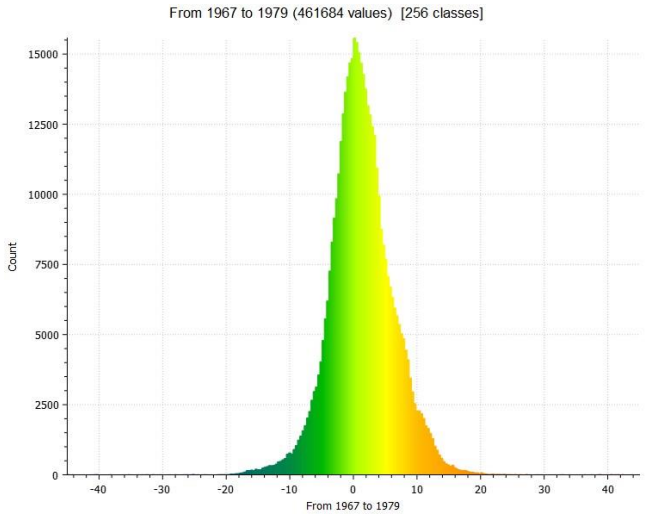

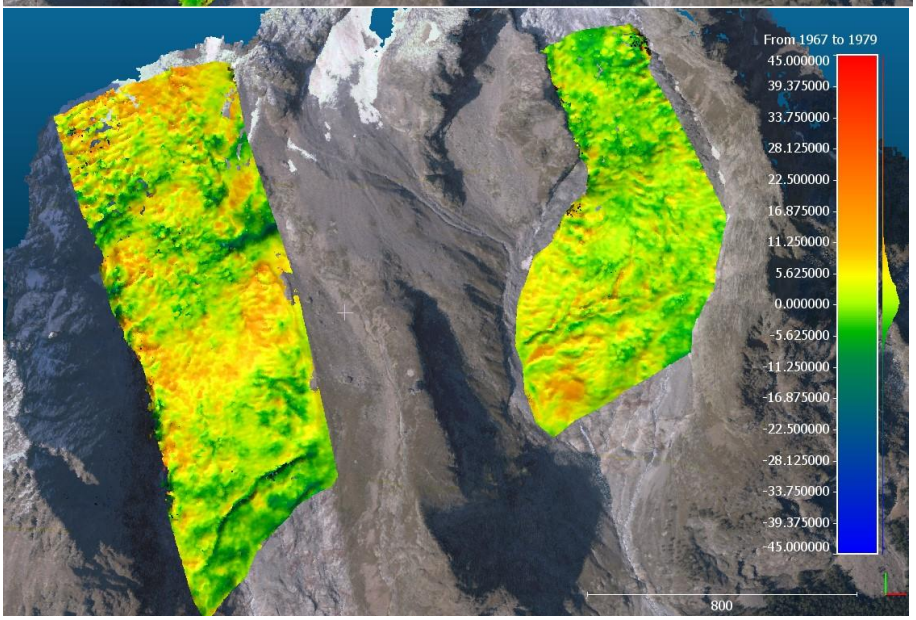

Figure 4.6. Freney and Brouillard Glacier evolution from year 1967 to 2006

Time Period	Mean of M3C2 distances [m]	Standard deviation of M3C2 distances [m]
2001-06	-9.252	4.262
2000-01	1.097	5.298
1996-2000	1.365	9.783
1988-96	-2.183	5.913
1979-88	-0.665	5.800
1967-79	1.299	4.99

Table 4.11. The mean height changes through the years 1967 to 2006 in Freney and Brouillard Glacier.

	Volume [m^3]	Removed Volume [m^3]	Added Volume[m^3]	Matching Cells [%]	Non-Matching Cells-ground [%]	Non-Matching Cells – Ceil [%]
1967 to 1979	1,957,809.808	(-)1,706,552.319	(+)3,664,362.128	97.1	2.5	0.4
1979 to 1988	-890,723.431	(-)2,475,710.022	(+)1,584,986.591	95.6	2.9	1.5
1988 to 1996	-4,047,685.681	(-)5,050,477.997	(+)1,002,792.316	98.1	0.9	1
1996 to 2000	1,204,392.261	(-)2,957,971.875	(+)4,162,364.136	98	1.2	0.8
2000 to 2001	1,354,591.235	(-)1,536,841.516	(+)2,891,432.751	97.5	1.6	0.9
2001 to 2006	-10,667,798.763	(-)10,959,808.761	(+)292,009.999	98.9	0.4	0.8
Total	-11,089,414.6	(-)24,687,362.5	(+)13,597,947.9			

Table 4.12. The volume variation of Freney and Brouillard glacier from 1967 to 2006.

4.4 Discussion

Numerous conclusions can be achieved by comparing 3D models from the perspective of glacier dynamics. This result can be coupled with meteorological factors from the same time period to validate the findings and predict future behaviour of glaciers as a consequence of global warming. Global warming and increasing temperature levels are expected to cause significant environmental changes in mountainous areas, including substantial variations in glacier size, permafrost, ice and snow cover (Rastner, P. et al., 2019).

All of the glaciers show the same pattern over time. They generally had a minor increment in mass loss until 1996, when there was a dramatic spike in the glacier height changes. Then, except for Freney and Brouillard, a modest declining tendency is apparent until 2006, but the overall trend for glacier mass change rates in Val Veny is growing. Until 1988, the height difference trends reveal that glaciers were typically at the same elevation. Then, for all glaciers, a highlighted decline is noticeable, particularly Brenva Glacier, which achieved less than -15 meters of height decrease until 1996. This is supported by the growing tendency of the retreat rate in Brenva, which has been about -3.5 m/year since 2000. The rate of melting in this glacier is then lowered to -1.5, however it still retains a declining tendency of thickness variation until 2006.

The Miage glacier, on the other hand, used to have a consistent slope with little thickness variations. It experienced a slight height growth until 1988, then a gradual decrease in thickness over time, despite not abrupt. In addition, the pace of shrinking tends to rise over time. Similarly, the thickness of the upper branches of Miage has remained consistent, with the exception of 2000, when a high retreat rate of -3 m per year was observed, resulting in a fall in height.

Both Freney and Brouillard's thickness changes were fairly constant before 2000, however a drastic drop in height to -9 meters can be detected in 2006, which is the highest among all glaciers. Furthermore, comparable to other glaciers, the retreat rate at Freney and Brouillard has grown from 0 to more than 2 m/year over the last 5 decades.

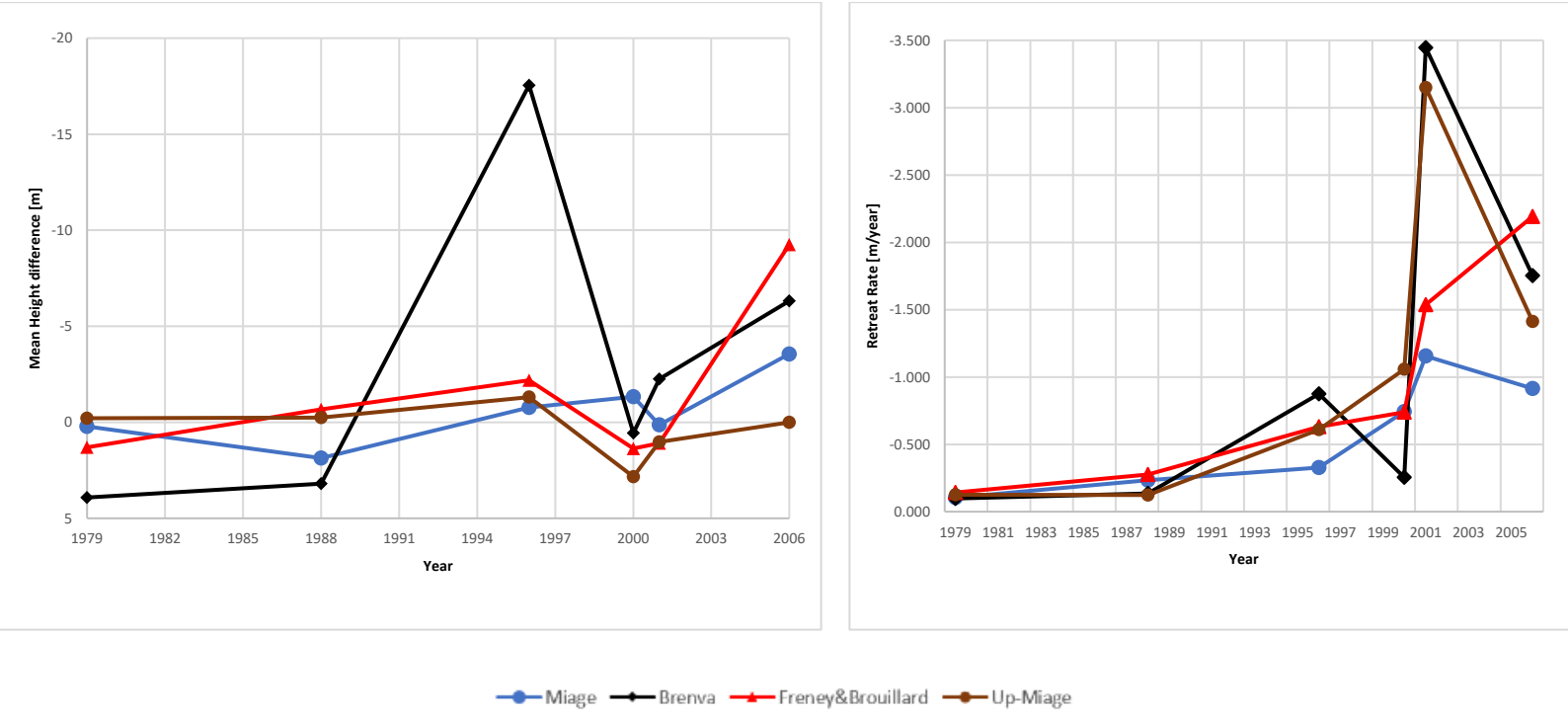

Figure 4.7. Mean height variation of glaciers in Val Veny through the years (left) and changing of retreat rate (right).

Variations in glacier thickness and retreat rate over the Val Veny reflect the impact of climate change throughout time. Meteorological data were acquired from Aosta Station (Meteostat.net) between 1979 to 2006 and it shows that the weather condition was generally regular over time in the area (Figure4.8 and Figure 4.9). From 1967 to 2006, the average lowest temperature in Val Veny was -5 to -10 °C and the average maximum temperature was 25 °C, with a very tiny growing tendency in the higher temperature in warm seasons. Temperatures rose above 30 degrees Celsius for a period of time, including 1992-93, causing an increase in the rate of retreat in all of Val Veny's glaciers as indicated in figure 4.8. In fact, when the overall temperature tendency rises to higher values, the rate of retreat in this region accelerates.

The other important component is the level of snowfall over the years, which can result in either an increase in mass or indeed a compensation for thickness loss in some cases. Snowfalls were consistent from 1979 through 1988, with average values of 30 to 50 cm. This pattern causes glacier thickness to rise in those years. Since then, there has been a decrease in both the volume and frequency of snowfalls until 1997. Thereafter, until 1999, Val Veny experienced heavy snowfalls of up to 50 cm, contributing to mass accumulation on glaciers at that time. Furthermore, until 2006, snowfalls were significantly fewer than in prior years, once this factor was coupled with rising temperatures, the retreat rate and thickness loss increased dramatically from 2001 to 2006.

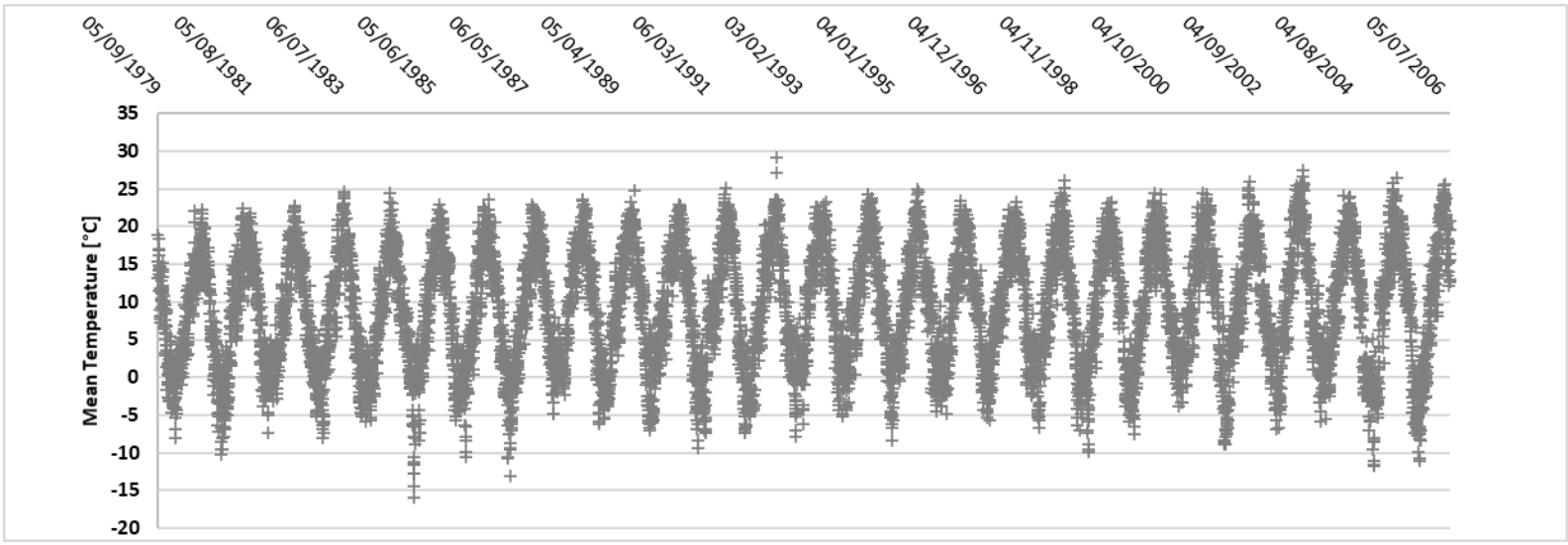

Figure 4.8. the mean temperature variation through the years 1979 to 2006 in Val Veny region (Meteostat.net).

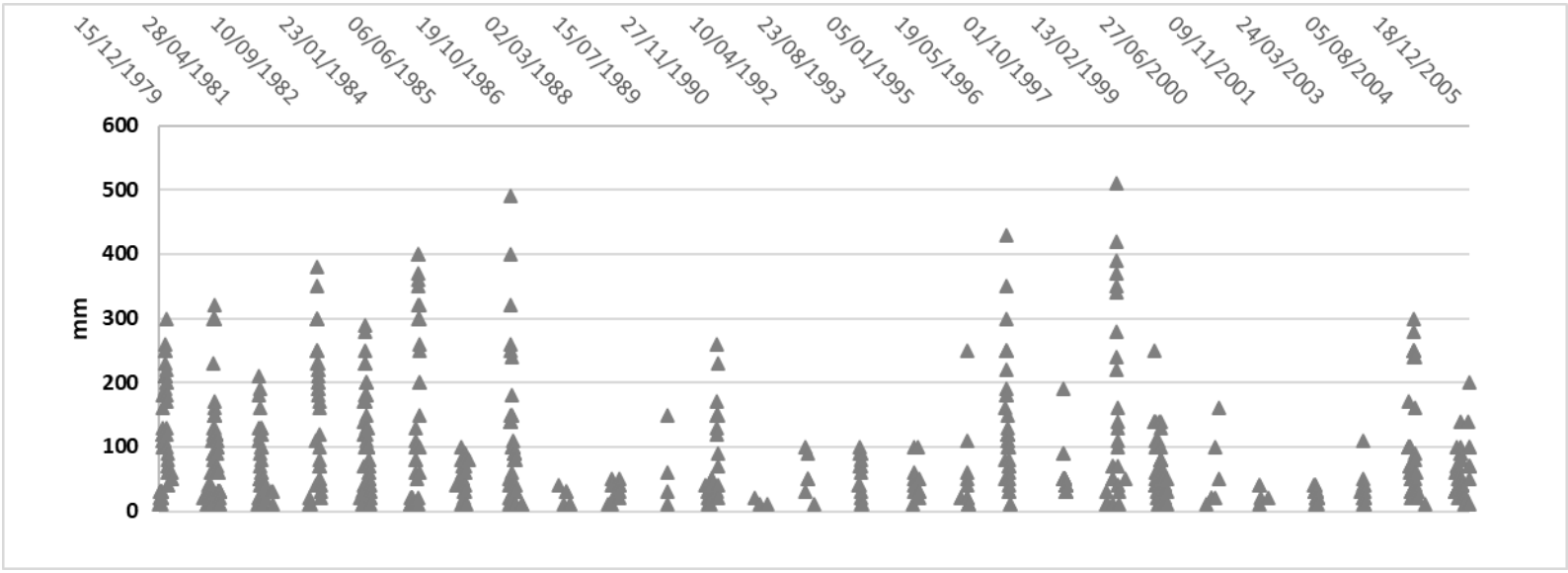

Figure 4.9. Snowfall level trends through the years 1979 to 2006 in Val Veny region (Meteostat.net).

4.5 Conclusion

The focus of this research was to compare 3D models in order to assess glacier thickness change and retreat rate over a 40-year period. To validate the findings, four glaciers in the Val Veny area were explored and their variation trends were compared to meteorological trends. The models were aligned according to GCP's thanks to georeferencing, and the quality of the cloud pair co-registration was tested by evaluating displayed distances in likely stable spots.

When a large region is surveyed, the results suggest that extracting a transformation matrix from the registration of several likely stable locations and applying it to other areas yields to more accurate registration. Additionally, each region of interest could be segmented to create smaller areas and improve the quality of the registration process. The correctness of the registration was then demonstrated by evaluating cloud pair distances in stable regions. Because it does not employ interpolation and has been endorsed by other researchers as the most accurate approach in contrast to other accessible methods, the M3C2 was regarded the best method for computing distances in cloud pairings.

Climate change, on the other hand, has confirmed our findings from cloud pair comparisons and made it feasible to track the retreat rate and volume fluctuation of glaciers by studying the local climate. Warmer-than-average months accelerate significantly the retreat of glaciers, and large snowfalls can raise the volume thickness of glaciers slightly. The discovery of a link between climate change and glacier fluctuations allows for improved monitoring of glacier-related hazards and more precise forecasting of their behaviour in various climates. More modern technologies, like as more precise GCPs or photogrammetry tools that can produce denser 3D reconstructions, can be used to better understand the link between climatic conditions and glacier thickness variations.

Chapter Five

5. Glacier-related Hazards

5.1 Introduction

Glaciers are formed by falling snow that accumulates over time to form enormous, thicker ice formations. Glaciers occur when snow freezes in one place for a lengthy period of time. The potential to flow is what distinguishes glaciers. Glaciers run like very sluggish rivers due to their tremendous bulk. Some glaciers are the size of football fields, while others can stretch for dozens, if not hundreds, of kilometers. Glaciers cover around 10% of the world's total land area, with the majority of them found in polar regions such as Antarctica, Greenland, and the Canadian Arctic. Glaciers are glacier-covered relics from the previous Ice Age, when ice covered approximately 32% of the land and 30% of the seas.

Climate change is having a significant influence on high-mountain environments, with glacier retreat being one of the most evident repercussions. The accelerated retreat of glaciers seen in the European Alps and other alpine regions throughout the world is anticipated to continue in the future (Zemp et al. 2006; Hock et al. 2019; Zekollari et al. 2019). The shrinking and loss of glacier masses has resulted in significant changes in high-mountain environments: alpine geomorphological landscapes are changing, and new landforms are emerging, bringing with them new challenges and risks (Diolaiuti and Smiraglia 2010). This necessitates the development of new methods for measuring geomorphic processes in glacial and periglacial environments (Bertotto et al. 2015). Overdeepenings and hollows, which are filled by glacial lakes when conditions are favourable, are among the recently produced landforms in recently deglaciated regions (Linsbauer et al. 2009; Buckel et al. 2018). Gradual glacier retreat is thus accompanied by a rise in the number of new glacier lakes (Paul et al. 2007; Carrivick and Tweed 2013; Mergili et al. 2013; Emmer et al. 2014; Salerno et al. 2014; Viani et al. 2016; Laute and Beylich 2021) as well as substantial geomorphological evolution including disappearance, expansion or shrinkage of existing ones (Paul e (Gardelle et al. 2011; Salerno et al. 2014, 2016; Zhang et al. 2017). Besides the emergence of new lakes, the slopes in deglaciated areas are changing owing to glacial dynamics being gradually replaced by gravitation and water-related mechanisms (i.e., paraglacial dynamics; Ballantyne 2002). These mechanisms can interact with lakes in a variety of ways, possibly resulting in a hazardous scenario (GAPHAZ 2017). Glacial Lake Outburst Floods (GLOFs), which are characterized by a rapid outflow of water from a glacial lake (Westoby et al. 2014) and subsequent severe floods with significant destructive potential and far-reaching repercussions, are among the most potentially hazardous circumstances (Worni et al. 2013; Haeberli et al. 2017; Huggel et al. 2020). The following are the most important GLOF conditioning factors: triggering mechanisms including snow or ice avalanches, rockfalls, rapid water input, etc.; reservoir hypsometry; geometry, composition, and structural integrity of the moraine dam (in the case of moraine-dammed lakes); topography and geology of the flood path (Huggel et al. 2004; GAPHAZ 2017).

The existence of a debris material on the surface of a glacier, even when the layer is only a few centimetres thick, can have a major impact on its predicted lifetime (Mihalcea, Mayer, Diolaiuti, Lambrecht, Smiraglia and Tartari, Mihalcea and others, 2006). Various processes, including as rock wall collapse and wind-blown particles inside the snow accumulation zone, can deposit debris within glaciers. The buried debris is freed by the progressive melting of the underlying ice as the glacier

progresses towards the ablation zone and adds to the surface debris layer (Stokes, Popovnin, Aleynikov, Gurney, and Shahgedanova, Stokes et al., 2007). The interaction of glacier and the atmosphere can be greatly influenced if enough debris cover is formed (e.g., by changing the surface albedo and insulation effects). Despite the significance of the debris layer to a glacier's energy balance, there are several unknowns about the underlying physical mechanisms (Collier, Nicholson, Brock, Maussion, Essery and BushCollier and others, 2014). Many of the fundamental mechanisms related to the energy flux balance have been discovered in field investigations of debris-covered glaciers, allowing melt-rate simulations to be carried out (Benn and Evans 2010). Existing models of totally covered glaciers suggest that their melt rate reduces monotonically as the thickness of the debris increases (Nicholson and Benn, 2006).

Glacier-related activities, on the other hand, can be hazardous. Furthermore, climate change may exacerbate some glacier hazards. Glacier hazards are natural Earth phenomena that affect people or property and are related to alpine glaciers, ice caps, or ice sheets.

5.2 Hazardous Mass Flows

5.2.1 Glacial Lake Outburst Floods

The term Glacial Lake Outburst Flood (GLOF) refers to the disastrous discharge of a water reservoir that has developed on, inside, beneath, or on the surface of a glacier. Dam constructions may be made mostly of glacial ice, morainic debris, or bedrock to impound the water reservoir. When side-valleys or depressions along the side of an expanding (or surging) glacier become truncated and obstructed, ice-dammed lakes can form. After the Little Ice Age, several similar lakes developed in high mountain locations (LIA). As the glaciers recede, the ice dam's stability is lost, and the lake may either drain dramatically or stay trapped behind the former glacier's lateral moraines. A collapse of such a lake was implicated in the recent 2013 GLOF disaster in Kedarnath, India (Allen et al., 2015). New lakes could emerge in a newly uncovered glacier forefeld, which is blocked downslope by a surviving glacier, once formerly confluent glaciers retreat. The most well-known subglacial lakes originate beneath glaciers in Iceland, where their formation (and drainage) is associated to geothermal and volcanic processes. Outbursts from ice-dammed water reservoirs inside or under a glacier, involving draining of supraglacial ponds through englacial pathways, have been described in most mountainous regions of the world, with links to heavy rainfall events or increased melt during hot temperatures (Benn et al., 2012; Huss et al., 2007; Richardson and Reynolds, 2000a; Rounce et al., 2017). The size and lifespan of supraglacial lakes are limited by the timing of linkage to the englacial drainage system, according to recent research from the Tien Shan, with continuous monitoring necessary to detect rapidly growing risks (Narama et al. 2010; 2017). Tunnels expanded by thermal and mechanical erosion are the primary conduits for subglacial or englacial drainage. The specific process that causes this outflow of water is generally unknown, although one possibility is hydrostatic flotation of the glacier dam once the trapped water volume reaches a threshold. When lake levels are equivalent, outburst floods related to tunnel expansion often take longer to develop and with lesser peak discharges than other GLOF processes. Even though the relevant mechanisms are not fully understood, faster sub- or englacial drainage occurrences have been reported.

Because of the extensive retreat of mountain glaciers since the Little Ice Age, lakes imprisoned behind proglacial moraines have formed, some of which are extraordinarily huge, with volumes of up to 100

million m^3 and depths reaching 200 m. (Cook and Quincey, 2015). Dam constructions up to 100 meters tall can be fragile and vulnerable to breaching due to the unconsolidated nature of morainic debris, that can be ice-cored. At the beginning, the hydraulic gradient across the dam can cause seepage, fine sediment removal, and degradation on the dam's downstream side. The inner integrity of the dam can be compromised by ice core deterioration, making it more vulnerable to dam collapse. Second, backward channel erosion such as wind-induced wave action or the break-through of a temporary outflow channel obstruction, might incise the obstacle and cause overflow. Finally, a quick inflow of water into the pond from rain or snowmelt or the formation of displacement waves by mass movements of ice or rock avalanches, can enhance water flow down the outflow channel and commence incision. The hydrological, geomorphological, and geological properties of the surrounding slopes and watershed region of the lake become essential parts of the hazard assessment in the event of a sudden inflow of water or a floodwave caused by a mass movement. Earthquakes can cause mass movements in a lake or destabilize a dam building directly. However, empirical findings are limited, and the 2015 Gorka earthquake in Nepal caused no significant moraine dam instability, probably due to the lakes' placement in flat valley-floor areas where ground acceleration was typically low (Kargel et al., 2016).

When a conduit is cut through a moraine dam and lake outflow increases, erosion is aided and the fracture is widened, lake flow expands even more, and a self-enhancing mechanism is facilitated (figure5.1). Typically, this proceeds until outflow drainage begins to reduce, together with shear pressures applied to the earth, and erosion processes slow or end. The dam's composition (e.g., clast size, buried ice, vegetation) and geometry (e.g., height, width, slope) are important not only for the dam's initial stability, but also for controlling the rate of degradation and the final depth of any breach, that are key considerations for the flood hydrograph. Moraine breaches often result in a significant reduction in lake water level, and the ensuing expanded channel typically prevents new hazards from arising, unless the lake is further enlarged and deeper, such as a consequence of further glacier retreat and shrinking. Furthermore, displacement waves from massive mass movements can occasionally overtop a moraine dam and create an outburst event without ever breaching the dam, implying that subsequent occurrences are still a possibility. Because the dam structures themselves are deemed stable, overtopping waves are the only way for a disastrous flood to occur in bedrock dammed lakes. For the comparable flow conditions, GLOFs create significantly larger erosive forces than conventional meteorological floods. Unlike meteorologically caused floods, GLOFs tend to quickly dissipate downstream, posing a threat to potential consequences and damages (Schwanghart et al., 2016b). The initial volume and length of the breach/outburst occurrence are connected to downstream attenuation of floodwaters, and with small volume short duration occurrences attenuating is the fastest. However, in long stream channels such as those in the Himalayas and the Andes, dynamic flow shifts from early debris flow types to hyper concentrated flows, and perhaps return to debris flows, are frequently recorded for GLOFs, depending on stream inclination and erodible material availability. Flood channels of up to 100 kilometers and even longer have been seen.

Figure 5.1. Many years after the 1997 flash flood of moraine-dammed Queen Bess Lake, the west fork of the Nostetuko River valley in British Columbia. The flood deposited massive volumes of coarse sediment and damaged the valley ground's which was before stream channel and floodplain (Clague J.J., 2013).

Destructive debris flows damaged the village of Kedarnath in Uttarakhand, northern India, on June 16 and 17, 2013. Following many days of unusually heavy rainfall, a small lake dammed near the lateral margin of the Chorabari glacier (blue arrow) overtopped and burst, causing the most damage and catastrophic casualties. A crucial contributor was undoubtedly the relatively quick spring melting and runoff into the lake in the previous month.

Figure 5.2. Overview of breached part of Chorabari lake and village of Kedarnath in downstream after disaster (Kaul, 2013)

Figure 5.3. village of Kedarnath in downstream before disaster.

Figure 5.4. village of Kedarnath in downstream after disaster.

5.2.2 Rock Avalanches

Bedrock slope collapses involving high-velocity downslope flow-like movement of fragmented source material that originated from an unbroken rock mass are referred to as rock avalanches (Hungr et al., 2001). Even though terminology is commonly used similarly in the literature, there is a significant contrast between rockfalls and landslides, which entail smaller-scale removal of unstable bedrock, whereas rockfalls can expand to destabilize a much bigger rock mass. A key factor of erosion and deposition in high mountain environments is rock avalanches, which are caused by steep topography, high relief, unstable geological features, and seismicity coupled with transitory climate-driven glacial, paraglacial, and periglacial mechanisms (Evans and Delaney, 2015). When a result of decreased friction and the integration of greater mass as the flow moves across snow and ice covered terrain, the subsequent effects and social implications can be far-reaching (Deline, 2008; Evans et al., 2009; Evans

and Clague, 1988; Schneider et al., 2011). Despite the fact that paraglacial and periglacial controls on bedrock stability are complex, operating on a variety of spatial and temporal time scales, there is convincing empirical information proving a temporary increase in slope instability following deglaciation, as well as enhanced instability from within warm permafrost locations (Deline et al., 2015). Large slopes have been degraded at their lower ends by glacial and/or fluvial activity in glacial or previously glaciated areas. The following retreat of glacial ice causes a debutressing effect, in which the ice's stability is eliminated (Ballantyne,2002). Stress-release fragmentation can grow in the rock layers as an outcome of this unloading, resulting in new planes of failure (McColl, 2012), while previously insulated surfaces are subjected to hydrological and hydraulic variations, as well as changed mechanical and thermal erosion regimes (Haeberli et al., 1997; Wegmann et al., 1998).

Heavy rainfall is a well-known cause of landslides on lowland mountain slopes, and it's been related to certain recent high mountain rock avalanche incidents (Hancox and Thomson, 2013; Paranunzio et al., 2016). Many recent rock avalanche events seem to have been initiated by extremely warm temperatures predominant on the order of days to weeks (Allen and Huggel, 2013; Paranunzio et al., 2016), especially in the European Alps, where some of the most sudden atmospheric warming over the past century has been noticed. These occurrences are usually small to medium in size, and they may be connected to permafrost melting, active layer deepening, or quickly rising pore and pore water pressures due to melting snow and ice. Furthermore, numerous big rock avalanches have happened without apparent meteorological or seismic triggers, when the cumulative deterioration in rock mass strength in response to long-term static stress and different conditioning processes appears to exceed an inherent threshold (e.g., Eberhardt et al., 2004; Hancox et al., 1999; McSaveney, 2002).

Figure 5.5. Pizzo Cengalo, Bondasca valley, southern Swiss Alps: rock avalanche and debris flows. image of the rock slope failure zone following the 3 million m3 avalanche on August 23, 2017. Debris flows originated at the toe of the rock slope failure on August 23, 2017, and transported considerable material from the rock avalanche (swisstopo, VBS, SDA).

5.2.3 Debris Flow

Other non-outburst relevant debris flows can also arise from steep moraines, talus slopes at the foot of eroding rock walls, and fluvio-glacial deposits within steep stream channels (Evans and Delaney, 2015). Once mobilized, debris flows are composed of a fast-flowing combination of silt and water, with one or more pulses (Iverson, 1997). The quantity of sediment varies, although it usually accounts for 50 to 70% of the total volume. Considerable eroding potential, movement of huge boulders, poorly sorted deposits, and levee production in response to flow slowing over flatter terrain are all diagnostic properties (Hungret al., 2001). The abundance of loose, poorly consolidated material, combined with steep terrain, melting snow and ice, and heavy convective or precipitation, makes peri- and para-glacial zones favorable for debris flow onset (Allen et al., 2015; Chiarle et al., 2007; Evans and Clague, 1994; Jomelli et al., 2007). Extremely warm temperatures and associated melting of snow and ice, as well as significant precipitation, are typical trigger mechanisms (Chiarle et al., 2007; Jomelli et al., 2007). In the Swiss Alps, excessive rainfall generated roughly 600 debris flows in 1987, with more than half of these occurrences originating in zones that had deglaciated over the previous 150 years (Rickenmann and Zimmermann, 1993; Zimmermann and Haeberli, 1992). Debris flow activity has also been seen in Southern Russia as a result of recent fast deglaciation and exposure of morainic material, with source sites frequently becoming oversaturated with meltwater or surface runoff (Seinova et al., 2011; Stokes et al., 2006). Groundwater filtration can be delayed by cold permafrost bodies, resulting in local saturation of the non-frozen material above (Zimmermann and Haeberli, 1992). Thawing permafrost in non-consolidated material causes a loss of cohesion and a rise in porewater pressure, as well as collapsing and the disappearance of enormous ground ice masses (Harris, 2005). Because deglaciated terrain takes a long time to re-vegetate, peri- and paraglacial landscapes can be left vulnerable to erosion for decades or more (Kääb et al., 2005).

There is a significant periodicity to debris flow activity, with occurrences happening more often in the summer and autumn in the European Alps (Rebetez et al., 1997; Stoffel et al., 2011), and in the summer in the Caucasus (Rebetez et al., 1997; Stoffel et al., 2011). (Perov et al., 2017). During these hotter seasons, not only is prompting from strong convective rainfall or melt-related mechanisms more likely, but sediments are less probable to be frozen, resulting in more material available for eroding. There is a strong link between debris flow activity and the formation of the active layer, especially in permafrost conditions. As a result, by late summer or fall, slopes are most susceptible to destabilization due to slow melting of the surface material.

Figure 5.6. Looking south toward the Skalistyi Mountains, a glacier ice mass deposit in the Karmadon Depression. Roads leading to the buried village of Nizhniy Karmadon on the left side vanish beneath the ice and debris. To the right of center, a large temporary dammed lake has formed in the village of Gornaya Saniba, and the narrow valley in the Skalistyi Mountains (the Karmadon Gates) is seen just above the left of center (helicopter photo by Igor Galushkin, 6 October 2002).

5.2.4 Ice Avalanches

Ice avalanches are most commonly caused by ice detaching from either a glacier's steep frontal part or a sloping glacier bed (Alean, 1985). The occurrence and size of a disastrous break-off are determined by a number of major parameters. The shear strength of the glacier ice at the base, which is affected by temperature and hydrological conditions, the slope and form of the basal slope, and the tensile strength of the glacier body itself are all factors to consider (Evans and Delaney, 2015). Ramp-type destabilization caused by cold-based glaciers, on average, need a steeper critical sliding surface than polythermal or temperate glaciers. Faillettz et al. (2015) used a combination of tracking and analysis to better understand the thermal controls on glacier instability, identifying three scenarios:

- Cold-based glaciers which are completely frozen to their bedrock, with increasing internal damage owing to changes in glacier geometry including mass acquisition and thickening towards the front, causing instability. The ultimate mechanical fracture happens within the ice in this situation, commonly a few meters above the bedrock.
- Polythermal glaciers having a temperate zone that are partially frozen onto their bedrock. The final fracture in this scenario happens right on the bedrock in the glacier's temperate zone and has the potential to spread through the ice. Liquid moisture is present, but not flowing in the glacier and plays a significant role in the evolution of the destabilization.

- Sliding on bedrock is a problem for temperate steep glacier tongues. The ultimate breach happens immediately at the bedrock in this scenario, and flowing water is present at the glacier-bedrock contact. Rapid fluctuations in subglacial water pressures produce destabilization, which necessitates a crucial geometrical arrangement such as a steep slope, no frontal abutment, and convex bed topography.

Because glacier beds often steepen and basal freezing increases with elevation or decreasing air temperatures, these fundamental mechanisms suggest a strong topo-climatic influence on glacier instability. As a result, a change in air temperature can affect the potential for ice avalanches in two ways: directly by affecting the glacier's thermal regime, and indirectly by modifying the glacier's shape. Regardless of how the collapse begins, the ice mass deteriorates as it flows downslope, resulting in a high-velocity, highly dynamic flow of fragmented ice. Although significant entrainment, flow modification, and cascade processes are feasible, total runout distances are generally linked to initial detached volume. Cliff-type circumstances are typically connected with smaller, more frequent, and repeating occurrences, and they reflect a natural ablation mechanism for these glaciers to some extent. Impacts into glacial lakes and associated displacement waves are a substantial and regular hazard, especially in cirque basins where lakes form below high glaciated headwalls. Ramp-type conditions generate ice avalanches that are less common but larger and able to reach and affect the downstream area.

Ice avalanches with a huge mass have been documented in the European Alps, North America, the Andes, the Himalayas, and Tibet (Schneider et al., 2011). Huge segments of fairly flat valley-type glaciers seldom collapse. The Kolka glacier in the Russian Caucasus (2002) (Evans et al., 2009; Haeberli et al., 2004; Huggel et al., 2005), which was destabilized by a sequence of ice and rock avalanches from the steep slopes behind, and the extraordinary twin ice avalanche occurrences in the Aru Cru Range, Tibet (2016), are two recent instances (Tian et al., 2017). Even though surging attitude has been associated to some instances and was clearly noted previous to the occurrences in Tibet, knowledge of the procedure is still restricted. Loss of shear resistance at the glacier bed due to the growth of excessive water pressures from rainfall or melting, particularly in polythermal bed conditions, mass loading due to snow deposition, and mass redistribution or loading from other mobilizations landing on the glacier ice are all proposed causal mechanisms contributing towards such disastrous detachments (Evans and Delaney, 2015). Ice avalanche activity is frequently preceded by increased glacier movement and the production of tension fractures and crevassing at the surface; however, this is not always the case, and collapses can emerge without obvious warning indications (Faillettaz et al., 2016). Seismic activity can also cause ice avalanches to occur unexpectedly. Although most of the time this is due to breakdown of the underlying bedrock (e.g., the Huascaran tragedy in 1970 in Peru), there have been instances where only little rock debris is seen in the avalanche deposition (van der Woerd et al., 2004). The recent 2015 Langtang catastrophic event, was mostly attributed to a seismically snow-ice avalanche (Fujita et al., 2016).

We are interested in detecting possible climate change signals in a number of disastrous (>105 m^3), collapses that have occurred in glacierized or formerly glaciated locations in the European Alps, the Americas, and the Caucasus during the last fifteen years. Table 5.1 summarizes these incidents. Rock slides, rock avalanches, debris flows, and ice–rock avalanches (sensu Cruden and Varnes, 1996) are among the events in collection that were not generated by earthquakes. Despite the fact that such landslides were relatively uncommon during the historical period, they have resulted in significant devastation and casualties (Eisbacher and Clague, 1984; Haeberliet al., 1989; Huggel et al., 2005; Pralong and Funk, 2006).

Location	Date of Incidence	Volume of Mass Failure [$10^6 m^3$]	Maximum Failure Elevation [m a.s.l]	Relation to climate
Mount Meager, Canada	6/08/2010	48	2400	Long-term glacier retreat causes debuttressing, most likely due to thawing permafrost in the source zone of rock slope collapse.
Ritzlihorn, Switzerland	2009-2010	>0.3	3260	Permafrost melts in the rock fall source zone, and days of hot weather precede collapses and debris flows.
Lower Grindelwald glacier, Switzerland	2006-2010		3000	Long-term glacier retreat causes glacial lakes, debuttressing, moraine and bedrock collapses, and likely warms permafrost in the rock fall source zone.
Mount Miller Alaska	6/08/2008	22	2200	Warming permafrost and steep glacier ice; days-weeks before failure, warm, melting weather
Monte Rosa, Italy	21/04/2007	0.3	4000	Permafrost incidence; unusually warm temperatures days-weeks before collapse; massive ice retreat and bedrock failures in surrounding locations in past years and decades;
Alpine debris flow Rotlaui, Switzerland	22/08/2005	0.5	2400	Due to recent glacier retreat, there remained abundance of glacial sediment in the source zone; permafrost in the sediment body. Extremely High Precipitation
Thurwieser, Italy	18/09/2004	2.5	3725	Warming permafrost through several meters deep in the bedrock, ridge condition
Kolka, Caucasus, Russia	22/09/2002	130	4300	Warming permafrost and steep glacier ice are most likely to blame.
Mount Harold Price, Canada	24/06/2002	1	1720	Warming of steep rock slope; rockslide transformed into a debris flow
Salcantay, Peru	27/02/1998	25	4200	Large accumulated rainfall amounts, warm temperatures implying a high snowfall line and additional liquid water from ice and snowmelt; abundant glacial sediment in source zone due to glacier retreat;
Mount Cook, New Zealand	14/12/1991	60	3755	Warming permafrost through several meters deep in the bedrock, ridge condition

Table 5.1. Selected recent slope collapse incidents and their relationship to climate and climate change (Huggel.,2012).

5.3 Process interactions of Glacier Hazards

5.3.1 Temporal and Spatial Dimensions of Hazard

Glacier and permafrost hazards have a broad range of temporal and spatial aspects. Small volume icefalls and rockfalls happen practically every day in dynamic mountain environments, specifically during warm season when occurrence frequencies might be tightly connected to daily warming and melting. The concerns caused by such hazards are normally localized within the high-mountain environment, but they might be concerning in areas where significant numbers of recreationalists (like climbers) walk exposed pathways (Temme,2015). Through the other end of the scale, fairly infrequent but great magnitude avalanches of ice and/or rock have the ability to achieve long runout distances and

hence endanger the public people and infrastructure placed far downstream, specifically when incidents transition or procedure chains begin (Schneider et al., 2011).

Non-climatic and human causes and triggers must be excluded before a climatic influence can be attributed to a specific sample of landslides. However, due to inconsistency or bias in landslide reports, statistically rigorous analysis is problematic. We concentrate on high-mountain places where human influences are absent or minor, and where temperature-sensitive snow, glaciers, and permafrost may affect slope stability. Climate change might affect the rates of physical and chemical weathering, as well as the degradation of permafrost, all of which could affect the bulk strength qualities of slope-forming materials (Harris et al., 2009). Infiltration rates and pore-water pressures are affected by changes in rainfall frequency and magnitude, as well as the erosional effectiveness of fluvial mechanisms. Increased rainfall may alter hillslope stability by causing dynamic loads during high-intensity rainstorms, slope undercutting, or redistributions of topographically produced stresses in rock slopes (debuttressing effects) (Augustinus, 1995; Ballantyne, 2002). The timescale on which climate change impacts slope stability and landslide hazards is obviously significant (Figure 5.7). Debuttressing effects, for example, can have millennia-long lag durations but can also occur on timescales as short as decades.

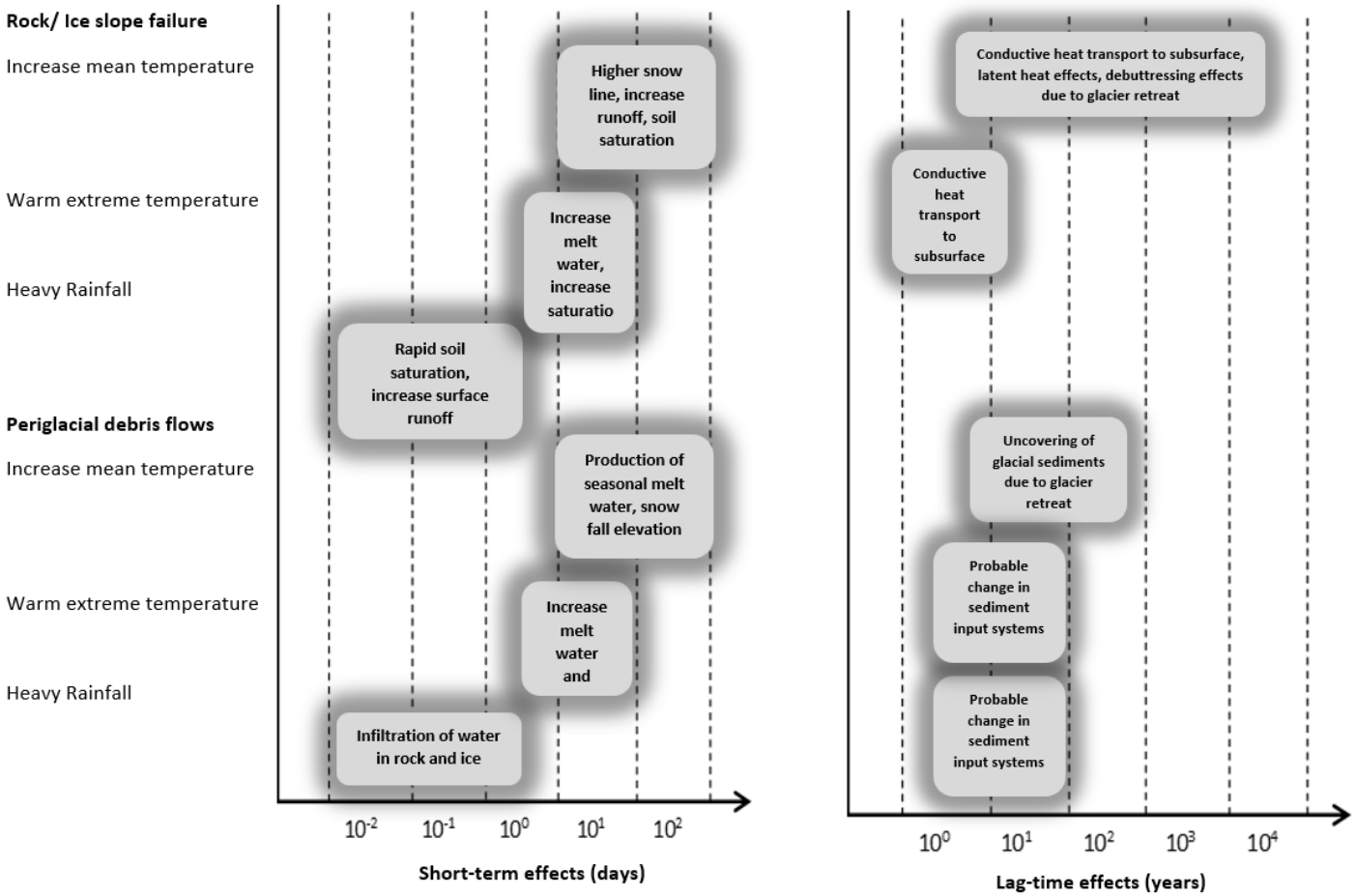

Figure 5.7. Mechanisms that impact slope stability and climatic drivers have temporal dependencies. Short-term impacts, lasting minutes to months, are separated from long-term consequences, lasting years to millennia. The grey bars represent an estimate of timescales, but they illustrate the variation in the different mechanisms.

5.3.2 Compound Events and Process Chains

The requirement to examine interacting processes and their cumulative downstream consequences is a defining feature in the evaluation of glacier and permafrost hazards. In fact, similar process chains have been engaged in some of the most catastrophic and far-reaching disasters in high mountainous areas, beginning with ice and/or rock avalanches and processing downstream as debris, mud, or hyperconcentrated flows (Huggel et al., 2005; Lliboutry et al., 1977). As in the situation of a mass movement falling into a lake and generating an outburst flood, the interaction between processes might be instantaneous (i.e., seconds to minutes). Other interactions, such as a landslide deposit damming a lake or a surging glacier, might lead in a secondary hazard that develops over days, weeks, months,or even years(Schneider et al. 2013; Korup and Tweed 2007).

Several researchers have well characterized one example of a common process chain involving huge flow of ice or rock into a glacial lake, and it is becoming increasingly important in view of lakes emerging in close vicinity to steep, destabilizing mountain flanks (Haeberli et al., 2016). While many scientific and technical groups have created modeling methodologies for separate processes such as wave generation, dam breach, flow propagation, these approaches were never designed for integrated GLOF modeling, which is a major barrier for hazard assessment. Schneider et al. (2014) published one of the first applications of a coupled mass flow and lake impact model as a baseline for hazard assessment in Peru. The biggest uncertainty about the overtopping wave in this case came from the original scenario definition for the rock/ice avalanche, emphasizing the necessity of the first slope stability evaluation. With two-phase mass flow models, recent efforts were made to provide model methods capable of modeling the whole chain of interacting mechanisms. There are significant links between rockfall, rock avalanches, and debris flow activities over longer time periods (months to years or more) (Frank et al., 2015; Tobler et al., 2014).

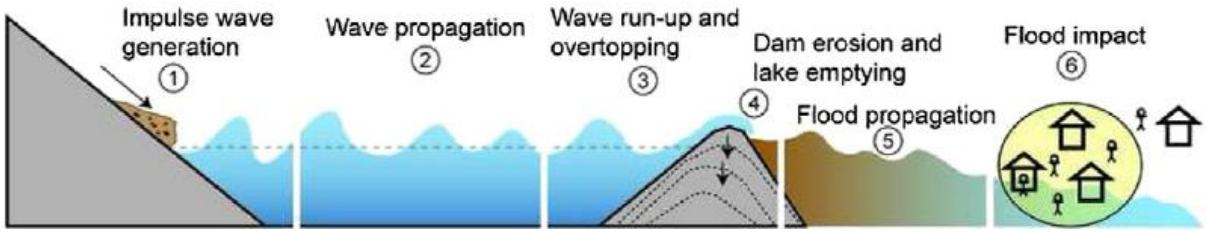

Figure 5.8. A typical glacial lake outburst chain emerging from an initial mass movement is depicted in this figure. (1) A mass movement (ice, rock, or debris) enters a lake, causing a displacement wave that (3) overtops and erodes the dam section. (5) A flood then moves downstream, damaging population areas and infrastructure. Note that displacement waves can be disastrous with or without dam erosion, providing a hazard to even seemingly stable bedrock dammed lakes.

5.4 Potential Hazards in our case study

Generally, the type of physical mechanism involved, the scale of the occurrence, and its probability or frequency can all be used to identify a natural hazard. Detecting and characterizing probable hazard sources is thus a critical initial step in assessing glacial, peri-, and paraglacial hazards. Multidomain classification techniques that combine spatial, spectral, and temporal information are particularly promising for this challenge due to the complexity of high-mountain activities.

5.4.1 Miage Glacier

This glacier contains some lakes who history over the previous 162 years has been distinguished by terrain changes and lake-level oscillations including many draining episodes. According to a bathymetric investigation, the lake is divided into two basins by a partially submerged moraine (figure 5.9). The limnological properties of each basin are unique. In the summer, melting icebergs, wind-driven surface currents, thick meltwater underflows, and other variables impact the thermal structure of the ice-proximal basin. There was just one basin in 1905, but it was separated into two separate basins in 1916, the first reaching from the ice cliff to the more recent moraine ridge, and the second, smaller, to the west. According to Sacco's 1918 studies, the lake was once again a single aquatic body behind a 30 m high ice wall in 1917 (Sacco, 1919). Capello recorded a single water body with a surface around the current height (2020 m a.s.l.) in 1929, but the lake began to slowly drain in August 1930, leaving a remnant lake on the western side and a tiny pond near the ice cliff (Capello, 1940). On 10–13 August 1950, a drainage incident happened, leaving a residual lake in the western sector and a small pond on the eastern side, as in 1930 (Cerutti, 1951). The lack of silt in the southeastern basin revealed an ice floor that extended to the northern moraine ridge (Nangeroni, 1950–51; Saibene, 1951). Debris-filled fractures and breaks in debris-rich ice punctured the ice floor. Recharging began in the autumn of 1950, and both the west and east basins were completed by 1951 (Lesca, 1956).

As a result, the history of Miage glacier lakes shows frequent outflow and refilling. Owing to glacier melting, enormous lakes arise as a response to abrupt climate changes and rising temperatures. There is also a chance that new lakes will arise as a product of debris flow on the glacier's surface. These lakes could become hazardous if the dam breaches and outflow discharges begin, causing damage to downstream lands and facilities.

In general, para- and peri-glacial landscapes are characterized by an abundance of steep, unconsolidated material, making them extremely susceptible to debris flow activity, which can be triggered by excessive meltwater or severe precipitation. In this example, the Miage's slope is indeed not steep enough to cause debris flow; but, significant rainfall and an extremely warm environment that causes glaciers to retreat can cause debris flow in this area.

Figure 5.9. The lakes formed in the Miage Glacier and their area

5.4.2 Brenva Glacier

Brenva Glacier began advancing in 1913, and by 1919-20, it was creeping forward at a rate of 20-25 m/a. A rock avalanche of >2.4 Mm^3 of rock and >7.5 Mm^3 of ice covered the entire lower glacier and a portion of the upper glacier in 1920. (Deline,2009). While both glaciers feature right-lateral moraines of comparable height (>200 m for the Brenva, but partially covered for the Miage) and a 40 degress mean slope angle, the Brenva moraine has a basal thickness of 65 m to 90 m, compared to just 25 m for the Miage. Gravity deposition, melting water, and glacial outbursts all contribute to the formation of this basal over thickness, which causes breaches in the lateral moraine crests. On the Brenva Glacier, these events are very common. The primary Brenva moraines breach originated in 1928 (Orombelli & Porter, 1982) and reopened during the latest glacial advance, which peaked in 1986, while eight other minor breaches emerged during this time. The distal side of the moraine, below the 1928 breach, has debris flow deposits covering an area 100-200 m wide, with traces of recent activity. During the retreat

of the glaciers, according to the topographic reconstruction of the upper Val d' Aosta Glacier, late glacial period was depicted by a thickness drop of 200 m in the upper Brenva Glacier. When the ice pressure stopped, this drop might have resulted in the destabilizing of rock wall bases owing to rock relaxation. The glacier's debris source was most probably quite active, and lateral moraine cores would have formed quickly. Rockwall equilibrium was more or less established over geological time, although rock failures could still occur owing to climate changes. The rock avalanches of 1920 and 1997 correspond to two strong warming periods, however the warmest era of the 1940s, did not result in a rockfall. During the warmer months, water runs mostly in gullies in the Mont Blanc Massif, while minor rockfalls happen on climbing routes: the many snowfalls during this period are quickly transformed to water, which seeps deeply into the crevasses, causing extremely high hydrostatic pressures (Bozonnet, 1994). The Directissime Americaine and the Thomas Gross routes, for example, were largely devastated by the Drus rockfall (09/1997, 13 500 m^2). During the same warmer months of 1997, many rockfalls occurred on the Aiguille Noire de Peuterey SE face, over 3000 m height, resulting in a dense brown fog that lasted in the Fauteuil des Allemands cirque for several days.

Changes in observing conditions could explain for an increased frequency of these events, however ice melting is a possibility. Ice-cemented blocks ranging in size from 0.5 to 2 m in volume were found in the Val Pola rock avalanche's deposit (07/1988, Valtellina); this implies that permafrost-related mechanisms, including ground ice melt caused by climatic warming and connected variations in groundwater regimes could have played a role in stimulating the landslide, according to the researchers (Dramis & alii, 1995). Despite its elevation, the 1997 Brenva scar bottom reveals running water being a south-facing spur, the Gendarme Rouge is quickly cleared of snow in the warmer months.

Figure 5.10. locations of rockfalls in upper part of Brenva Galciers in years 1920 and 1997

Because no indirect dating of Holocene activity has been discovered due to deposit features, and the three most recent events (14th century, 1920, 1997) took place during warmer months, it is difficult to describe the Brenva rock avalanches by climatic changes. Nevertheless, the first rock avalanche remains hypothetical, while the 20th century incidents happened at the beginning and end of the current post-Little Ice Age warming interstage. Furthermore, the proximity of these two occurrences over a period of 77 years might imply increase activity in the region, while the presence of a settlement implies that the Middle Ages were morphodynamically steady, as was the main portion of the Little Ice Age. The Brenva Glacier basin's geometry, coupled with the lower glacier's SE orientation, describes

that why main rock avalanches cross the glacier, and the basal over thickness of debris that has created distal to the right-lateral moraine, indicates that rock avalanche activity has lasted throughout the Holocene.

Furthermore, debris flow from the Brenva might form a natural dam, with the river stream filling the dam until it is overtopped or the dam is breached. This technique has the potential to flood the town downstream. The size of the flood, on the other hand, is highly dependent on the debris flow material, river discharge, and dam capacity.

5.4.3 Freney & Brouillard Glaciers

The Freney and Brouillard glaciers are steep mountain glaciers in the Mont Blanc massif, located near Courmayeur in the upper Veny Valley. In contrast to valley glaciers, mountain glaciers have no or only a little tongue and do not flow far enough down to reach the main valley. The Freney runs through a steep, narrow hanging valley on the southern flank of Mont Blanc de Courmayeur. It is separated from the twin glacier of Brouillard, which runs parallel to it (figure 5.11). The two important debris-covered glaciers of the Italian Mont Blanc range (Miage southwestward) and Brenva (northeastward) spread their long black tongues not far from the Brouillard and Freney glacier. The Freney and Brouillard might be representative of a large number of tiny glaciers (less than 1 km^2); one widely discussed topic is how these glaciers will survive in the next decades as a result of global warming. In the twentieth century, Italian glaciers experienced a broad retreat (Citterio et al., 2007). Small glaciers had a significant role in overall area loss; in fact, the smaller the glacier, the faster it shrank; therefore, its extinction is more than a hypothesis. Glaciers running down a small valley in high mountain terrain, such as the Freney, are, on the other hand, subjected to a stronger shading.

Massive cliffs surround these glaciers, which can be hazardous if melting water from snowfall and glaciers seeps into the rocks, causing high hydrostatic pressure and, eventually, rockfalls. Furthermore, during periods of excessive heat, high melting of glaciers causes an increase in flow and volume of water downstream of these glaciers. This can be coupled with Miage glacier retreat or lake outbursts surrounding Miage, resulting in a large volume of water in river streams, posing a flood hazard to nearby lands.

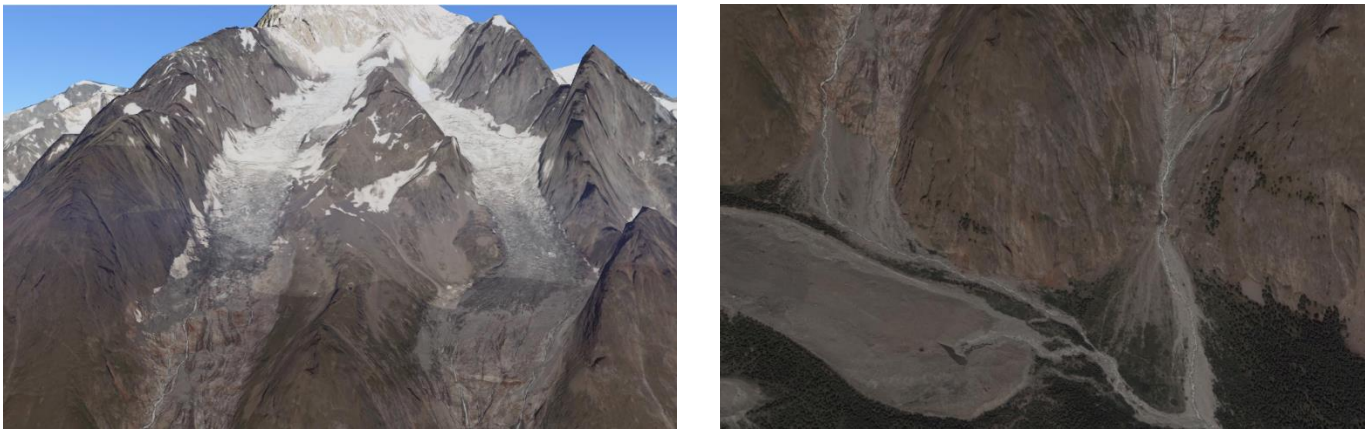

Figure 5.11. (Left) High rock walls around Freney and Brouillard (Right) streams flow to the main river of the Val Veny from Brouillard, Freney and Miage.

5.5 Conclusion

Because of the changing glaciers in the Val Veny area as a due to climate change, it is vital to evaluate the possible hazards that each glacier in this area poses. According to the findings, any glacier can have a variety of glacier-related hazards, but one of them is the more likely depending on the glacier's morphology and topography. It is also feasible to draw a link between climatic change and the kind of occurrence based on the history of incidents in each glacier.

The most probable glacier-related hazard that can happen in Miage glacier, is GLOF, because it contains some glacial lakes that can outburst and flood surrounding lands. In addition, high amount of melting can increase the discharge in the river if it combines with melting water of other glaciers and leads to outflow of water in main river stream. Artificial outlets, pumping, or tunnels might be used to lower the lake level, reducing the risk potential. Because the lake's remoteness may preclude large-scale development projects, widening or deepening the river channel along the GLOF route may be a viable option. Early warning systems can also lessen susceptibility, allowing occupants to protect precious goods or, at the very least, their lives. The reaction time for GLOF incidents is longer than for quick mass movements, allowing for the development of warning systems or the creation of an evacuation strategy. The most potential hazard in Brenva Glacier, based on past incidents, is rockfall in the upper section. Rockfalls are more likely around this glacier because of the high cliffs that surround it. Although, owing to Brenva's steep slope and debris-covered glaciers, debris flow is a possibility, which might result in the development of a natural dam upstream the town, with dam breach or overtopping flooding the city downstream. Although no major natural catastrophe has been reported in the Freney and Brouillard glaciers, the existence of high cliffs and a steep slope in the upper parts of the glaciers makes rockfall and avalanche threats probable. Furthermore, at warmer times of the year, a large volume of melting water can boost river discharge, especially when paired with melting water from neighbouring glaciers.

Due to the complexity of triggering conditions, uncommon occurrence, accessibility limitations, and the transitory time period involved, there is still a long way to go in understanding the formation mechanism and triggering factors of debris flow. Future research should focus on determining the failure mechanism and thresholds of rock, ice-rock and moraine slopes, as well as estimating dynamic loose sediment refilling in response to climate change. Attempts to improve the spatiotemporal resolution of climate data in mountain cryosphere and integrated field monitoring of debris flow initiation and propagation should also be stepped up.

Chapter Six

6. Conclusion

Archival photographs were utilized in this master's thesis to better understand the evolution and dynamics of glaciers in Val Veny from 1967 to 2006. Photogrammetric methods can be used to interpret morphological change captured in a sequence of aerial photographs. These data were given by IGNF and covered an area ranging from 132 to 345 km^2 and they were acquired with various cameras during the warmer months of the year. Although the camera coordinates were included in side information of photos in some datasets, none of the images contained GCPs since they were captured for purposes other than photogrammetric ones. To understand the variation of glacier through these years, 3D models obtained from these data were compared.

The 3D model of each series of photos was reconstructed using the Structure from Motion approach. Some pre-processing was conducted before the main procedure to improve point extraction from photographs in this approach. Furthermore, image overlapping plays an essential role in image alignment, and better reconstruction was produced in spots with larger overlapping. According to availability of certificate of dataset, it was possible to try the alignment procedure by using fiducial markers. However, in most of the datasets, masking out the fiducial markers leads to better or equivalent results. Satellite data was used to pinpoint stable spots that were used as GCPs in all images, resulting in improved initial alignment of the 3D models during the comparison phase. The appearance of shadows on the glaciers in some zones is due to the presence of high cliffs and improper photography timing, and this fact leads to missing data in some portions of the 3D model.

To use 3D models to discover variations in glaciers, noises must be eliminated and model alignment must be accurate enough to provide an accurate result. The distances between the stable zones may be used to measure the registration and alignment quality of two models. The error in the registration procedure may be seen in the mean distances in these places. The registration error varies depending on the quality of the 3D model in different zones of Val Veny, but it is usually between 1 and 2 meters. Multi-scale Model to Model cloud comparison was employed to determine distances, as recommended by prior studies, especially for complex landforms.

In the Miage Glacier, height loss was determined to be 1 m/year between 2000 and 2006, after being almost negligible until the 1990s. The height difference in Freney and Brouillard fluctuated near zero until 2000, when it dropped dramatically to approximately -10 meters until 2006. Brenva Glacier, which underwent a height change rate of -3.5 m/year around the turn of the century, has the greatest values of height change rate and height drop among the comparisons. The mass loss of all the glaciers in this area has been rising during the last 40 years. These findings, when combined with local meteorological data, revealed that the overall trend of glacier mass loss was caused by a general rise in temperature over the warmer months of the year. Furthermore, massive glacier losses occurred at a time when temperatures were higher than average, ranging between 25 and 30 °C. According to local snowfall records, the glacier minor height growth in some periods was most likely owing to heavy snowfalls. Due to frequent snowfall up to 50 cm till 1999, all glaciers saw a considerable height rise of up to 3 meters before 2000.

Increasing glacier height change rates when the average temperature rises throughout the warmer months of the year in this area might result in a variety of glacier-related hazards. Depending on the morphological qualities of the glaciers, the sort of hazard might vary. The existence of certain lakes

near the glacier tongue on the Miage glacier might raise the risk of Glacial Lake Outburst Floods in the case of either excessive melting water during warm seasons or rockfalls from the Freney and Brouillard glaciers. Brenva glacier's proximity to the city in its downstream makes it more essential in terms of hazard assessment. The primary hazards that may arise from the Brenva glacier are rockfall avalanches in the upper section and the potential of a natural dam formation at downstream as a consequence of debris flow.

The findings of this study can be integrated with additional hazard assessments. Indirect geomechanical studies on the rock mass in the upper parts of the Brenva, Freney and Brouillard Glaciers could be conducted to analyse the spatial distribution of joint sets and possibly evaluate the size of the block most susceptible to collapse. A detailed study at the debris accumulation might reveal the sediment granulometry, which could be used to assess the internal stability for the case of debris flow.

While our study covered a broad region, the integrated photogrammetric technique is easily adaptable to smaller and similar-sized glaciers, where it might give a thorough evaluation of hazards and thickness variations and be valuable in natural hazard management. Furthermore, the findings of this study may be integrated with more contemporary models acquired using more advanced photogrammetry technology to assess whether the variance in glaciers of the area follows the same trend as before. Due to recent advancements in the SfM algorithm, similar work from this master's thesis may be applied to various applications or locations if archival photographs are available. Unidentified causes of natural disasters, including landslides, floods, and droughts, can be identified by analysing archival photographs of the region and using the results for risk mitigation and planning in the long term.

Bibliography

Aguilar, M., Aguilar, F., Fernandez, I. and Mills, J., 2013. Accuracy assessment of commercial self-calibrating bundle adjustment routines applied to archival aerial photography. *The Photogrammetric Record* 28(141), pp. 96–114.

Alean, J.: Ice avalanches: some empirical information about their formation and reach, J. Glaciol., 31, 324–333, 1985.

Allen, S. K. and Huggel, C.: Extremely warm temperatures as a potential cause of recent high mountain rockfall, Glob. Planet. Change, 107, 59–69, 2013.

Allen, S. K., Gruber, S. and Owens, I. F.: Exploring steep bedrock permafrost and its relationship with recent slope failures in the Southern Alps of New Zealand, Permafr. Periglac. Process., 20, 345–356, 2009.

Allen, S. K., Rastner, P., Arora, M., Huggel, C. and Stoffel, M.: Lake outburst and debris flow disaster at Kedarnath, June 2013: hydrometeorological triggering and topographic predisposition, Landslides, 10.1007/s10346-015-0584-3, 2015.

Azzoni, R.S., Fugazza, D., Zennaro, M., Zucali, M., D'Agata, C., Maragno, D., Cernuschi, M., Smiraglia, C., Diolaiuti, G.A. (2017). Recent structural evolution of Forni Glacier tongue (Ortles-Cevedale Group, Central Italian Alps). *J. Maps*, 13(2): 870-878, doi: 10.1080/17445647.2017.1394227.

Baumann, P., 2019. Aerial Photography: History and Georeferencing. *The Geographic Information Science & Technology Body of Knowledge* (2nd Quarter Edition), John P. Wilson (Ed.).

Carrivick, J. L. and Tweed, F. S.: A global assessment of the societal impacts of glacier outburst fl oods, Glob. Planet. Change, 144, 1–16, doi: 10.1016/j.gloplacha.2016.07.001, 2016.

Chiarle, M., Iannotti, S., Mortara, G. and Deline, P.: Recent debris flow occurrences associated with glaciers in the Alps, Glob. Planet. Change, 56, 123–136, 2007.

Costa, J. E.: Physical geomorphology of debris flows, in Developments an Applications of Geomorphology, edited by J. E. Costa and P. J. Fleisher, pp. 268–317, Springer-Verlag, Berlin., 1984.

Cox, S. C., McSaveney, M. J., Spencer, J., Allen, S. K., Ashraf, S., Hancox, G. T., Sirguey, P., Salichon, J. and Ferris, B. G.: Rock avalanche on 14 July 2014 from Hillary Ridge, Aoraki/Mount Cook, New Zealand, Landslides, 12(2), 395–402, doi:10.1007/ s10346-015-0556-7, 2015.

De Michele, C.; Avanzi, F.; Passoni, D.; Barzaghi, R.; Pinto, L.; Dosso, P.; Ghezzi, A.; Gianatti, R.; Della Vedova, G. Using a Fixed-Wing UAS to Map Snow Depth Distribution: An Evaluation at Peak Accumulation. *Cryosphere* **2016**, *10*, 511–522.

Deline, P., 2002. Etude géomorphologique des interations écroulements rocheux/glaciers dans la haute montagne alpine (versantsud-est du massif du Mont Blanc). Thèse de doctorat de géographie, Université de Savoie. Pp. 539.

Diolaiuti, G.A., Smiraglia, C., 2010. Changing glaciers in a changing climate: how vanishing geomorphosites have been driving deep changes in mountain landscapes and environments. *Géomorphologie: relief, processus, environnement*, 2: 131-152.

Eltner, A., Kaiser, A., Castillo, C., Rock, G., Neugirg, F., Abellán, A., 2015. Image-based surface reconstruction in geomorphometry – merits, limits and developments. *Earth Surface Dynamics*, 4: 359-389.

Evans, S. G. and Clague, J. J.: Catastrophic rock avalanches in glacial environment, Proc. 5th Int. Synposium Landslides, July 10-15, 1988, 2, 1153–1158, 1988.

Faillettaz, J., Funk, M. and Vincent, C.: Avalanching glacier instabilities: Review on processes and early warning perspectives, Rev. Geophys., 53(2), 203–224, doi:10.1002/2014RG000466, 2015.

Fey, C., Wichmann, V., Zangerl, C., 2017.Reconstructing the evolution of a deap seated rockslide (Marzell) and its responseto glacial retreat based on historic and remote sensing data. *Geomorphology*, 298: 72-85.

Ford, M., 2013. Shoreline changes interpreted from multitemporal aerial photographs and high-resolution satellite images: Wotje atoll, marshall islands. *Remote Sensing of Environment* 135, pp. 130–140.

Fox, A. J. and Cziferszky, A., 2008. Unlocking the time capsule of historic aerial photography to measure changes in antarctic peninsula glaciers. *The Photogrammetric Record* 23(121), pp. 51–68.

Fraser, C. S. (2013). Automatic camera calibration in close range photogrammetry. *Photogrammetric Engineering & Remote Sensing*, *79*(4), 381-388.

Fraser, R. H., Olthof, I., Maloley, M., Fernandes, R., Prevost, C., van der Sluijs, J., Kokelj, S., Lantz, T., & Tunnicliffe, J. (2015). UAV photogrammetry for mapping and monitoring of northern permafrost landscapes. *Int Arch Photogramm Remote Sens Spat Inf Sci XL-1 W*, *4*.

Fugazza, D., Scaioni, M., Corti, M., D'Agata, C., Azzoni, R.S., Cernuschi, M., Smiraglia, C., Diolaiuti, G.A., 2018. Combination of UAV and terrestrial photogrammetry to assess rapid glacier evolution and map glacier hazards. Nat. Hazards Earth Syst. Sci. 18, 1055–1071. //doi.org/10.5194/nhess-18- 1055-2018.

Fugazza, D., Senese, A., Azzoni, R.S., Smiraglia, C., Cernuschi, C., Severi, D., Diolaiuti, G.A., 2015. Highresolution mapping of glacier surface features. The UAV survey of the Forni Glacier (Stelvio National Park, Italy). *Geografia Fisica e Dinamica del Quaternario*, 38: 25-33.

Fujii, Y., Higuchi, K., 1977. Statistical analysis of the forms of the glaciers in Khumbu Himal. Journal Japan Society Snow Ice (Seppyo) 39, 7–14 (Special issue).

Fujita, K., Inoue, H., Izumi, T., Yamaguchi, S., Sadakane, A., Sunako, S., Nishimura, K., Immerzeel, W. W., Shea, J. M., Kayashta, R. B., Sawagaki, T., Breashears, D. F., Yagi, H. and Sakai, A.: Anomalous winter snow amplifed earthquake induced disaster of the 2015 Langtang avalanche in Nepal, Nat. Hazards Earth Syst. Sci. Discuss., 1–27, doi:10.5194/nhess-2016-317, 2016.

Furukawa, y., Ponce, J., 2010: Accurate, Dense, and Robust Multi-View Stereopsis. – IEEE Transactions on Pattern Analysis and Machine Intelligence **32** (8), pp.1362–1376.

Giordano, S., Le Bris, A. and Mallet, C., 2017. Fully automatic analysis of archival aerial images current status and challenges. In: *Joint Urban Remote Sensing Event (JURSE)*.

Haala et al, 2010] Haala, N.; Kada, M. An update on automatic 3D building reconstruction. In *ISPRS Journal of Photogrammetry and Remote Sensing*, vol. 65, pp. 570-580, 2010.

Haeberli, W.: Investigating glacier-permafrost relationships in high-mountain area: historical background, selected examples and research needs, in Cryospheric Systems: Glaciers and Permafrost, vol. 242, edited by C. Harris and J. B.Murton, pp. 29–37, Geological Society Special Publication, London., 2005.

Harris, C.: Climate Change, Mountain Permafrost Degradation and Geotechnical Hazard, in Global Change and Mountain Regions. An Overview of Current Knowledge, edited by U. M. Huber, H. K. M. Bugmann, and M. A. Reasoner, pp. 215–224, Springer, Dordrecht., 2005.

Harrison, W. D., Osipova, G. B., Nosenko, G. A., Espizua, L., Kääb, A., Fischer, L., Huggel, C., Burns, P. A. C., Truffer, M. and Lai, A. W.: Glacier Surges, in Snow and Ice-Related Hazards, Risks, and Disasters, edited by W. Haeberli and C. Whiteman, pp. 437–485, Elsevier., 2014.

Huggel C, Zgraggen-Oswals S, Haeberli W et al. (2005) The 2002 rock/ ice avalanche at Kolka/Karmadon, Russian Caucasus: Assessment of extraordinary avalanche formation and mobility, and application of QuickBird satellite imagery. *Natural Hazards and Earth System Sciences*
5: 173–187.

Huggel, C., Kääb, A., Haeberli, W., Teysseire, P. and Paul, F.: Remote sensing-based assessment of hazards from glacier lake outbursts: a case study in the Swiss Alps, Can. Geotech. J., 39, 316–330, 2002.

Huggel, C.: Recent extreme slope failures in glacial environments: effects of thermal perturbation, Quat. Sci. Rev., 28,1119–1130, 2009.

Ioannides, M., Hadjiprocopi, A., Doulamis, N., Doulamis, A., Protopapadakis, E., Makantasis, K., Santos, P., Fellner, D., Stork, A., Balet, O., Julien, M., Weinlinger, G., Johnson, P. S., Klein, M., and Fritsch, D.: ONLINE 4D RECONSTRUCTION USING MULTI-IMAGES AVAILABLE UNDER OPEN ACCESS, ISPRS Ann. Photogramm. Remote Sens. Spatial Inf. Sci., II-5/W1, 169–174, https://doi.org/10.5194/isprsannals-II-5-W1-169-2013, 2013.

James, M.R., Robson, S., Smith, M.W. (2017). 3-D uncertainty-based topographic change detection with structure-from-motion photogrammetry: precision maps for ground control and directly georeferenced surveys. *Earth Surf. Proc. Landforms*, 42(12): 1769-1788.

Kääb, A. Monitoring High-Mountain Terrain Deformation from Repeated Air-and Spaceborne Optical Data: Examples Using Digital Aerial Imagery and ASTER Data. *ISPRS J. Photogramm. Remote Sens.* **2002**, *57*, 39–52.

Kääb, A.; Huggel, C.; Barbero, S.; Chiarle, M.; Cordola, M.; Epifani, F.; Haeberli, W. Glacier Hazards At Belvedere Glacier and the Monte Rosa East Face, Italian Alps: Processes and Mitigation. *Inter. Natl. Symp.* 2004, 67–78.

Kaufmann, V.; Ladstädter, R. Quantitative Analysis of Rock Glacier Creep by Means of Digital Photogrammetry Using MultiTemporal Aerial Photographs: Two Case Studies in the Austrian Alps. In Proceedings of the 8th International Conference on Permafrost, Zurich, Switzerland, 21–25 July 2003; pp. 21–25.

Kraus, K., 1994. Fotogrammetria. Vol. 1—Teoria e applicazioni, Libreria Universitaria Levrotto and Bella, Torino, p. 516.

Krautblatter, M., Funk, D. and Guenzel, F. K.: Why permafrost rocks become unstable: a rock-ice mechanical model in time and space, Earth Surf. Process. Landforms, 38, 876–887, doi:10.1002/esp.3374, 2013.

Lague D., Brodu N., Leroux J., *Accurate 3D comparison of complex topography with terrestrial laser scanner: Application to the Rangitikei canyon (N-Z)*, ISPRS Journal of Photogrammetry and Remote Sensing, 2012.

Lesca, C., 1972. L'espansione della lingua terminale del Ghiacciaiodella Brenva in base ai rilievi fotogrammetrici del 1959, 1970 e 1971. Bollettino Comitato Glaciologico Italiano, Ser. 2 20, 93–101.

M. Pierrot-Deseilligny, N. Paparoditis . A multiresolution and optimization-based imagematching approach: An application to surf ace reconstruction from SPOT5-HRS stereoimagery. In IAPRS vol XXXVI-1/W41 in ISPRS Workshop On Topographic Mapping FromSpace (With Special Emphasis on Small Satellites), Ankara, Turquie, 02-2006.

Masetti M, Diolaiuti G, D'Agata C et al. (2010) Hydrological characterization of an ice-contact lake: Miage lake (Monte Bianco, Italy). *Water Resources Management* 24: doi 10.1007/s11269-009-9519-x.

Mayer, C. (2010). "The Early History of Remote Sensing of Glaciers". In: *Remote Sensing of Glaciers*. Ed. by P. Pellikka and W. G. Rees. Leiden, the Netherlands: CRC Press, pp. 67–80.

McSaveney, M. J.: Recent rockfalls and rock avalanches in Mount Cook National Park, New Zealand, Geol. Soc. Am. Rev. Eng. Geol., XV, 35–69, 2002.

Micheletti N., Chandler J.H., Lane S.N., (2015) Section 2.2. *Structure from Motion (SfM) photogrammetry.* In: Cook, SJ, Clarke, LE, Nield, JM (eds) Geomorphological Techniques (Online Edition). London, UK: British Society for Geomorphology. ISSN: 2047-0371.

Nocerino, E., Menna, F. and Remondino, F., 2012. Multitemporal analysis of landscapes and urban areas. *International Archives of the Photogrammetry, Remote Sensing and Spatial Information Sciences* 39(B4), pp. 85–90.

O'Connor JE and Costa JE (1993) Geologic and hydrologic hazards in glacierized basins in North America resulting from 19th and 20th century global warming. *Natural Hazards* 8: 121–140.

O'Connor, J. E., Hardison, J. H. and Costa, J. E.: Debris flows from failures of Neoglacial-Age moraine dams in the Three Sisters and Mount Jefferson wilderness areas, Oregon., US Geol. Surv. Prof. Pap. , 1606, 2001.

Østrem G (1959) Ice melting under a thin layer of moraine and the existence of ice in moraine ridges. *Geografiska Annaler* 41: 228–230.

Poli, D.; Casarotto, C.; Strudl, M.; Bollmann, E.; Moe, K.; Legat, K. Use of Historical Aerial Images for 3D Modelling of Glaciers in the Province of Trento. *ISPRS Int. Arch. Photogramm. Remote Sens. Spat. Inf. Sci.* 2020, *XLIII-B2*, 1151–1158.

Rebetez, M., LUGON, R. and BAERISWYL, P.-A.: CLIMATIC CHANGE AND DEBRIS FLOWS IN HIGH MOUNTAIN REGIONS: THE CASE STUDY OF THE RITIGRABEN TORRENT (SWISS ALPS), Clim. Change, 36(3/4), 371–389, doi:10.1023/A:1005356130392, 1997.

Rickenmann, D. and Zimmermann, M.: The 1987 debris flows in Switzerland: documentation and analysis, Geomorphology, 8, 175–189, 1993.

Ryan, J.C.; Hubbard, A.L.; Box, J.E.; Todd, J.; Christoffersen, P.; Carr, J.R.; Holt, T.O.; Snooke, N. UAV Photogrammetry and Structure from Motion to Assess Calving Dynamics at Store Glacier, a Large Outlet Draining the Greenland Ice Sheet. *Cryosphere* 2015, *9*, 1–11.

Scaioni, M., Barazzetti, L., Yordanov, V., Azzoni, R.S., Fugazza, D., Cernuschi, M., Diolaiuti, G.A., 2019. "Structure-From-Motion Photogrammetry to Support the Assessment of Collapse Risk in Alpine Glaciers." In: O. Altan, M. Chandra, F. Sunar, T. Tanzi T. (Ed.'s), Intelligent Systems for Crisis Management. Gi4DM 2018, Lecture Notes in Geoinformation and Cartography. Springer, Cham (Switzerland), pp. 239-263.

Scaioni, M., Corti, M., Diolaiuti, G., Fugazza, D., Cernuschi, M. (2017). Local and general monitoring of Forni glacier (Italian alps) using multi-platform structure-from-motion photogrammetry. *Int. Arch. Photogramm. Remote Sens. Spatial Inf. Sci.* Vol. 42, Part 2/W7:1547-1554, DOI:10.5194/isprs-archives-XLII-2-W7-1547-2017.

Scaioni, M., Crippa, J., Corti, M., Barazzetti, L., Fugazza, D., Azzoni, R., Cernuschi, M., Diolaiuti, G.A., 2018. Technical Aspects Related to the Application of SfM Photogrammetry in High Mountain. Int. Arch. Photogramm. Remote Sens. Spatial Inf. Sci., Vol. XLII, Part 2, 1029-1036.

Scaioni, M., Roncella, R. and Alba, M. I., 2013. Change detection and deformation analysis in point clouds: application to rock face monitoring. Photogrammetric Engineering & Remote Sensing 79(5): 441– 455.

Schneider, D., Huggel, C., Cochachin, A., Guillén, S. and García, J.: Mapping hazards from glacier lake outburst floods based on modelling of process cascades at Lake 513, Carhuaz, Peru, Adv. Geosci, 35, 145–155, doi:10.5194/adgeo-35-145-2014.

Schneider, J. F., Gruber, F. E. and Mergili, M.: Recent Cases and Geomorphic Evidence of Landslide Dammed Lakesand Related Hazards in the Mountains of Central Asia, in Landslide Science and Practice, pp. 57–64, Springer Berlin Heidelberg, Berlin, Heidelberg., 2013.

Smiraglia, C., Diolaiuti, G., and D'Agata, C., 2001: I ghiacciai delle Alpi italiane: variazioni areali e volumetriche e dinamica geomorfologia recente. Relazione contratto di ricerca n8 R1877 Milano: CESI.

Smiraglia, C., Diolaiuti, G., Casati, D., and Kirkbride, M., 2000: Recent areal and altimetric variations of Miage Glacier (Monte Bianco Massif, Italian Alps). In Nakawo, M., Raymond, C. F., and Fountain, A. (eds), Debris-Covered Glaciers IAHS Publ. 264: 227– 233.

Smith, M. W., Carrivick, J. L., & Quincey, D. J. (2015). Structure from motion photogrammetry in physical geography. Progress in Physical Geography, 40(2), 247–275. https://doi.org/10.1177/0309133315615805.

Snavely, N., Seitz, S.N., Szeliski, R., 2008. Modelling the world from internet image collections: *International Journal of Computer Vision*, Vol. 80, pp. 189-210.

Walstra, J., Dixon, N., Chandler, J.H., 2007. Historical aerial photographs for landslide assessment: two case histories. *Quart. J. Eng. Geol. Hydrogeol.*, 40. 315-332.

Westoby, M.J., Brasington, J., Glasser, N.F., Hambrey, M.J., Reynolds, J.M., 2012. 'Structure-from-Motion' photogrammetry: A low-cost, effective tool for geoscience applications. Geomorphology 179, 300–314. doi.org/10.1016/j.geomorph.2012.08.021.

Wu, c., 2007. SiftGPU: A GPU implementation of Scale Invariant Feature Transform (SIFT). http://cs.unc.edu/~ccwu/siftgpu (11 March 2019).

Zimmermann, M. and Haeberli, W.: Climatic change and debris flow activity in high mountain areas: a case study in the Swiss Alps, Catena Suppl., 22, 49–72, 1992.